DIFFRACTIVE HADRONIC PRODUCTION OF D MESONS

BY

WILLIAM WALLACE MACKAY

B. S., University of Virginia, 1974
M. S., University of Illinois, 1976

THESIS

Submitted in partial fulfillment of the requirements
for the degree of Doctor of Philosophy in Physics
in the Graduate College of the
University of Illinois at Urbana-Champaign, 1980

Urbana, Illinois

DISCLAIMER

DIFFRACTIVE HADRONIC PRODUCTION OF D MESONS

William Wallace MacKay, Ph. D.
Department of Physics
University of Illinois at Urbana-Champaign, 1980

This thesis reports on data taken in experiment E369 using the Chicago Cyclotron Spectrometer at Fermilab. A search for charmed D mesons was made using a beam of 217 GeV π^- incident on a liquid hydrogen target. The trigger required a recoil proton and a prompt muon. A total of 50±12 charged D events were seen in the $K^{\pm}\pi^{\mp}\pi^{\mp}$ channels and were split between the two channels in about equal amounts. Cuts were made which selected diffractive events, but when these cuts were removed the signal remained the same although the background was greatly increased. The Feynman x and angular distributions were consistent with diffractive production. A diffractive model yields a cross section of $(6\text{-}10)+4\ \mu b$.

ACKNOWLEDGMENTS

First and foremost, I would like to thank my advisor, Louis J. Koester Jr., for invaluable help throughout my graduate career. I would also like to thank all the E369 collaborators and the staffs of the institutions involved. Special thanks is due to G. O. Alverson, G. Ascoli, P. R. Avery, D. Bender, J. W. Cooper, S. R. Hahn, L. Holloway, L. M. Jones, T. B. W. Kirk, R. Klanner, U. E. Kruse, R. Raja, R. D. Sard, P. Schoessow, M. A. Shupe, E. B. Smith, and J. Wiss for help with analysis and discussions of the data. The help of Jerry Wray and the programing staff of the Illinois High Energy Physics Group made the analysis possible. I thank R. Gulbranson for useful advice on handling the Cyber and L. Seward for the construction of the recoil counters. The moral support provided by my parents and by my friends, Louis, George, Steve, Dee, John, Mike, and the Mad Dog to name a few, helped me carry out this job which seemed hopeless at times.

The work presented in this thesis was supported in part by the Department of Energy under grant EY-76-C-02-1195.

This thesis is dedicated to my dog Wolfgang.

TABLE OF CONTENTS

CHAPTER 1

Introduction

This thesis is the result of data gathered by an experiment ("E369") at Fermi National Accelerator Laboratory (FNAL) during the summer of 1977. The experiment was performed by physicists from several institutions: Fermilab, Harvard University, the University of Illinois, the University of Oxford, and Tufts University.

The primary thrust of the experiment was to find hadronically produced particles with charm and to measure the cross section. To do this we used a 217 GeV π^- beam and the Chicago Cyclotron Spectrometer. There were actually three separate triggers in the experiment:

1. the "2MU" trigger with both a Be target and a liquid H_2 target, requiring the detection of two oppositely charged muons,
2. the "1MUP" trigger using the H_2 target and requiring the detection of a muon and a recoiling proton, and
3. the low mass proton, "LMP", trigger using the H_2 target and a proton recoiling against a low mass system.

The 2MU trigger was basically for the investigation of hadronically produced charm anti-charm bound states, and was the subject of George Alverson's thesis (Alverson, 1979). The LMP trigger was designed to study diffractive production of three π states, but due to an error in the trigger setup this was not possible at a profitable level. This thesis only covers data from

the 1MUP trigger, so very little, if anything, shall be said about the other triggers. The 1MUP data amounted to about 200,000 triggers.

The type of reaction I studied was

$$\pi^- + p \longrightarrow p+D+D+X \longrightarrow p+D+\mu+X$$

where the D decays into a charged K and charged pions, the μ is assumed to come from the decay of the other D, and the X just signifies an inclusive reaction. The proton in the final state was required to recoil with a low momentum (0.3-0.7 GeV/c) and a large angle in the lab frame (60°-75°), so that the mass recoiling against the proton was large (3-6.5 GeV/c^2) and moving forward through the spectrometer. This mass cut removed events with recoiling masses considerably below the DD threshold (3.7 GeV/c^2).

I have specifically studied decays into final states with only charged hadrons. Dan Bender, in his thesis, will cover decays with neutral hadrons in the final state.

CHAPTER 2

Theory

Since the discovery of the J/ψ particle in 1974, there has been a flood of literature written about charmed hadrons (see for example Einhorn, 1975). I shall only briefly mention the high points of charmed particles. A few of the properties of the u, d, s, and c quarks are listed in Table 1 for the standard SU(4) quark model. In addition each quark comes in three colors and interacts strongly via the $SU(3)_c$ color force. This force is propagated by eight massless vector gluons which may carry color between quarks. The theory of these interactions is called quantum chromodynamics (QCD).

Charmed hadrons are basically like the old garden variety hadrons of the SU(3) theory, except that one or more of the valence quarks is now a charmed quark. Mesons are still built from a quark-antiquark pair, and baryons from three quarks. The resultant combination must still be formed in a color singlet state. Table 2 shows some of the expected mesons with bare charm. The charge conjugate states with $\bar{c}q$ combinations should also exist. Of these only the D and D^* mesons are experimentally well verified.

2.1 Decays of D Mesons

The Weinberg-Salam (Einhorn, 1975; Gaillard and Lee, 1975) model of weak interactions has incorporated the quark model to explain both charm and strangeness changing decays of hadrons. This theory introduces two left handed weak isospin doublets,

TABLE 1

Quark Properties

Flavor	I	I_3	Charge	Strangeness	Charm
u	1/2	1/2	2/3	0	0
d	1/2	-1/2	-1/3	0	0
s	0	0	-1/3	-1	0
c	0	0	2/3	0	1

TABLE 2

Mesons with Bare Charm

Meson	valence quarks	J^P	I	I_3	C	S
D^+	$c\bar{d}$	0^-	1/2	1/2	1	0
D^0	$c\bar{u}$	0^-	1/2	-1/2	1	0
F^+	$c\bar{s}$	0^-	0	0	1	1
D^{*+}	$c\bar{d}$	1^-	1/2	1/2	1	0
D^{*0}	$c\bar{u}$	1^-	1/2	-1/2	1	0
F^{*+}	$c\bar{s}$	1^-	0	0	1	1

$$\begin{pmatrix} c \\ u \end{pmatrix}_L \quad \text{and} \quad \begin{pmatrix} d' \\ s' \end{pmatrix}_L$$

where d' and s' are the orthogonal linear combinations of the d and s quarks,

$$d' = -\sin\theta_c\, d + \cos\theta_c\, s$$

and

$$s' = \cos\theta_c\, d + \sin\theta_c\, s.$$

The angle, θ_c, is called the Cabibbo angle and has been experimentally determined to be about 13° (Perkins, 1972). The hadronic charged current can be written as

$$J^H_\mu = (\bar{c}\ \bar{u})\, \gamma_\mu(1-\gamma^5) \begin{pmatrix} d' \\ s' \end{pmatrix}.$$

When this is coupled to the charged intermediate vector boson current, $W^\dagger_\mu J^\mu_H + J^{H\dagger}_\mu W^\mu$, we obtain the four different interaction vertices shown in Figure 1a with their relative coupling strengths. The decay of a heavy c quark into an s or a d quark is possible by the emission of a virtual W^+ boson. Figure 1b shows the vertices for the normal leptonic charged current. The virtual W boson from the decay of a c quark can produce either a lepton-antilepton pair or a $q\bar{q}$ pair. The decay of a c quark into a d quark must be suppressed by a factor of $\tan^2\theta_c = 0.05$ relative to its decay into an s quark. This means we should usually expect to see a strange particle from the decay of a charmed particle. In order to reconstruct a charmed particle, we must look at final states which have only hadrons since a neutrino is undetectable. Typical non-suppressed decays are

$$D^+ \longrightarrow K^- + \pi^+ + \pi^+,$$

and

$$D^0 \longrightarrow K^- + \pi^+.$$

Fig. 1a. The weak charged current quark vertices with relative coupling strengths.

Fig. 1b. The charged current leptonic vertices.

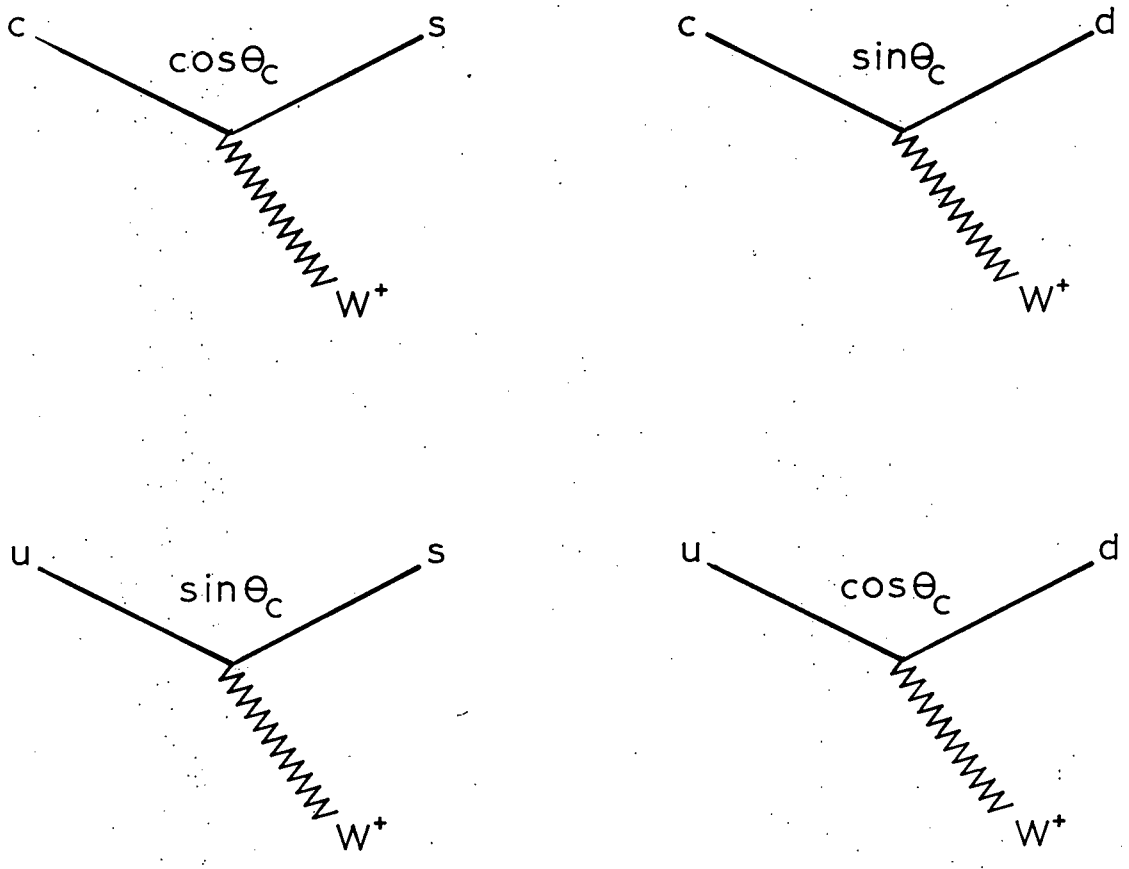

1a

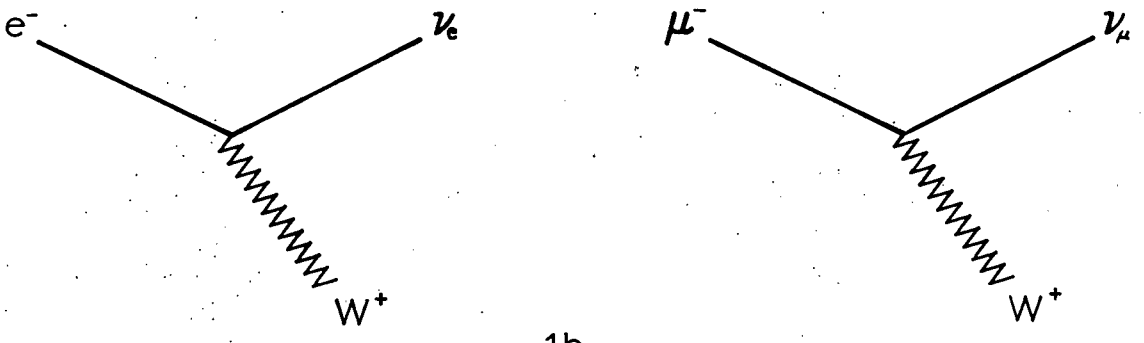

1b

Note that the decay $D^+ \rightarrow K^+ + \pi^- + \pi^+$ must be suppressed by $\tan^4\theta_c$ (see Figure 2).

Until recently it was believed that the semileptonic branching ratios of D^+ and D^o were equal. Recent data show that $B(D^+ \rightarrow \mu^+ X)/B(D^o \rightarrow \mu^+ X) \simeq 5\text{-}6$ (Kirkby, 1979). One explanation for this is the W-exchange interaction (Bander et al., 1980) between the c quark and $\bar{u}$ quark shown in Figure 3. No such diagram exists for D^+ decay. The partial widths for the semileptonic decays of D^+ and D^o should be equal. The diagram in Figure 3 increases the total width of the D^o's; thereby lowering the D^o semileptonic branching ratio. Another explanation uses a sextet dominance argument (Rosen, 1980) which basically invokes another SU(4) symmetry breaking.

2.2 Charm Production Mechanisms

Hadronic production models for charm are on much shakier ground than the decay models. One of the main reasons, if not the foremost, is the lack of data for direct production of charm. Most of what we know comes from experiments which attribute excess lepton signals to charm production or look at $c\bar{c}$ bound state production. The majority of the models can be categorized into two classes:

1. central production models, in which the $c\bar{c}$ system tends to be produced at rest in the center of mass, and
2. diffractive models, in which there is a small momentum transfer to the target, and the charmed particles tend to move forward with large momentum in the center of mass.

Fig. 2. The quark decay diagrams for the Cabibbo nonsuppressed decay, $D^+ \longrightarrow K^- \pi^+ \pi^+$, and the Cabibbo doubly suppressed decay, $D^+ \longrightarrow K^+ \pi^- \pi^+$.

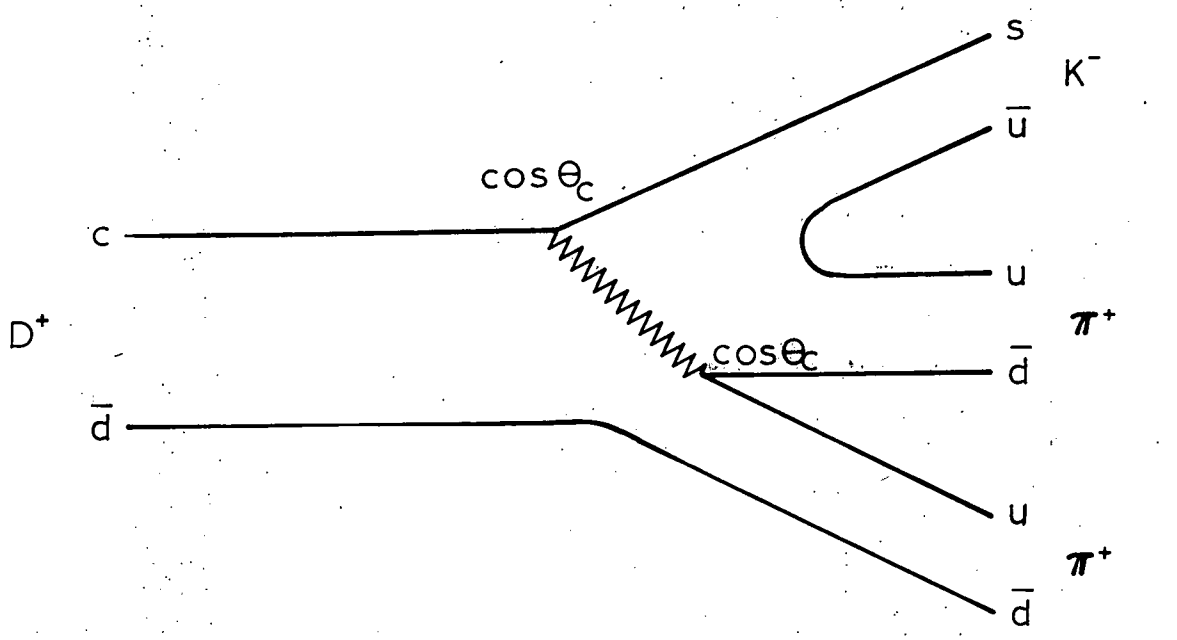
s
K⁻
ū
cos θc
c
u
D⁺
π⁺
cos θc
d̄
d̄
u
π⁺
d̄

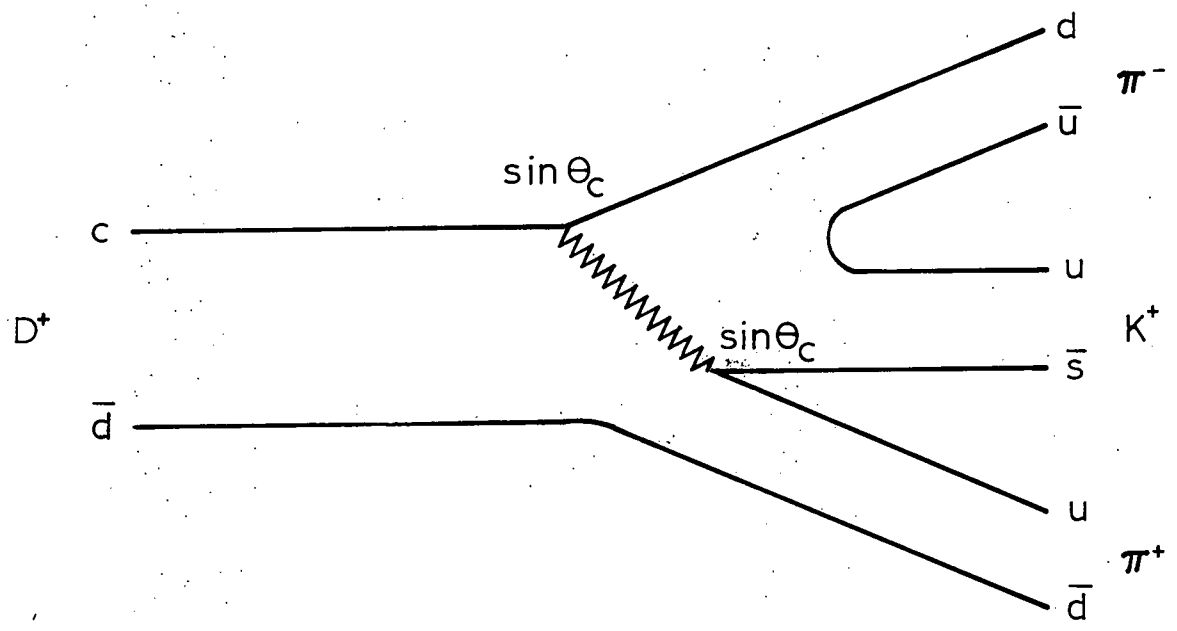
d
π⁻
ū
sin θc
c
u
D⁺
K⁺
sin θc
s̄
d̄
u
π⁺
d̄

Fig. 3. The W-exchange diagram for D^0 decay. Note that no such decay is possible for D^+ decay, since there is no quark with a charge of +4/3 for the $\bar{d}$ of the $D^+(c\bar{d})$ to connect with.

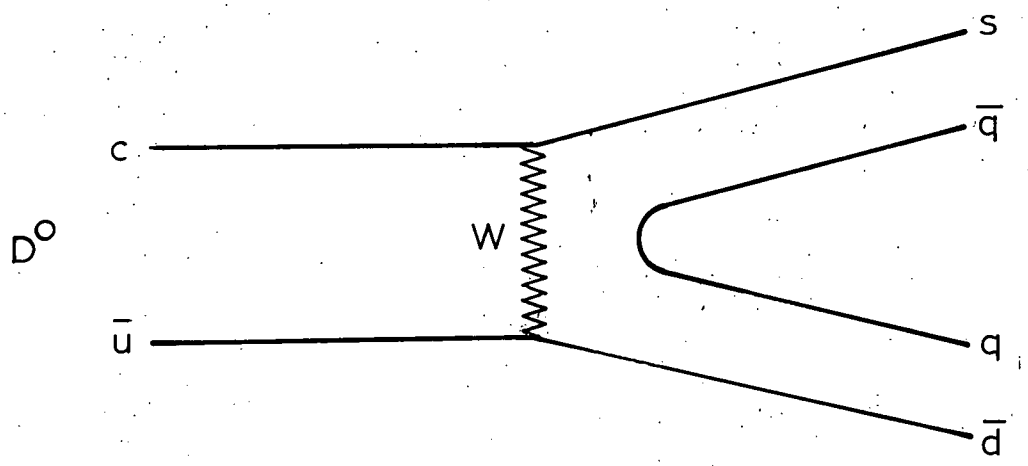
s
$\bar{q}$
c
D^0
W
$\bar{u}$
q
$\bar{d}$

2.2.1 Central Production

The two most popular central models are the Drell-Yan like model (Roy, 1975) and the gluon fusion model (Jones and Wyld, 1978; Carlson and Suaya, 1978). Both these models are statistical in nature and use the formalism of the parton model.

The parton model assumes that each hadron is composed of quarks, antiquarks, and gluons which are lumped together under the name of partons. Each particular type of parton is assumed to have a distribution in terms of the fraction of the hadron's momentum which is carried by the parton. For example, a proton is made up of all types of partons with a momentum fraction distribution $q_i(x_i)$ for the ith flavor of quarks, a momentum fraction distribution $q_j(x_j)$ for the jth flavor of antiquarks, and a momentum fraction distribution $g_k(x_k)$ for the kth color of gluons. At high energies it is assumed that all of these partons move in the same direction as the parent hadron and that we may neglect any transverse momentum of the individual partons. The momentum fraction of the ith parton is just

$$x_i = p_i / P,$$

where p_i is the momentum of the parton, and P is the momentum of the proton. Another assumption is that all the gluon distributions for a particular hadron are the same, since color is not an observable quantum number.

In considering a collision beteen two hadrons, h_1 and h_2, it is reasonable to look at a collision beteen a parton from h_1 and a parton from h_2. Perturbation theory can be used because the value

of the strong coupling constant, $g^2/4\pi = 0.25$ at these energies (Jones and Wyld, 1978).

The Drell-Yan like model (see Figure 4) considers the process where one parton is a quark and the other is an antiquark of the same flavor. This $q\bar{q}$ pair then annihilates into a virtual gluon which decays into a new $q\bar{q}$ pair.

The gluon fusion model (see Figure 5a) assumes that these partons are both gluons. Figure 5b shows the three lowest order vertices for the $gg \rightarrow q\bar{q}$ process. One embarrassing feature of the gluon fusion process is that the gluons carry color away from the initial hadrons, leaving a color imbalance. QCD predicts that there should be an infinite number of soft gluons near x=0. This color discrepancy may now be reconciled by assuming that these soft gluons can leak across with a unit probability.

The parton model writes the cross section for this sort of process as

$$\sigma = \int \sigma(M^2)\ \delta(M^2 - x_1 x_2 s)\ F_i^{h_1}(x_1)\ F_j^{h_2}(x_2)\ dx_1\ dx_2\ dM^2,$$

where $\sigma(M^2)$ is the QCD cross section for the parton-parton reaction, M is the mass of the $q\bar{q}$ system, and $F_i^{h_j}(x_j)$ is the momentum fraction distribution for a parton of type i found in hadron h_j, with a momentum fraction x_j. The delta function just requires energy conservation, and s is the square of the total center of mass energy of the incident hadrons.

For the gluon fusion model Jones and Wyld give the $gg \rightarrow c\bar{c}$ cross section as

$$\sigma(M^2) = \frac{4\pi}{3}\left(\frac{g^2}{4\pi}\right)^2 \left[-(28+31r)\beta + (r^2+16r+15)\ \ln\left(\frac{1+\beta}{1-\beta}\right)\right]/M^2,$$

Fig. 4. The Drell-Yan like mechanism. The unlabelled external lines signify an inclusive process.

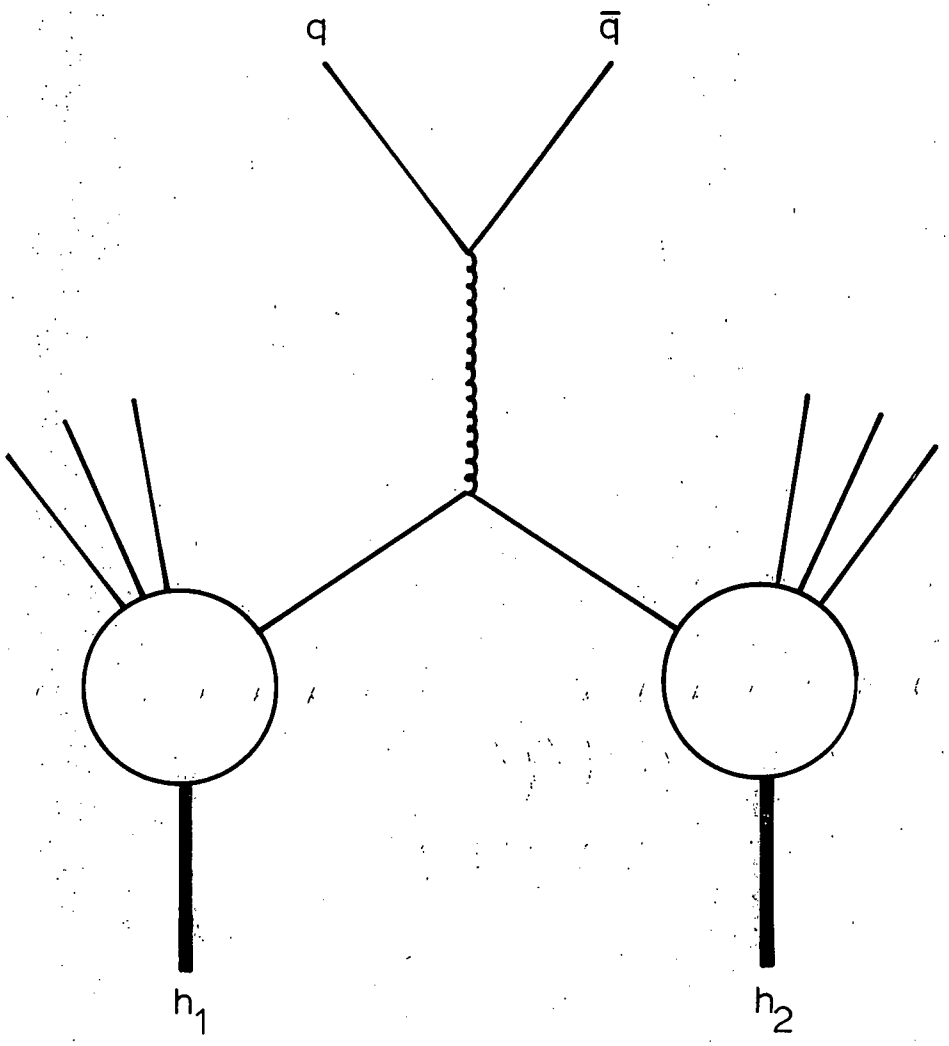
q
$\bar{q}$
h_1
h_2

Fig. 5a. The gluon fusion mechanism. The unlabelled external lines signify an inclusive process.

Fig. 5b. The three lowest order diagrams for the gluon fusion process.

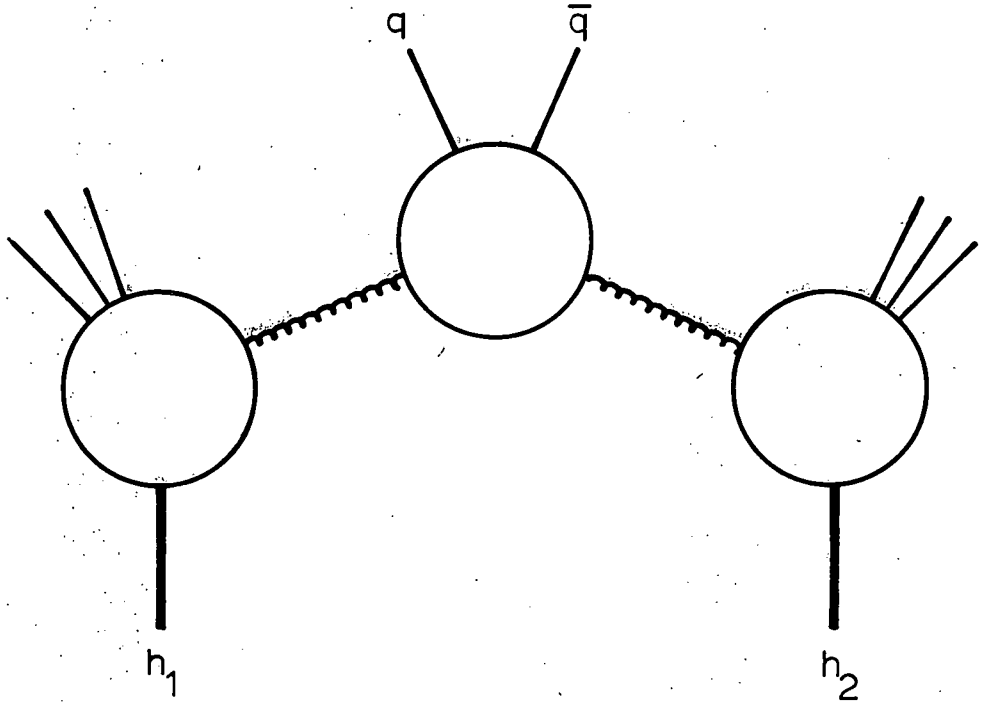

a

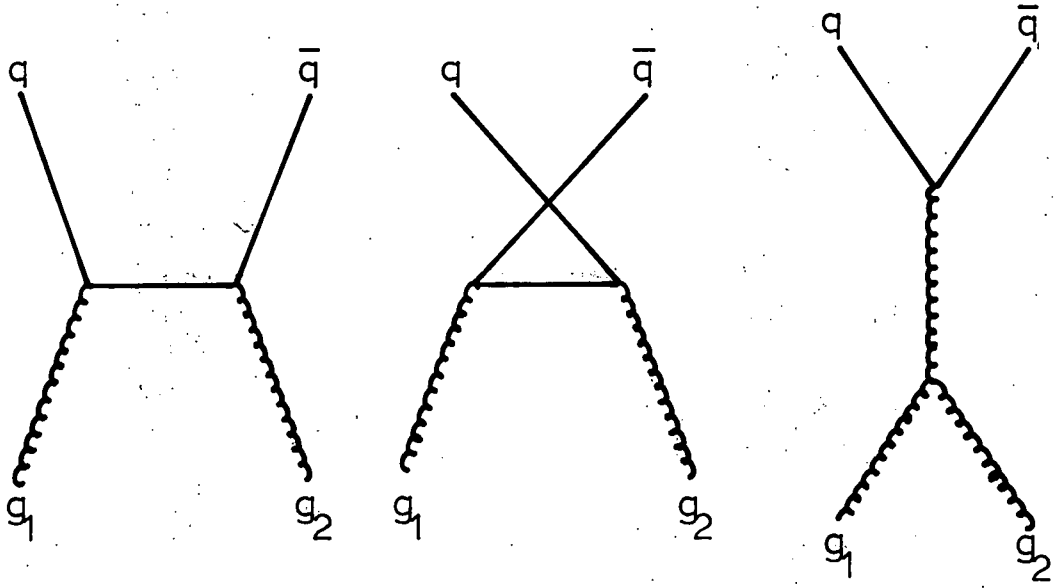

b

where for the c quark in the center of mass of the $c\bar{c}$ system, we have

$$\beta = 2P/M,$$

$$P = \sqrt{\left(\frac{M^2}{4} - m_c^2\right)}, \text{ and}$$

$$r = 1/\gamma^2 = (2m_c/M)^2.$$

They assume the charmed quark mass, m_c, is 1.65 GeV/c^2. They use a gluon structure function of the form

$$g(x) \propto \frac{1}{x}(1-x)^n,$$

with n=5 and n=10.

For our energy, with s=408 GeV^2, they calculate the total charm cross section from the Drell-Yan like process to be about 400 nb. Their calculations for the gluon fusion process give a cross section between 200 and 900 nb, depending on the value of n. In section 6.5, I take the gluon fusion model as a typical example of central production, and compare it to my data.

2.2.2 Diffractive Production

Cross sections have been calculated (Barger and Phillips, 1975) to be of the order of 1 nb for D channel exchange, and 60 nb for triple Regge processes with D exchange. These estimates are at least a factor of 100 smaller than our data indicates (6-10 μb). These small cross section calculations are the basis for the current belief that almost all of the charm cross section is due to central production.

So ignoring such sophisticated diffractive processes, I use a naive parameterization for the differential cross section,

$$\frac{d^2\sigma}{dt\,dM^2} \propto e^{-b|t|},$$

where t is the invariant momentum transfer to the proton, and M is the mass recoiling against the proton. The parameter, b, is a function of M^2 and has essentially no s dependence (Albrow, 1976). More is said about this model in section 6.4.

CHAPTER 3

Experimental Setup

3.1 Apparatus

The experiment was performed using the Chicago Cyclotron Magnet (CCM) spectrometer in the Muon Lab at Fermi National Accelerator Laboratory from July to August 1977. Most of the equipment has been described elsewhere (Alverson, 1979), so I will only give a brief summary of those parts. Figure 6 shows the placement of the various pieces. Before proceeding, the definition of a laboratory coordinate system is required. The direction of the beam, pointing north defined the Z-axis, and the Y-axis was vertically upward. The tradition of a right-handed system defined the X-axis, pointing to the west.

3.1.1 Beam

The beam was a 217 GeV/c momentum beam of negative pions from the N-1 line in the neutrino area (see Figure 7). A temporary modification in the beam line was made by the addition of a quadrupole magnet placed through the south wall of the Muon Lab in order to focus the beam in as small an area as possible in the target region.

Three sections of the beam pipe were fitted with Cerenkov mirrors and phototubes and were filled with helium at a pressure just below the kaon threshold. The composition of the beam was found to be about 97% π^-, 2% K^-, and 0.3% $\bar{p}$.

3.1.2 Target

The two targets used in the experiment consisted of a 2.6 cm

Fig. 6. The E369 Apparatus.

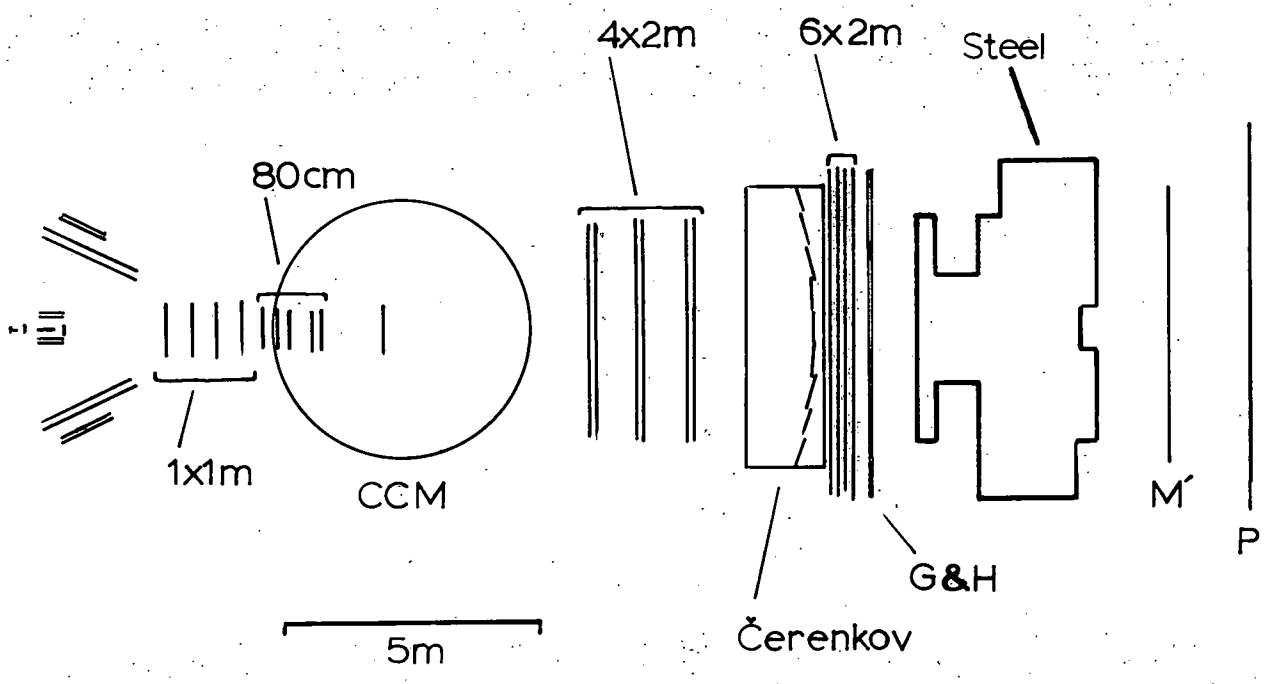
4x2m
6x2m
Steel
80cm
1x1m
CCM
M´
P
G&H
Čerenkov
5m

Fig. 7. The N-1 Beam line from the pion production target to the B1 counter shown in figure 8. The lines marked x and y were MWPC planes in those projections. The unmarked rectangles were hodoscope planes used to define a clean single particle beam. C102, C103, and C104 were the beam Cerenkov counters. 1W2 and 1E4 were the bending magnets for momentum selection.

Production
Target
Steering
Magnets
C102
1W2
C103
C104
1E4
xy
1QMU
xy
B1

beryllium target and a 46.1 cm long liquid hydrogen target. Each of these was followed by two thin scintillation counters with pulse height discrimination to permit triggering on interactions in one target or the other.

Since one of the objects of the experiment was to measure slow recoil protons coming out of the target at large angles with respect to the beam, we wanted the material between the interaction and the detecting counters to be as small as possible. A cylindrical flask, filled with liquid hydrogen and constructed of 5 mil mylar, was made 46.1 cm long and 1.59 cm in radius. This flask was covered with ten layers of 0.25 mil aluminized mylar for thermal insulation. A cylindrical sheath, made from Klegcell foam with a wall 3/8 inch thick and an outer diameter of 3 inches, surrounded the flask. The sheath was covered with a seal of 2 mil mylar and a vacuum was maintained between the seal and the flask. All this amounted to an equivalent of 0.15 g/cm^2 of liquid hydrogen for a proton coming from the center of the target. The effective length of the hydrogen target was only 40 cm, since the first 6 cm were enclosed in a large aluminum box for mechanical reasons.

There were five scintillation counters in the beam placed around the two targets (see Figure 8). Each had an RCA 8575 photo multiplier tube with a special emitter follower transistorized base (Kerns, 1977) for high rates. The first, and most important (B1), was a 1 inch diameter, 1/16 inch thick scintillator with an air light pipe. It provided the timing signal for the start of an event, and defined the beam upstream of both targets. The next

Fig. 8. West recoil arm and target region. The east arm was the mirror image of the west arm. B1-B5 were the target counters placed around the Be and H_2 targets. WF corresponds to the front layer of recoil counters which were numbered as shown. The back layer, WB, was ignored in the analysis.

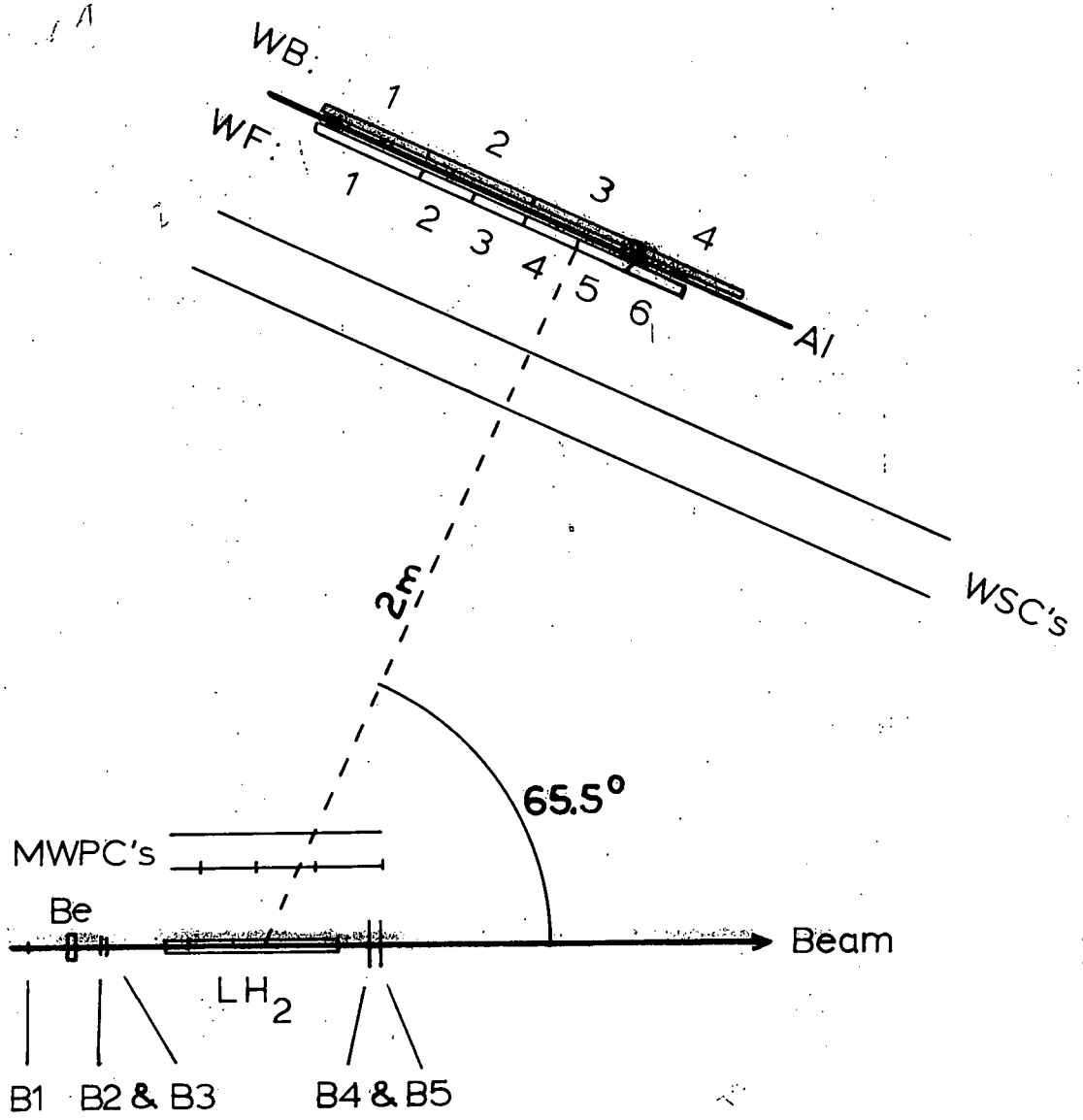
WB:
1
2
3
4
WF:
1
2
3
4
5
6
Al
WSC's
2m
65.5°
MWPC's
Be
Beam
LH2
B1
B2 & B3
B4 & B5

two (B2 and B3) were two inch squares of scintillator placed between the two targets. The last two, (B4 and B5) five inch squares, were placed downstream of the hydrogen target.

On either side of the target, in planes parallel to the beam, were two multi-wire proportional chambers (MWPC) with 176 vertical wires and 1/8 inch spacing. Each of the inner chambers had three fast sum line outputs covering 15 cm sections for use in the fast trigger logic.

Three helium filled bags were placed around the target region to reduce multiple scattering. One was downstream of B5 and upstream of the first 1x1 m^2 chamber, and the other two were between the recoil MWPC's and the recoil WSC's on the east and west arms.

3.1.3 Recoil Proton Arms

In addition to the above mentioned MWPC's, each recoil arm had two 2x2 m^2 wire spark chambers (WSC) with magnetostrictive readouts. Finally came two layers of scintillator separated by a half inch of aluminum for energy detection of the recoil particle.

The front layer of scintillator consisted of five six inch wide counters and one twelve inch wide counter. The back layer was four one-foot wide counters. Each of the ten counters was six feet tall and one inch thick with lucite light pipes. Each front counter had an RCA 8575 phototube on either end, and each back counter had a single Amperex 56DVP phototube on the top end. The front one foot wide counter was only used in the low mass trigger. The positioning of the counters relative to the target is shown in Figure 8.

3.1.4 The Apparatus Downstream of the Target

The CCM was a gigantic cylindrical dipole magnet with a 1.2 m gap between pole faces and an effective radius of 2.5 m. It was run at a field of 14.047 kG pointing down in the -y direction. This field gave a perpendicular momentum kick of about 2.1 GeV/c to charged particles. The over all angular acceptance of the spectrometer in the lab system was more than 70 mrad in both the x and y projections.

Downstream of the target and just upstream of the CCM were four 1x1 m^2 MWPC's, each with an x and a y plane. Then came five 80 cm square MWPC's leading into the CCM, with another 1x1 m^2 chamber in the center of the magnet. Downstream of the CCM were twelve planes of 2x4 m^2 capacitive readout WSC's. Farther downstream were eight planes of 2x6 m^2 WSC's with magnetostrictive readouts.

Between the two sets of WSC's was an 18 cell Cerenkov counter with nine cells above the beam and the other nine below the beam. The counter was filled with nitrogen at one atmosphere and had a 1.2 m path length to the mirrors. Figure 9 shows the light output for muons, pions, kaons, and protons as a function of momentum, with the curves normalized to the light expected from a speed of light particle.

Downstream of the 2x6 m^2 chambers were two layers of hodoscopes, labelled G and H, which were used for separating in-time tracks from out-of-time tracks. Behind the G and H hodoscopes were 2.2 meters of steel for stopping hadrons. After this absorber came two more hodoscopes, labelled M', and P (see

Fig. 9. Calculated light output from the Cerenkov as a function of particle momentum. 100% corresponds to a β=1 particle.

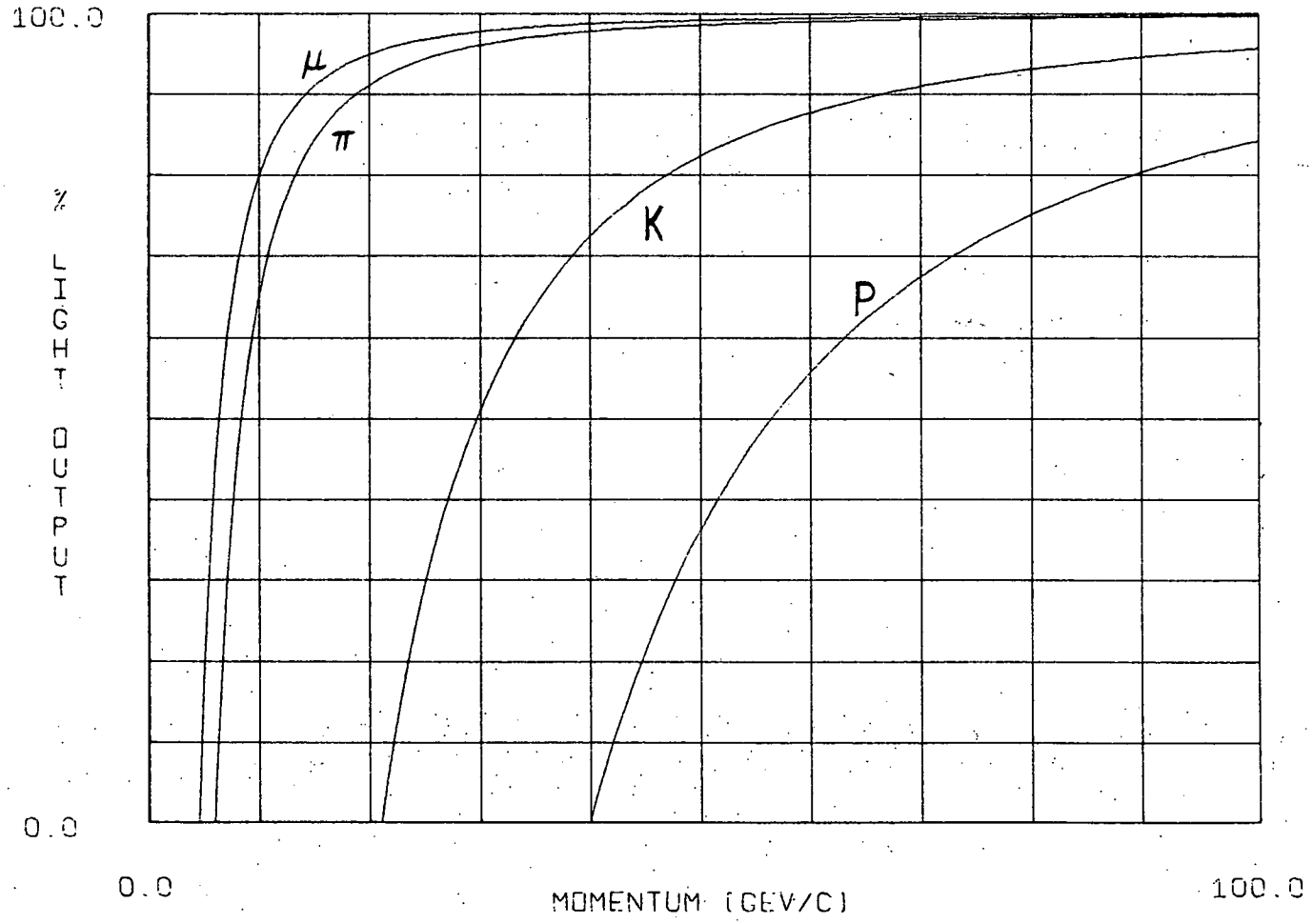
100.0
0.0
% LIGHT OUTPUT
μ
π
K
P
0.0
MOMENTUM (GEV/C)
100.0

Figure 10), which were used to detect muons.

There was also an array of 80 lead glass blocks just downstream of the G and H hodoscopes, but this was not used in this analysis.

3.2 Trigger Logic

3.2.1 High Mass Proton Requirement

The top and bottom phototube signals from each front layer recoil counter were put into a special adder integrater circuit (see Figure 11) to sum their pulse heights during a 20 ns interval. The two pulses were also discriminated and fed into a chronotron to give a timing signal independent of the position at which the counter was hit. The adder integrater signal was discriminated with a threshold twice that for a minimum ionizing pulse, and then put into coincidence with the chronotron signal to produce a timed signal. The amplitude and time information from each tube were also fed into ADC's and TDC's respectively, for off-line analysis.

An angular requirement (60^{o}-75^{o}) for the recoil proton was made by combining the appropriate counters with each sum line section of the recoil MWPC as shown in Figure 12 for the west recoil arm. This resulted in a mass cut between 3 and 6.5 GeV/c^2 for the system recoiling against the proton. The logic for the east arm was identical, and the two resulting signals were or-ed to produce the high mass trigger requirement.

3.2.2 "1MUP" Trigger

All timing was done with respect to the start signal from counter B1. Each of the other four target counter signals was put

Fig. 10. The P hodoscope. The four sets of counters, Q1 Q2, Q3, and Q4, were used in the trigger. The dashed line defines the area covered by the M' hodoscope trigger requirement. The muon trigger requirement was just the or of the signals from the 5 sets.

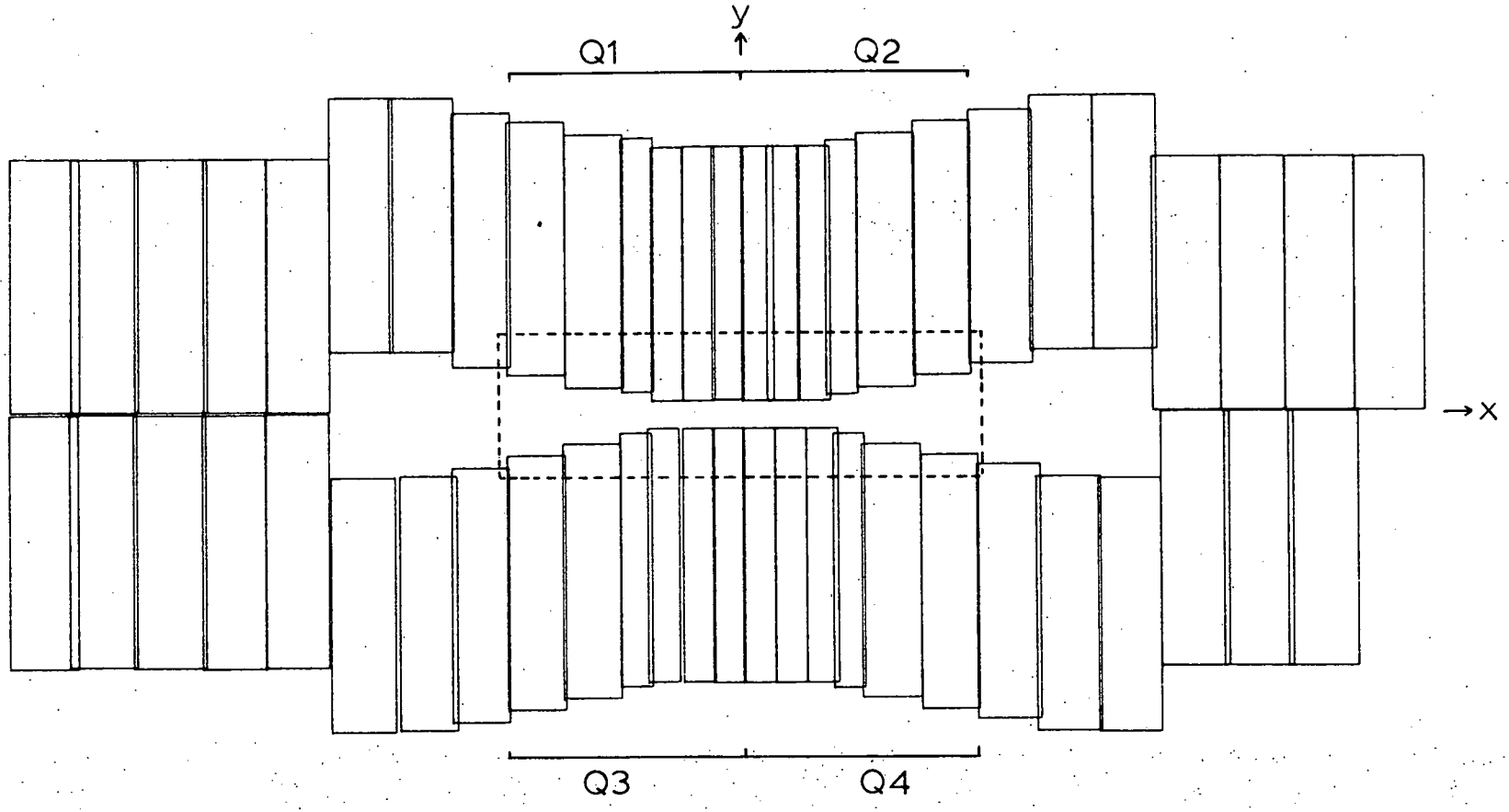
y
Q1
Q2
→X
Q3
Q4
P-HODOSCOPE
1 METER

Fig. 11. Trigger logic for a typical recoil counter (e.g. WF2).

F: linear fanout.

D: discriminator.

The outputs from the ADC's, TDC's, and latch were written to tape for off-line analysis.

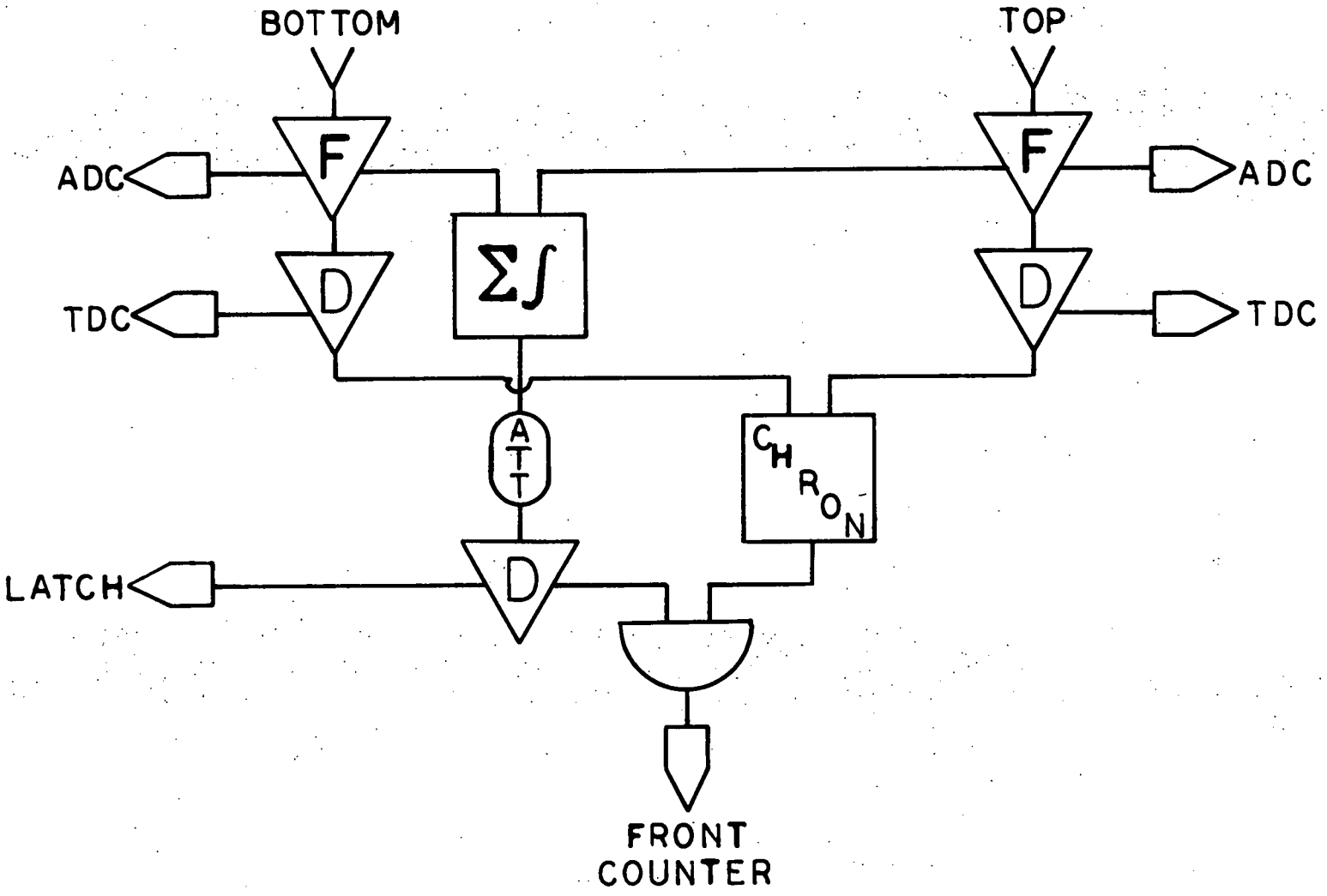
BOTTOM
TOP
F
F
ADC
ADC
D
D
TDC
TDC
ΣJ
ATT
CHRON
D
LATCH
FRONT
COUNTER

Fig. 12. Logic for the recoil proton trigger, west side. The logic for the east side was identical.

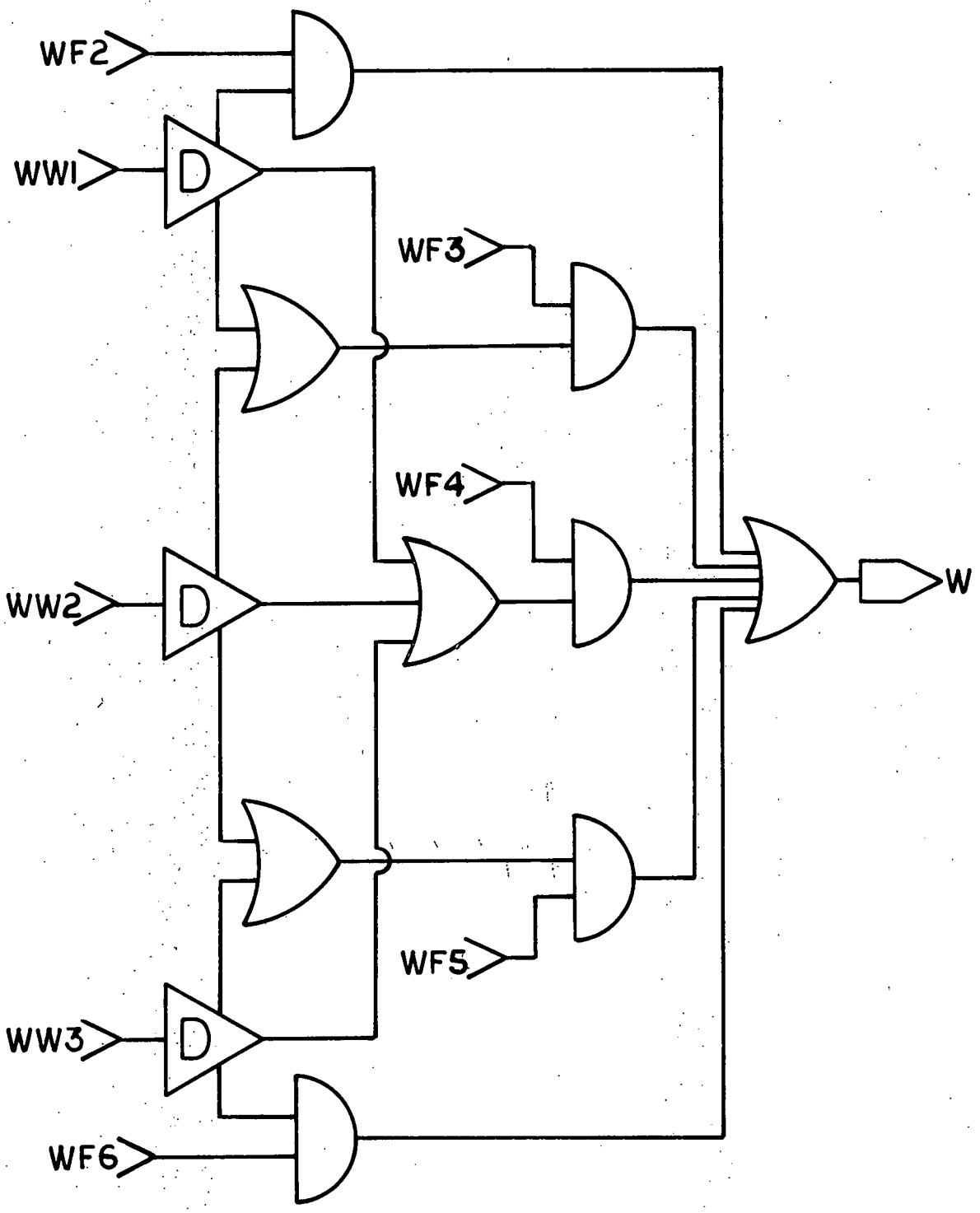
WF2
WW1
D
WF3
WF4
WW2
D
W
WF5
WW3
D
WF6

through high and low level discriminators (see Figure 13). The high level outputs from B2 and B3 were put in coincidence (B23H), as were the low level outputs (B23L), in order to distinguish whether or not an interaction took place upstream in the beryllium target. Similarly the outputs from B4 and B5 were combined to make the same test for an interaction upstream in either target. A hydrogen target interaction was defined by coincidence of B45H with the complement of B23H. One of the side effects of this requirement was to discriminate against events with three or fewer charged tracks besides the recoil proton.

The beam at Fermilab is such that there is a bunch of particles, called a bucket, about every 20 ns. Since some of the timing required gates longer than this, a beam self-veto circuit was designed to avoid recording ambiguous events with multiple beam tracks. This was done (see Figure 14) by putting B45L into an updating discriminator with a width of 32 ns and a 2 ns clip line on one output. The clipped output was then delayed by 32 ns and put in coincidence with the complement of another output to give a signal, unless another input pulse occurred before or after within 32 ns.

A clean hydrogen interaction was defined by a four-fold coincidence of the B1 start signal, B45H, the self-veto, and the complement of B23H. This interaction signal was then put in coincidence with the muon requirement (see Figure 10), the high mass proton trigger, and a requirement to remove halo muons from the beam (B98) (Hicks, 1978) to give the "1MUP" trigger (see Figure 15).

Fig. 13. Beam logic around targets.

F: linear fanout

L: low level discriminator

H: High level discriminator

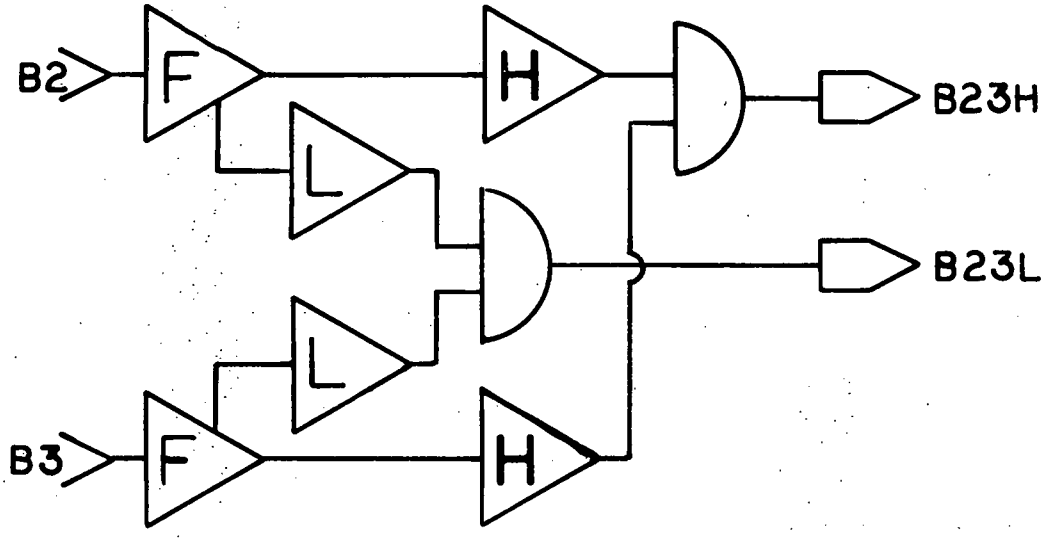
B2
F
H
L
B23H
B23L
L
B3
F
H

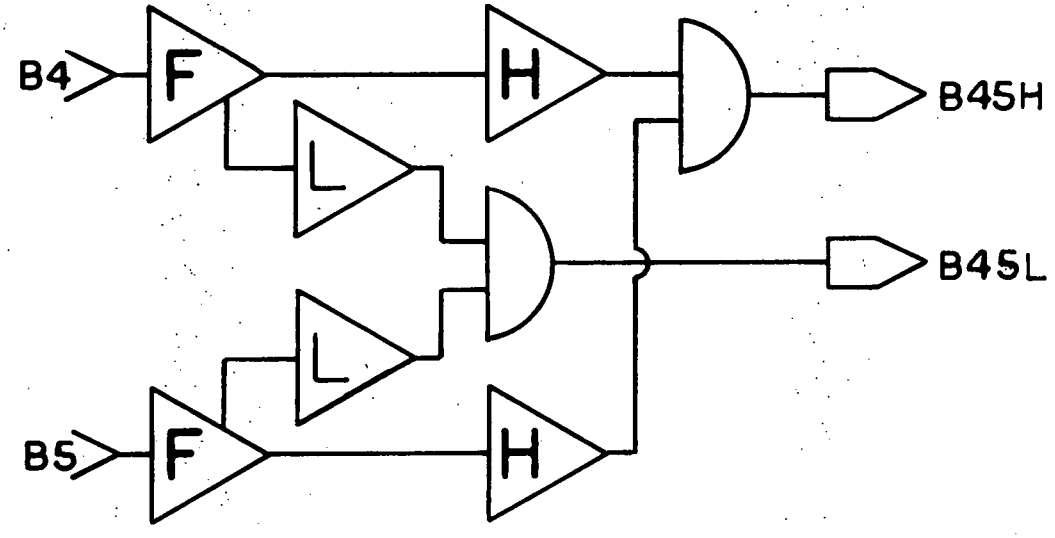
B4
F
H
L
B45H
B45L
L
B5
F
H

Fig. 14. Self veto logic. The discriminator was an updating discriminator with a 32 ns width and a 2 ns clip line on output C. Typical signals are shown for the labelled points for one input pulse and two input pulses within 32 ns of each other.

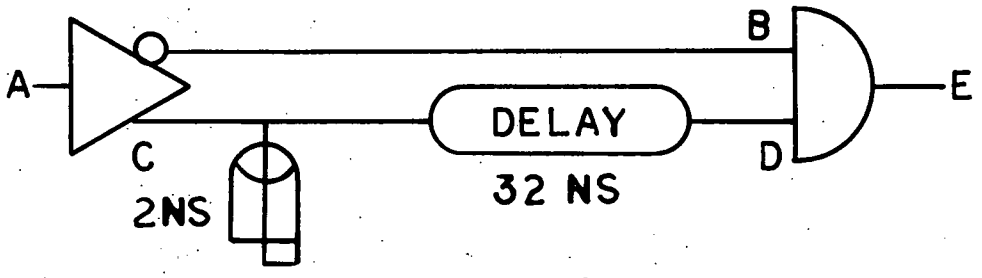

ONE PULSE

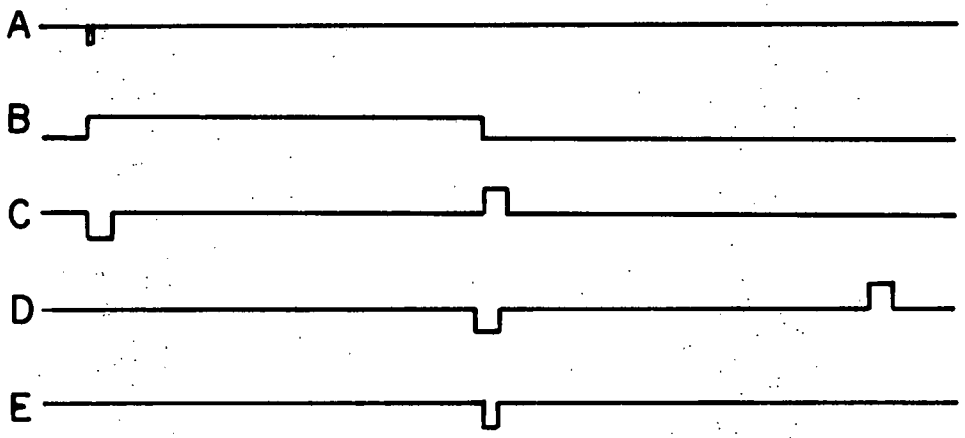

TWO PULSES

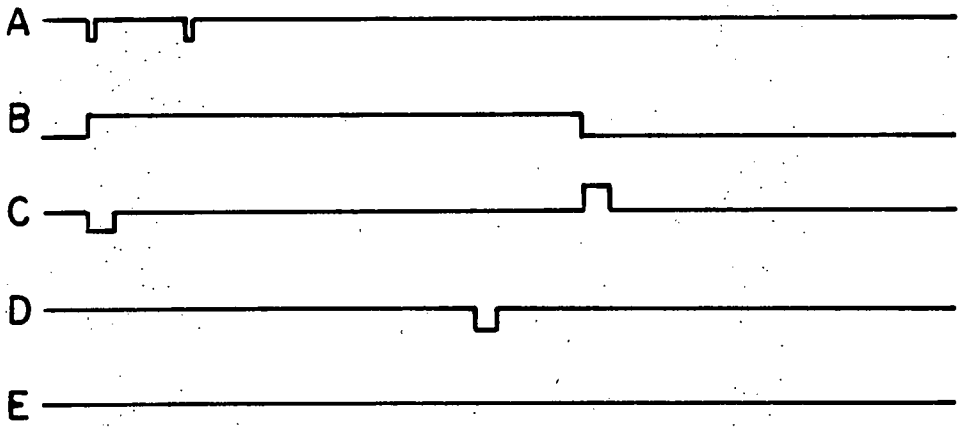

Fig. 15. Final "1MUP" trigger logic.

P is the or of the east and west proton signals.

Q1-Q4 and M' are the signals from the P and M' hodoscopes shown in figure 10.

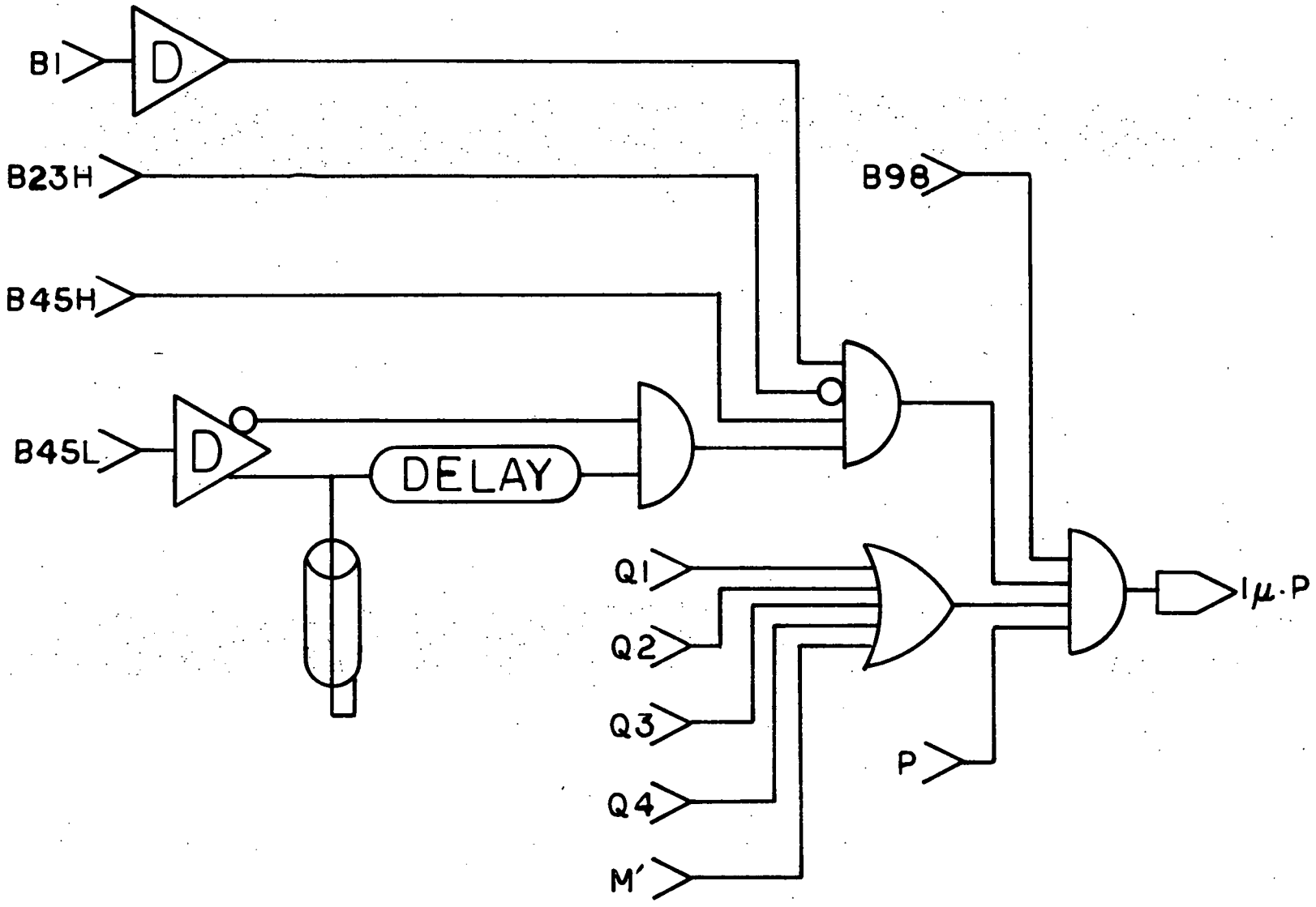
B1
D
B23H
B45H
B45L
D
DELAY
B98
Q1
Q2
Q3
Q4
M'
P
1μ·P

In addition there was some extra logic to stop the scalers and data acquisition if the on-line computer was busy. The on line computer was a Xerox Sigma-3 and was programmed by G. Alverson and L. Holloway. The data for each event were read in from a system of CAMAC crates and written to 9-track tapes at 800 bits per inch.

CHAPTER 4

Recoil Proton Detection and Calibration

The reason for using a recoil proton trigger was to pick out events with small momentum transfer and a large missing mass (about 3 to 6.5 Gev/c^2) that would be thrown forward through the spectrometer. The purpose of this chapter is to convince the reader that the recoil particles were really protons.

Professor R. D. Sard made a study of Fermilab hydrogen bubble chamber data from experiment E154 with a 147GeV π^- beam. For particles with momentum less than 1.4GeV/c, protons could be distinguished from pions by the amount of ionization the track made in the chamber. Requiring lab angles greater than 55°, and velocities corresponding to flight times between 11 and 30 ns, he found 90% of the recoil particles were protons. The largest amount of contamination occured for the fast particles, as shown in Figure 16.

By correlating the energy lost by the particle in traversing the scintillator with the velocity it had before losing any energy, we can decide whether the recoil particle was a proton or a pion. Energy loss per unit length, dE/dx, is a function of the charge and the velocity of a particle but not its mass. A frequently used parameterization (Rossi, 1952) is

$$\frac{dE}{dx} = -0.153(\text{MeVcm}^2/\text{g}) \left\{ \frac{r}{r-1} [9.96 + \ln(r-1)] - 1 \right\},$$

where x is in grams per square centimeter, and r is the square of the ratio of energy to momentum for the particle in question.

Fig. 16. The fraction of all recoil tracks with lab angles above 55^{o} and which were identified as protons as a function of time of flight over a distance of 2 m. This comes from Sard's study of bubble chamber data as described in the text.

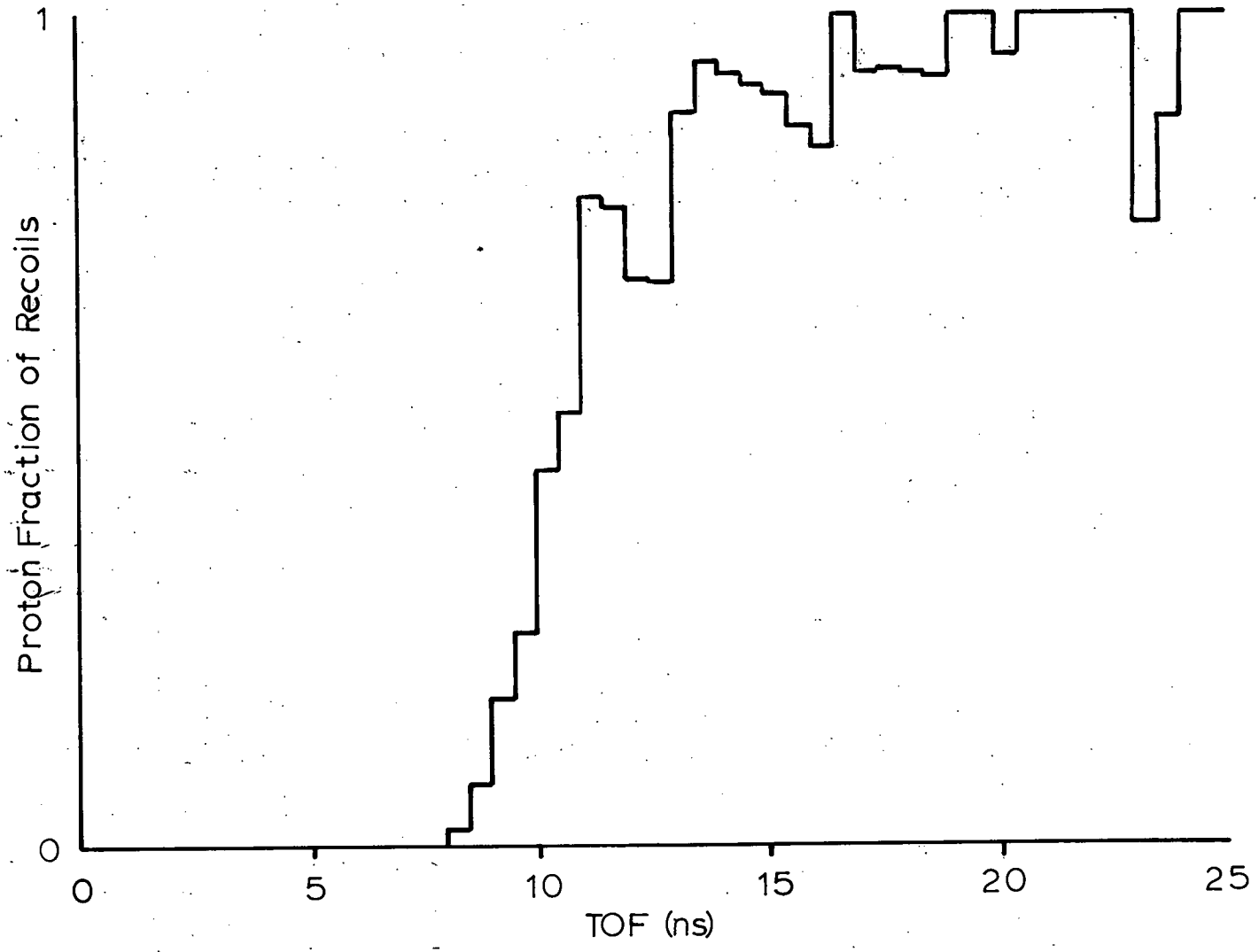
1
0
Proton Fraction of Recoils
0
5
10
15
20
25
TOF (ns)

Kinetic energy as a function of $\gamma(=E/M)$ for a particle of mass M may be written as

$$K = (\gamma-1)M.$$

Taking the derivative we get

$$dK/d\gamma = M,$$

or

$$\delta\gamma = \delta K/M.$$

For a proton and a pion both starting with the same velocity, an infinitesimal distance dx would correspond to the same kinetic energy loss for both particles, but the change in γ would be greater for the pion. This means that the pion will stop in less material than the proton.

For a one inch thick scintillator, particles of increasing velocity will deposit all their energy until one reaches a critical speed at which it just penetrates the back edge. For a proton this is about 31% of the speed of light. As the velocity increases, the total energy lost by a particle in the scintillator decreases, since the integration takes place farther to the right on the dE/dx curve (see Figure 17). Calculated energy loss versus velocity is shown in Figure 18 for both protons and pions.

Time of flight measurements were made so that the proton's velocity could be calculated. As previously mentioned, each counter in the front layer had a phototube on either end, provided with both time and pulse height analysis. The time actually measured for the top tube was

$$T_t = Tof + (Z_v - Z_{BI})/c + T_{BI} + y/V_s + D_t$$

where Tof is the actual time of flight from the interaction

Fig. 17. Energy loss (MeV cm^2/g) in scintillator for a singly charged particle as a function of $\gamma=E/m$.

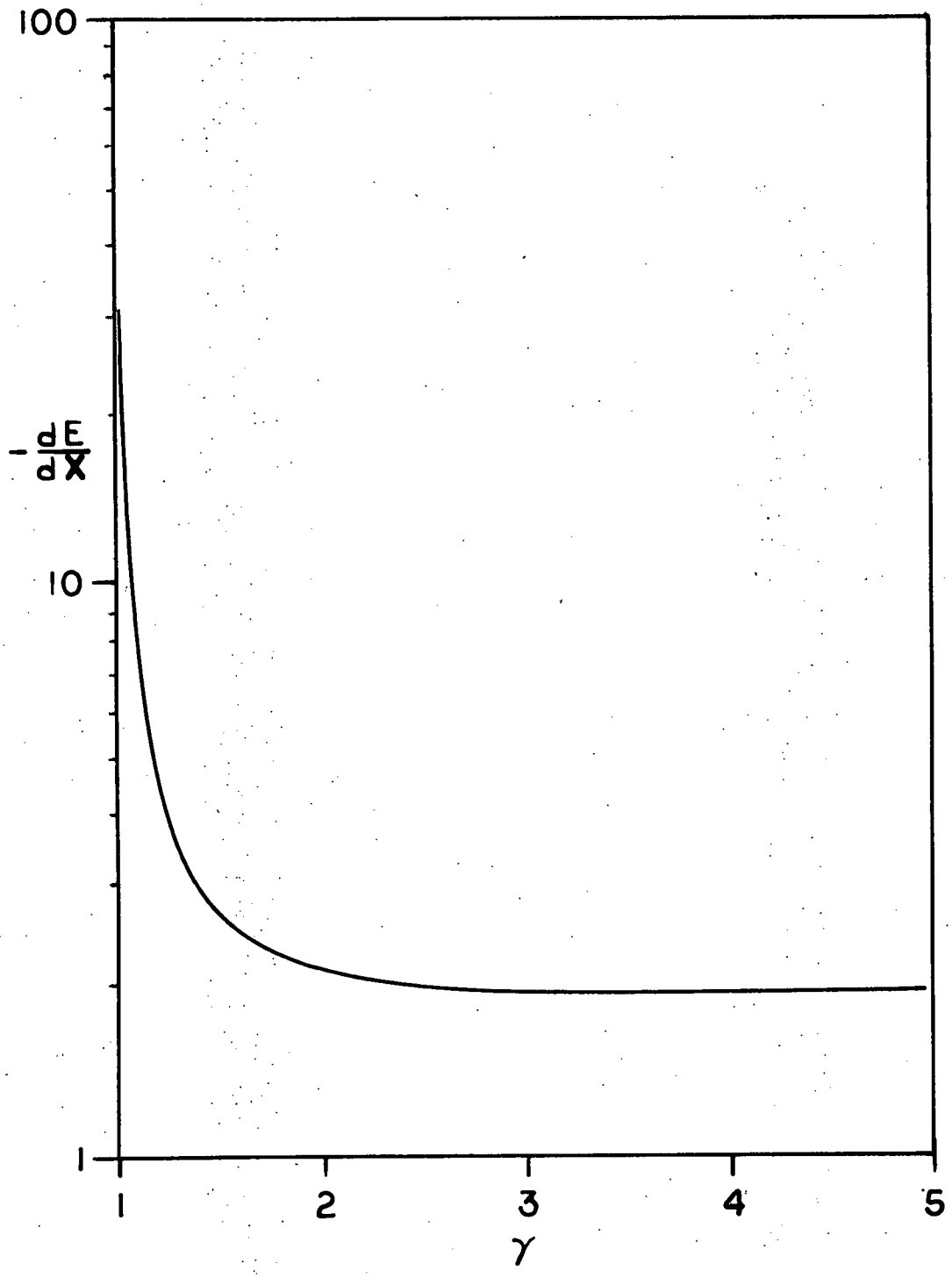
100
10
1
$-\frac{dE}{dX}$
1
2
3
4
5
γ

Fig. 18. Calculated energy loss in the front layer of recoil counters by protons and pions as a function of particle velocity.

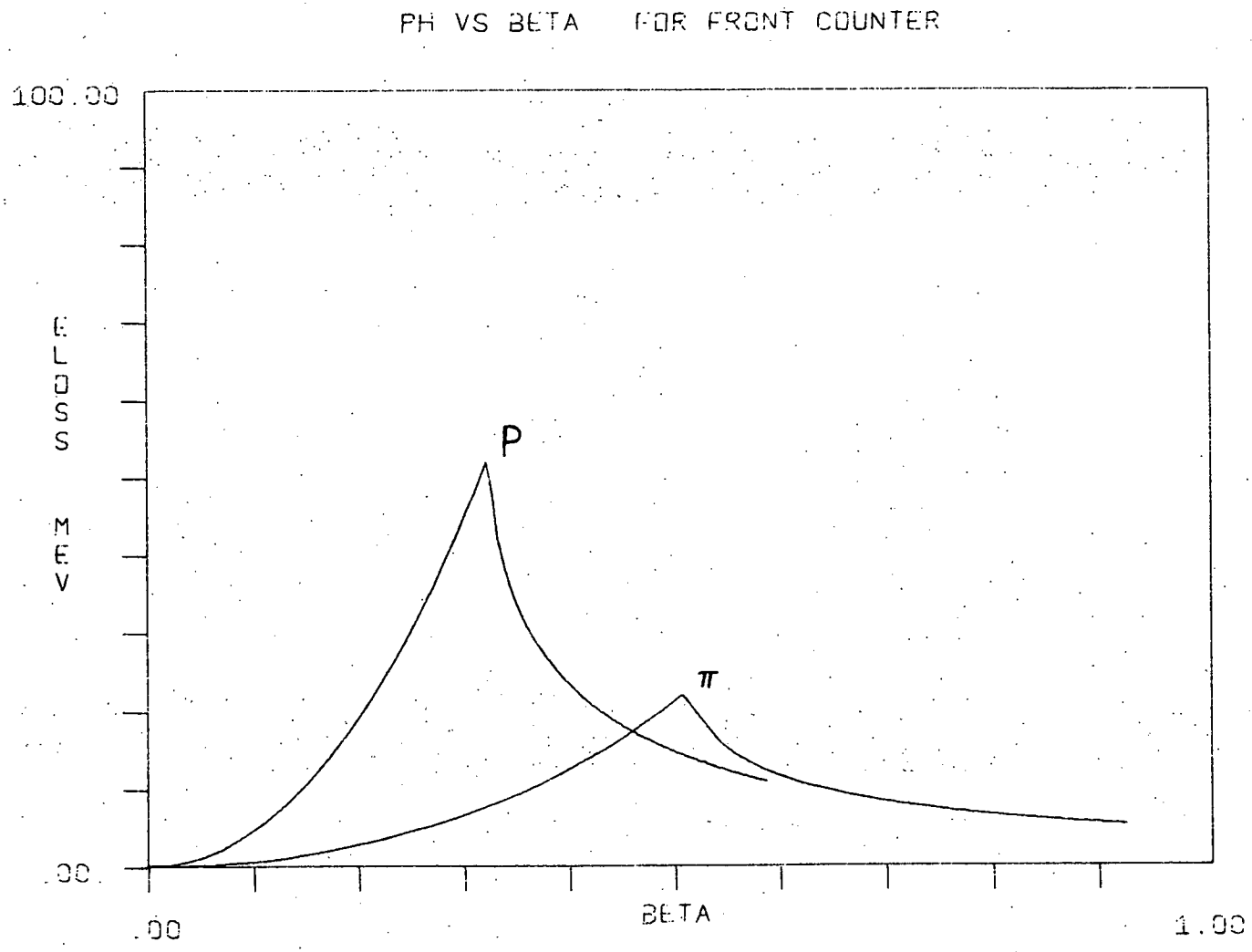
PH VS BETA FOR FRONT COUNTER
100.00
ELOSS MEV
.00
P
π
.00
BETA
1.00

vertex, $(Z_v - Z_{B1})$ is the distance the beam travelled from the start signal (at B1) to where it interacted, and T_{B1} is the delay of the start signal from B1, due to cables and logic. The distance from where the track intersects the counter to the top end of the scintillator is y, and V_s is the velocity of signal propagation through the counter. D_t is a constant summing up all the delays from cables and electronics.

Similarly we may write the time for the bottom tube as

$$T_b = Tof + (Z_v - Z_{B1})/c + T_{B1} + (L-y)/V_s + D_b,$$

where L is the length of the scintillator.

If we take the difference of the two times, we get

$$\Delta T = T_t - T_b = 2y/V_s + (D_t - D_b - L/V_s).$$

This equation tells us that the position where the track hits the counter may be arrived at just from the time difference. In Figure 19 we show, for a typical counter, the difference in y determined by this method and by the track reconstruction. The half width is less than 2 cm, and using the determined value for V_s of about 14 cm/ns, we see this corresponds to an error of less than 0.15 ns. (The resolution of the TDC was 0.1 ns).

If we average the two times, the y dependence drops out, and we have

$$(T_t + T_b)/2 = Tof + (Z_v - Z_{B1})/c + T_{B1} + L/2V_s + (D_t + D_b)/2,$$

or

$$Tof = (T_t + T_b)/2 - T_{B1} - (Z_v - Z_{B1})/2c + D$$

where D is just the total of all those constants.

Fig. 19. The difference in y positions of a recoil track as measured by a typical recoil scintillation counter and by extrapolation from the recoil wire chambers.

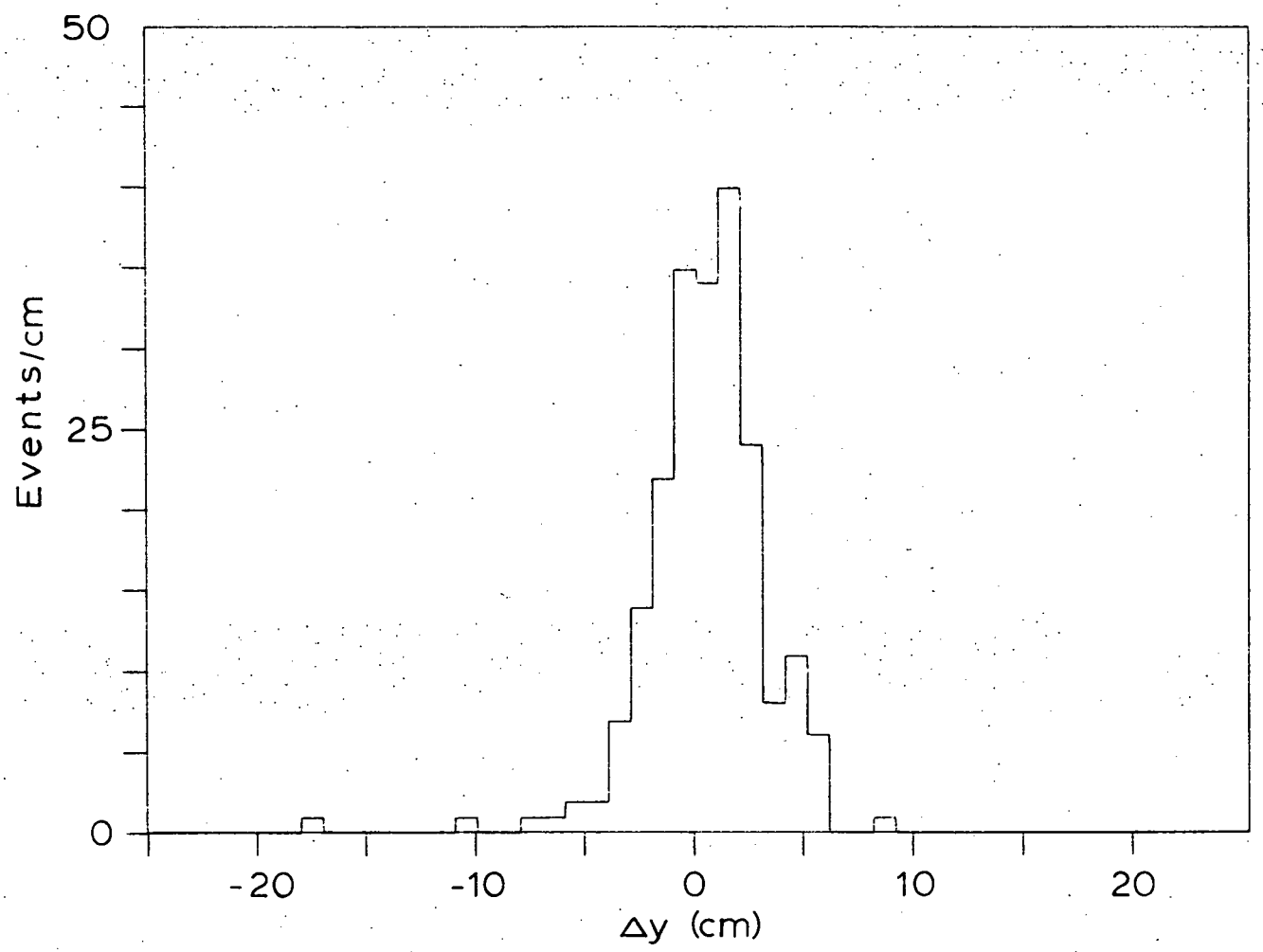
50
25
0
Events/cm
-20
-10
0
10
20
Δy (cm)

During the running of the experiment, we attempted to measure D by moving the recoil time of flight window to accept elastic pions(β=1); however we appear to have failed in lowering the discriminator level enough to accept minimum ionizing particles. The method finally used for this calibration was to compare the pulse height measurements with calculated energy loss expected in the counter. I used momentum range tables (Measday and Serre, 1969) to calculate the energy loss and plotted this against the pulse height average of the two tubes. The constant, D, was varied until the two maxima coincided. This calibration is probably good to about 0.5 ns. Figure 20, showing the measured pulse height of the recoil versus velocity, agrees quite well with our previous estimates (Figure 18).

The energy loss for pions and protons travelling faster than 12cm/ns is about the same, and in this region they become indistinguishable, unless we increase the absorber thickness. Behind the front layer of scintillator we had a half inch of aluminum and another inch of scintillator. The expected energy deposited in the second scintillator is shown in Figure 21 for both protons and pions. The efficiency of the back layer seems to have been too low to do us much good. It was ignored in the analysis.

The square of the mass recoiling against the proton has been calculated and plotted in Figure 22. The smooth curve is from a Monte Carlo done by G. Ascoli and is normalized to the data. The agreement is quite good, except for the missing low mass peak. This peak comes from three pion events which have been

Fig. 20. Measured pulse height as a function of velocity.

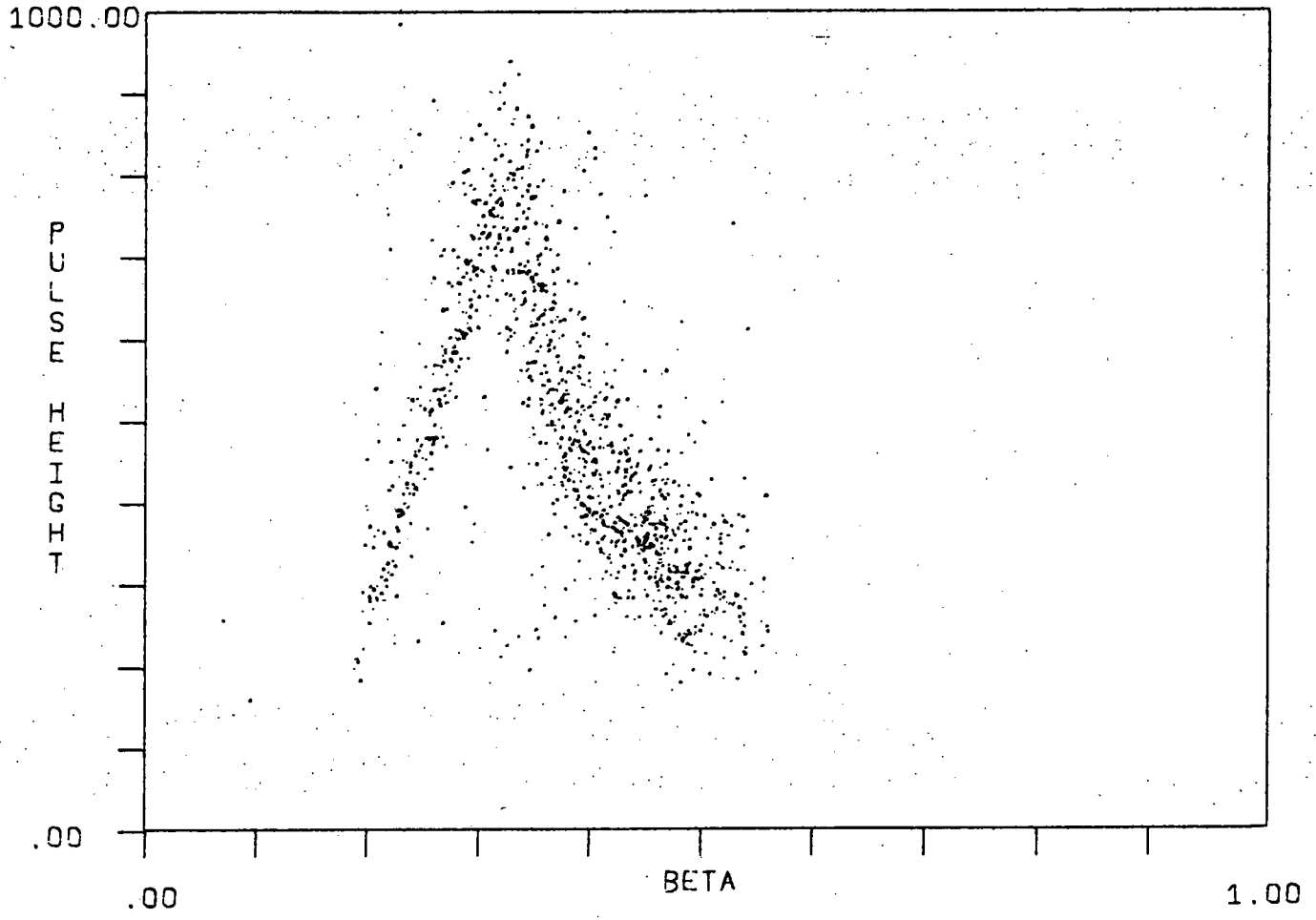
1000.00
PULSE HEIGHT
.00
.00
BETA
1.00

Fig. 21. Calculated energy loss in the back layer of recoil counters as a function of velocity for protons and pions.

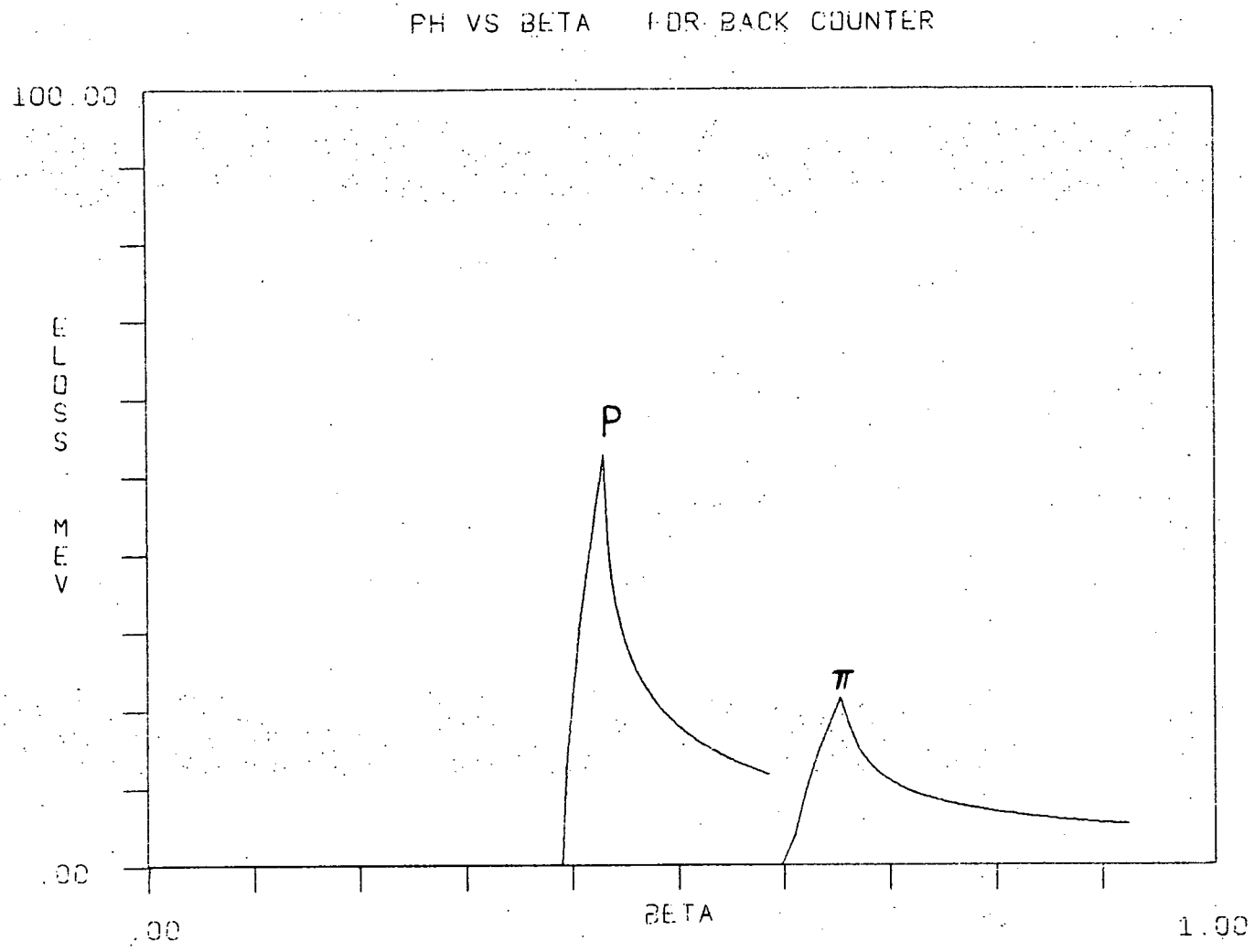
PH VS BETA FOR BACK COUNTER
100.00
ELOSS MEV
.00
P
π
.00
BETA
1.00

Fig. 22. Square of the mass recoiling against the proton. The histogram is a sample of the "1MUP" data and the curve is from a Monte Carlo using the proton diffractive cross section with no muon requirement. The curve is normalized to the data.

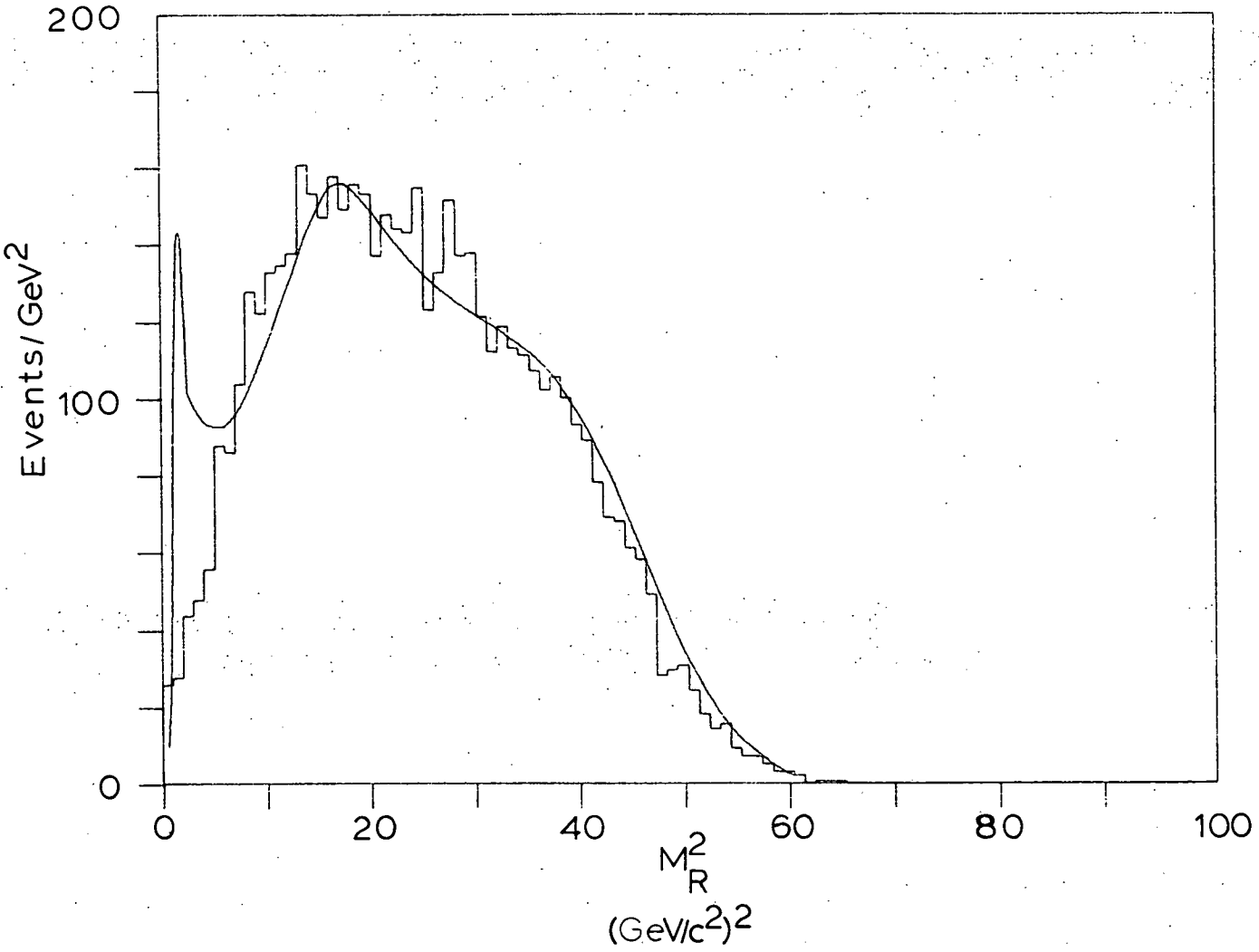
200
100
0
Events/GeV^2
0
20
40
60
80
100
M_R^2
$(GeV/c^2)^2$

discriminated against by the trigger. The Monte Carlo used the recoil proton geometry and trigger requirement, but it had no muon requirement. The data, which had required a muon, correspond to an acceptance times cross section of about 10 μb, instead of the Monte Carlo acceptance times cross section of about 200 μb.

If we assume that our background trigger rate from the muon requirement was basically due to pions decaying in flight and to hadrons punching through the hadron absorber, we estimate a maximum partial acceptance for these bogus muon events of about 5%.

CHAPTER 5

Preliminary Analysis

5.1 Track Reconstruction

Track reconstruction of the E369 data was done separately at Oxford University and at the University of Illinois; however the results of this paper come only from the Illinois version. The basic skeleton of both program versions came from the E398 collaboration (Hicks, 1978), also using the CCM spectrometer. M. Shupe and G. Ascoli revamped and added much of the code for the Illinois program, and new sections were also contributed by R. Raja, U. E. Kruse, and me. This program was constructed on the High Energy Physics PDP-10 and then transferred to the Cyber at the Digital Computation Lab. It took about 120 hours of Cyber CPU time to reconstruct the data for all events. I will give a brief description of the program's journey through an event.

First an event was read in from tape, and the hit positions in each chamber were converted from readout propagation times to length in 0.25 mm (The reason for these bizarre units is historical, and comes from the fact that the original CCM spectrometer analysis routines were written on a 16-bit computer in integer format). The 2x6 m^2 chamber sparks were then corrected for variations in speed of sound along the magnetostrictive ribbons.

Next we come to the track finding, which was carried out independently in the four regions: beam, recoil, upstream of the CCM, and downstream of the CCM.

The eight upstream 1x1 m^2 MWPC planes were scanned separately in x and y for track projections, requiring three out of four hits per projection.

The downstream spark chambers were searched for tracks consistent with stale beam tracks, and these hits were removed from the spark buffer. This was done because the combinations added by stale beam tracks tended to choke the track finder. Then the twenty planes were searched for tracks with at least three hits in each of the x and y projections. These tracks were also required to project upstream into a window 2.5m wide at the center of the CCM(z=0).

Next we scanned the recoil hodoscopes, looking for hits. If one was found we calculated a road through the chambers and searched for the track, requiring three out of four x-hits and at least one out of two y-hits. When a track was found, we fit the track using the nominal beam axis as an additional constraint in y. Then the recoil flight path length, and the time of flight were calculated.

We tried to fit the beam track using the MWPCs and hodoscopes shown in Figure 7. If the data was insufficient for a good fit, the the beam track was flagged as bad, and the fit was done using the beam envelope.

Fits of the interaction vertex were done separately in the x and y projections using the upstream tracks, the recoil track if one was found, and the beam track if it was not flagged as bad. The initial fit to the vertex assigned large weights to the recoil and beam projections when they existed. Successive fits were done

by removing the projection with the largest deviation in the previous fit, until all used projections were within a given tolerance. If there were less than two tracks left at this point, we did not find a vertex, and the event was subsequently removed from the data set. The removal process was then reversed to allow for a shift in the fitted vertex. This was done by adding, one at a time, any previously removed projection within tolerance until no more could be added. Finally we fit the vertex in each projection with equal weights for all tracks, including the recoil and beam tracks. The z for the vertex was calculated by a weighted average of the z's from both projections.

If we were previously unable to do a good beam fit, but a good vertex was found, then we used the vertex information to find a better beam track.

We then used the vertex to look for track projections coming from the vertex but with only two hits per projection in the upstream 1x1 m^2 MWPCs.

Next we linked the downstream tracks to the upstream projections, including those which missed the primary vertex, using a cylindrical hard edge approximation for the magnetic field (Pordes, 1976). The MWPC planes in the magnet were scanned for hits, and the downstream hodoscopes were checked to see if each track was in time. If a downstream track was lacking any upstream projection, the missing projection was fabricated by assuming the track came from the interaction vertex. These linked tracks were then refitted using all hits upstream, downstream, and inside the CCM, and a parameterization of the CCM field.

Any left over upstream projections were projected into the CCM planes, which were scanned for hits in order to find low momentum tracks that were swept away from the downstream chambers by the CCM.

Finally the tracks, momentum, timing data, scalers, lead glass data, recoil, and Cerenkov data were written to magnetic tapes. These output tapes were then read into the PDP-10 and converted from Cyber 60-bit word format to PDP-10 36-bit word format. The results of this conversion were transferred to another set of tapes.

5.2 Particle Identification

The next step in the analysis was to feed the reconstructed tracks through a program written by D. Bender and E. Smith, which looked for neutral particles decaying between the interaction vertex and the 1x1 m^2 MWPC's. Their program used the 18 cell Cerenkov counter to identify charged particles as either pions or kaons. The Cerenkov algorithm was developed by Smith and Sard, and will be covered in more detail in Smith's thesis; however I will give a brief summary of its function since it was a crucial part of my analysis.

For a charged particle travelling in a medium with refractive index r, the angle, θ_c, between the Cerenkov radiation and the particle's trajectory is given by (Jackson, 1962)

$$\cos\theta_c = 1/(\beta r)$$

where βc is the particle's velocity. There is no radiation when this cosine is greater than one. The intensity of the radiation is proportional to $\sin^2(\theta_c)$, so we may write the ratio of light

intensity of a particle of velocity βc to that of a particle with $\beta=1$ as

$$R = \frac{1 - 1/(\beta r)^2}{1 - 1/r^2}$$

The average number, $\bar{n}$, of photoelectrons emitted from the cathode is proportional to the radiated Cerenkov light. We may write this as $\bar{n} = \bar{n}_o R$, where $\bar{n}_o$ is the average number of photoelectrons seen for a particle with $\beta=1$.

The number of photoelectrons was assumed to follow the Poisson distribution and the gain A, of the photo tube was assumed to be Gaussian with mean $\langle A \rangle$ and variance σ_A^2. These assumptions yield a probability distribution,

$$P(y) = \sum_{n=1}^{\infty} e^{-\bar{n}} \frac{\bar{n}^n}{n!} \frac{1}{\sqrt{2\pi n}\,\sigma_A} e^{-\frac{(y - n\langle A \rangle)^2}{2 n \sigma_A^2}},$$

for the expected pulse height, y, in the photo tube.

For each particle track that was found we identified which Cerenkov cell, if any, the track passed through, and then using the parameters, $\bar{n}_o$, $\langle A \rangle$, and σ_A for that cell, we calculated the ratio, $R(K/\pi)$, of the probability that the particle was a kaon to the probability that it was a pion.

Smith's algorithm also looked at cases where the Cerenkov circle fell onto more than one cell, and it calculated the fraction of light reflected by each mirror. When more than one track went through the same cell the pulse height was calculated, using each possible configuration of particle types, to find the most probable hypothesis. The ratio was calculated for each track using the best identification for all the other tracks hitting the cell. Figure 23 shows the raw pulse height distribution for a

Fig. 23. Raw pulse height distribution for all 18 cells of the Cerenkov counter for a sample of the data.

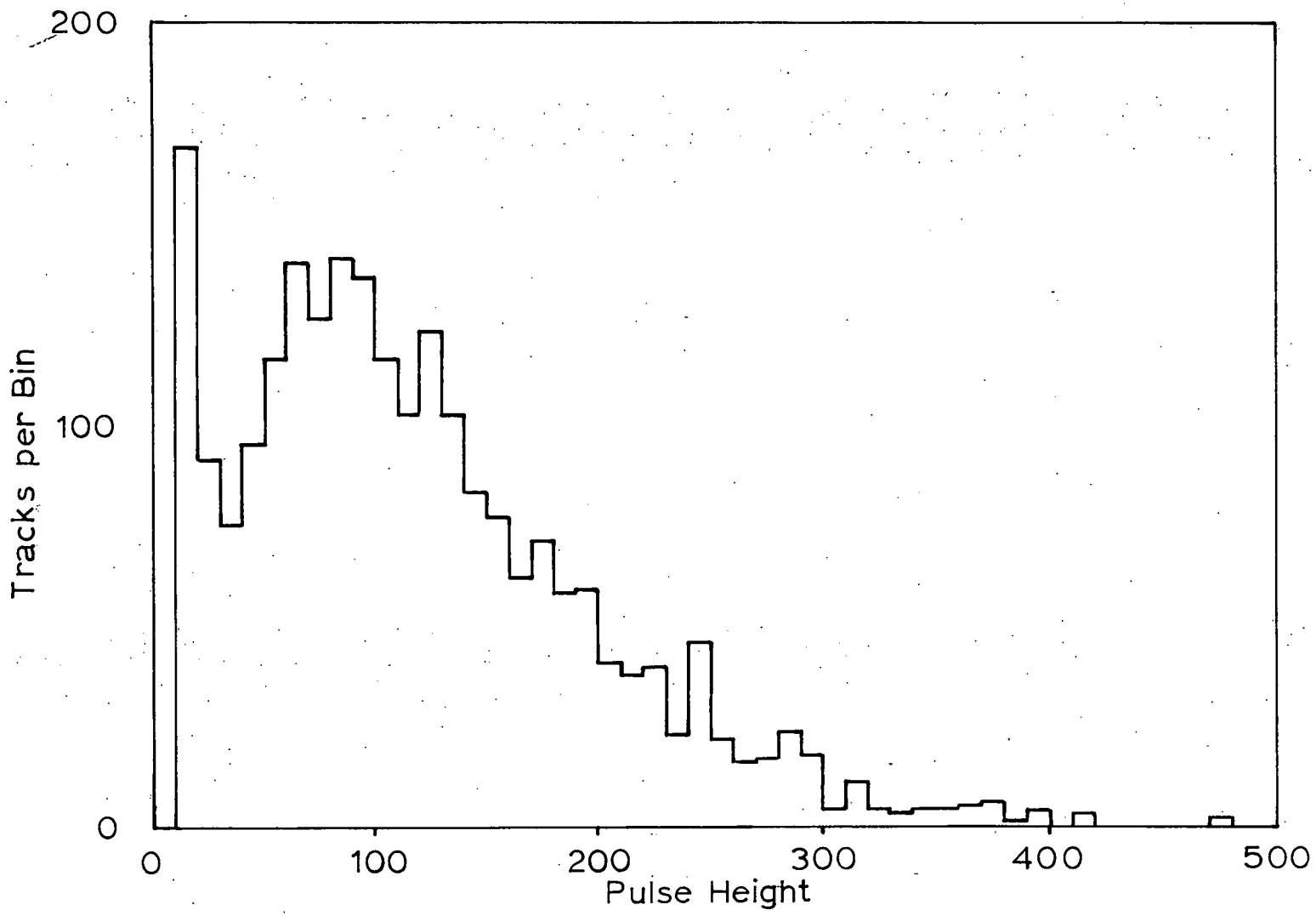
200
100
0
Tracks per Bin
0
100
200
300
400
500
Pulse Height

sample of the data in all 18 cells. Smith determined that $\bar{n}_o$ varied between 2 and 4 photoelectrons from cell to cell. A scatter plot of track momentum versus R(K/π) is shown in Figure 24. We found that requiring tracks to have R(K/π)>0.25 gave the best discrimination between K's and π's.

Having transformed the raw data into a usable form of momenta and trajectories of identified particles, we were now ready to start the actual particle search.

Fig. 24. Scatter plot of track momentum versus R(K/π) for a sample of the data.

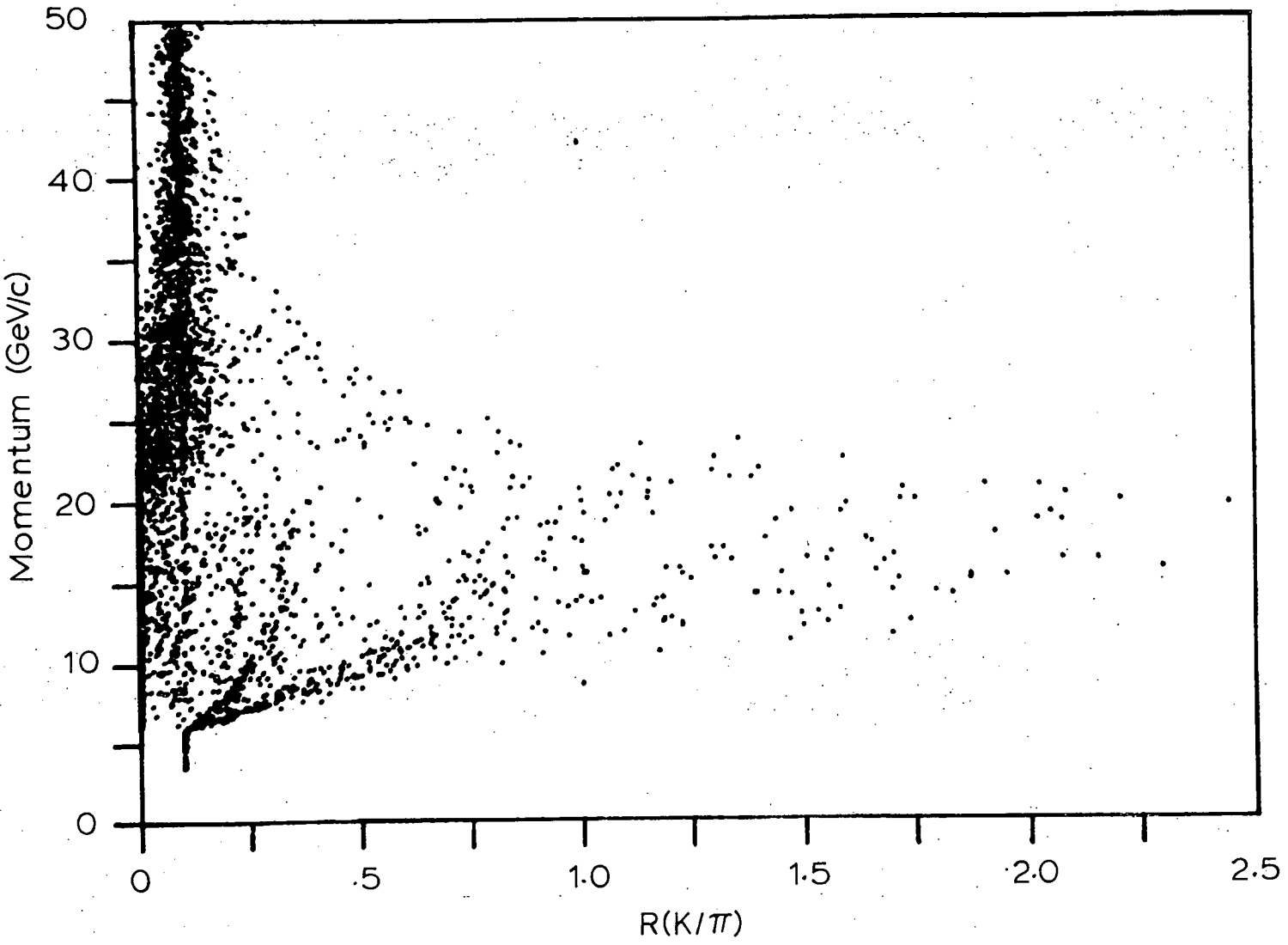
50
40
30
20
10
0
Momentum (GeV/c)
0
.5
1.0
1.5
2.0
2.5
R(K/π)

CHAPTER 6

Final Analysis and Discussion of Data

In this chapter I describe the cuts used to reconstruct the D signals. Then momentum and angular distributions are compared with diffractive and gluon fusion models. The diffractive model agrees more closely with the results and is used to evaluate the cross section. Finally I compare the results with other experiments.

6.1 Kinematic Definitions

In order to explain the cuts and the interpretation of the data, we need the following definitions. Figure 25 shows the basic reaction considered and defines the incoming and outgoing four-momenta. The reconstructed D is labelled D_1, and D_2 is assumed to decay semileptonically. The four-momentum of the target proton is written as $\vec{m}_p$ to signify that it is at rest in the lab.

The invariant momentum transfer to the proton is

$$t_p = (\vec{m}_p - \vec{P}_p)^2,$$

and

$$M_R^2 = (\vec{P}_{\pi} + \vec{m}_p - \vec{P}_p)^2$$

is the square of the mass recoiling against the proton. Our trigger required that

$$3\text{GeV}/c^2 < M_R < 6.5\text{GeV}/c^2 \quad \text{and} \quad -0.1\text{GeV}^2 > t_p > -0.4\text{GeV}^2.$$

For a real $D\bar{D}$ event, M_R should be greater than 3.7 GeV/c^2, the rest mass of a D pair. The mass squared left over after the momenta from the recoil proton and D_1 have been subtracted is

Fig. 25. Schematic diagram defining four-momenta for the reaction

$$\pi^- + p \longrightarrow p + D_1 + D_2 + X.$$

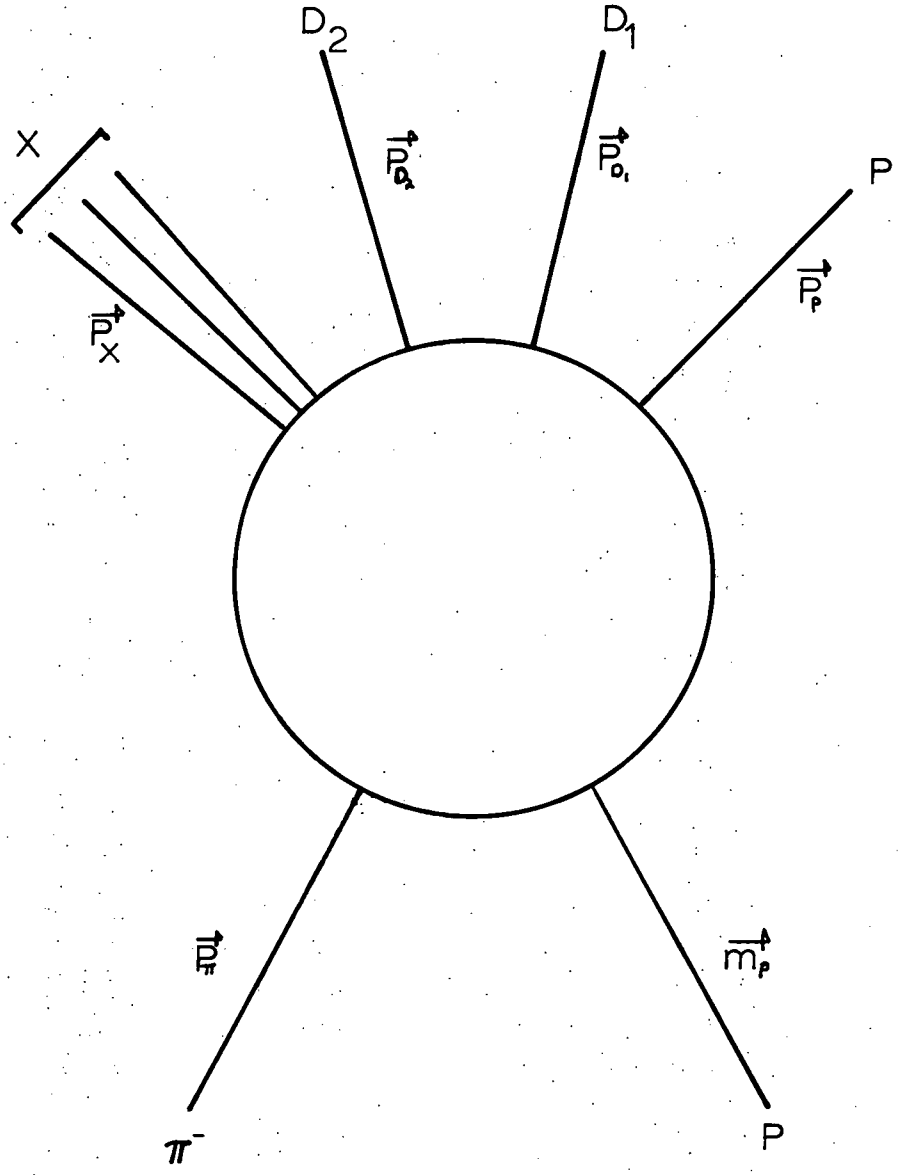
D2
D1
X
P
$\vec{P}_{D_2}$
$\vec{P}_{D_1}$
$\vec{P}_X$
$\vec{P}_P$
$\vec{P}_{\pi^-}$
$\vec{m}_P$
π^-
P

$$M_L^2 = (\vec{P}_\pi + \vec{m}_p - \vec{P}_p - \vec{P}_{D_1})^2,$$

and M_L should be at least as large as the D mass. Since the recoil proton time of flight determination has large errors, M_R and M_L will have large errors. The cuts made with them were very liberal. The invariant momentum transfer to D is defined by

$$t_{D_1} = (\vec{P}_\pi - \vec{P}_{D_1})^2,$$

which is plotted later to see if the production looks diffractive.

6.2 Cuts and Mass Plots

The first cut I made on the data was to require that the trigger latch bits indicated an interaction in the hydrogen target only and that it was a "1MUP" trigger. I also required that there be a single reconstructed recoil track. Of the events which passed the trigger bit cut, 70% had a single reconstructed recoil track and 4% had two or more recoil tracks. The remaining 26% had no recoil track. This low efficiency is indicative of the problems we had with noise from our spark chambers which frequently fouled up the signals from many of our chambers, and sometimes even zapped the on-line computers. Most of the events with no recoil track had other hardware errors.

The downstream tracks were found with high efficiency (>95%). The upstream tracks were not always linked through the magnet correctly. The mid magnet MWPC planes were about 50% efficient and sometimes gave hits in the wrong places. Consequently, the hits in the CCM planes occasionally told us to link the wrong upstream x and y projections together. The corresponding downstream track would then not link in one projection, and so an upstream projection would be fabricated for the downstream track.

When an observed upstream x-projection matched the fabricated x-projection for a downstream track, we essentially ended up with two tracks of the same momentum. This tended to produce funny looking spikes in the mass plots. By ignoring the track stubs with no downstream links, I was able to make plots with smooth and reasonable looking backgrounds.

I made the following cuts on the data:

1. that $M_R^2 > 0$,
2. that the proton momentum $P_p < 0.63$ GeV/c,
3. that any downstream track with a momentum above 200 GeV/c should be ignored,
4. that the number of final in-time tracks be between 4 and 10 tracks including the proton,
5. that the sum of the downstream track momenta be between 100 and 230 GeV/c, and
6. that the primary interaction vertex be inside the target.

Cut 1 removed events with recoil particles which could not be protons due to energy momentum conservation. Cut 2 required that the invariant momentum transfer to the proton, t_p, be greater than $-0.36(\text{GeV})^2$. This corresponded to a minimum time of flight cut of about 14.3 ns with more than 90% of the recoil particles being protons as can be seen from Figure 16. The third cut essentially removed any stale beam tracks. Cut 4 required the minimum number of final state particles to reconstruct a D event. Events with more than 10 tracks had large combinatorials and showed no signal enhancement. Cut 5 was not very stringent. It required that at least half of the energy of an event be accounted for, and that this did not exceed the beam energy.

In addition to the above cuts, I required: 7)that the net charge seen in the event be zero, and 8)that there were no track stubs (without downstream links) in the event. These two cuts were rather stringent and picked out events which were diffractive in nature. A ninth cut was made for the charged $K\pi\pi$ channels which required the square of mass recoiling against the proton and $K\pi\pi$ combination to be non-negative, $M_L^2>0$.

Figures 26 and 27 show, respectively, the $K^+\pi^-\pi^-$ and $K^-\pi^+\pi^+$ mass spectra with all the above cuts. Note the peaks in both channels at the known D mass (1868 MeV/c^2). No such signal can be seen in the two non-exotic channels shown in Figures 28 and 29. These channels correspond to the Cabibbo suppressed decays. The combined D^+ and D^- data are shown in Figure 30 along with a maximum likelihood fit to a Gaussian signal plus a background given by a constant plus an exponential. The width (36.6 MeV/c^2) is consistent with the resolution of the spectrometer. The mass (1877±4 MeV/c^2) agrees with the known mass within the tolerance of our alignment. Similar fits for the individual channels with the mass and width constrained are shown in Figures 31 and 32.

Figure 33 shows the sum of the D^o and $\overline{D^o}$ channels, $K^-\pi^+$ and $K^+\pi^-$. The lack of signal in this plot corresponds to an upper limit of 3.7 events at a 90% confidence level.

If this is really diffractive production, almost everything should go through the spectrometer to the downstream chambers. We should not expect cuts 7 and 8 to make much difference in the signal if the production is diffractive. On the other hand, if the production is central we should expect to see more signal when

Fig. 26. The $D^-(K^+\pi^-\pi^-)$ channel invariant mass plotted in 40 MeV/c^2 bins with no stub events and net charge of zero.

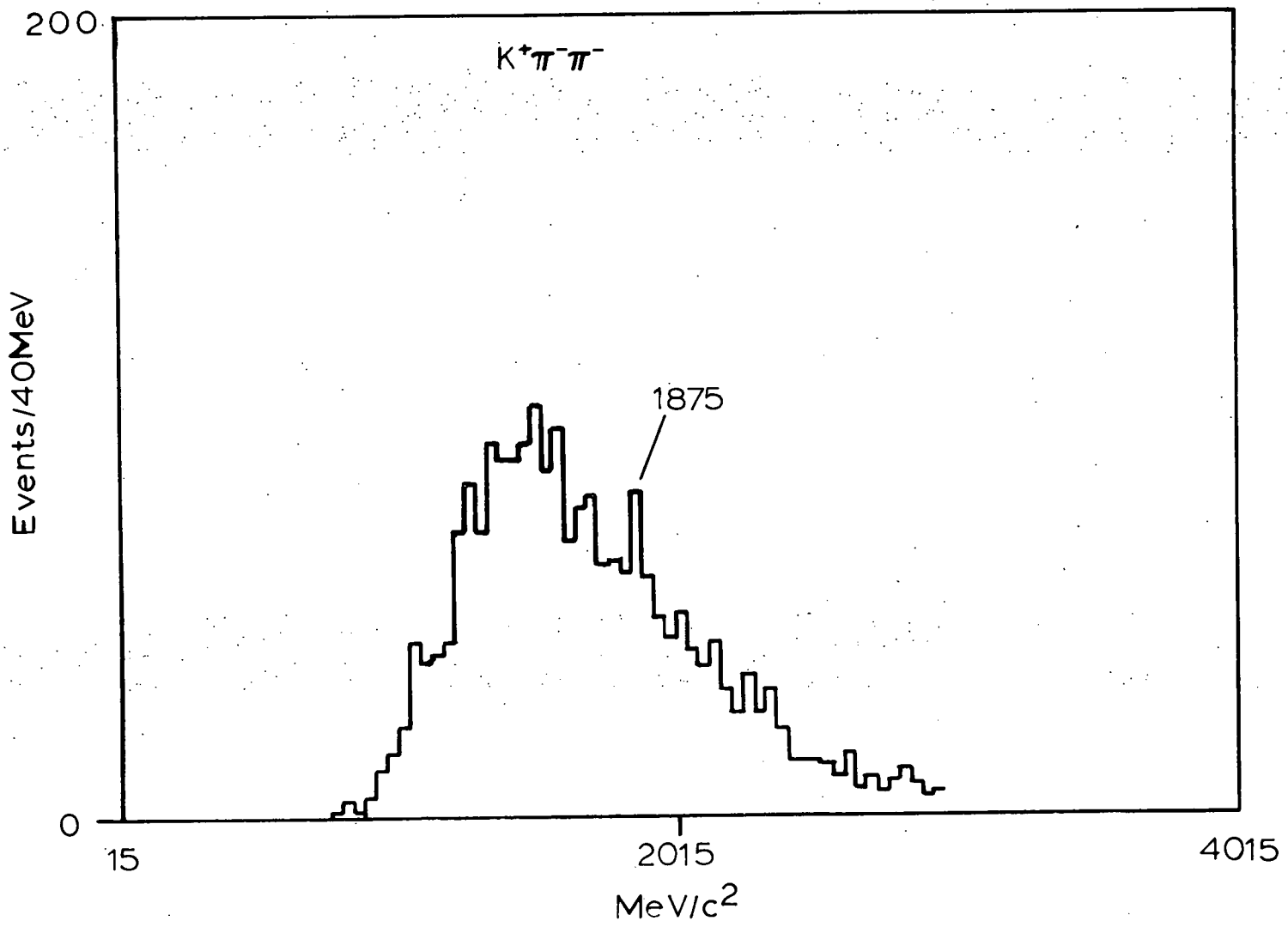
200
$K^+\pi^-\pi^-$
Events/40MeV
1875
0
15
2015
4015
MeV/c^2

Fig. 27. The $D^+(K^-\pi^+\pi^+)$ channel invariant mass plotted in 40 MeV/c^2 bins with no stub events and net charge of zero.

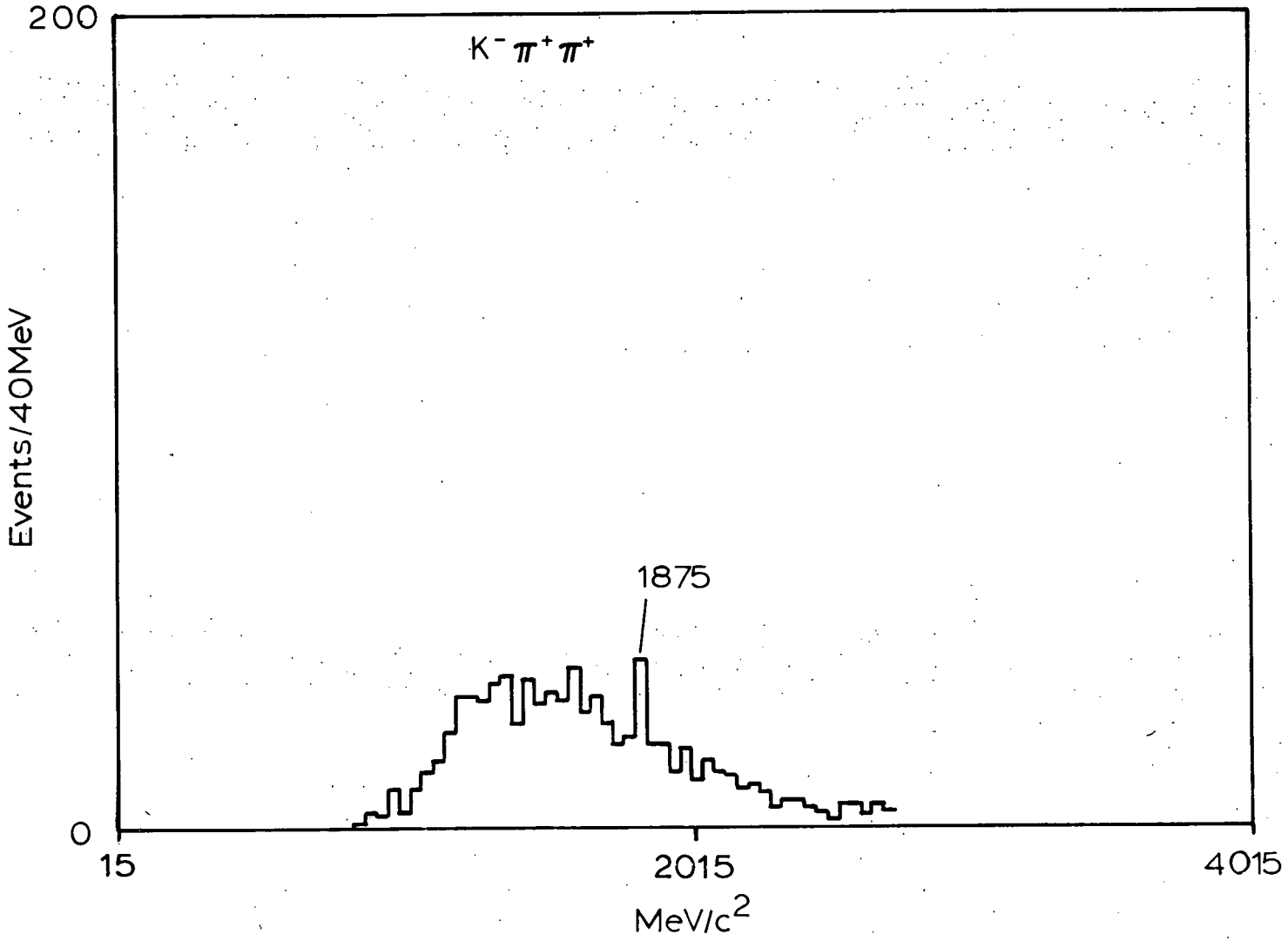
200
$K^- \pi^+ \pi^+$
Events/40MeV
1875
0
15
2015
4015
MeV/c^2

Fig. 28. The non-exotic $K^+\pi^-\pi^+$ channel invariant mass plotted in 40MeV/c^2 bins.

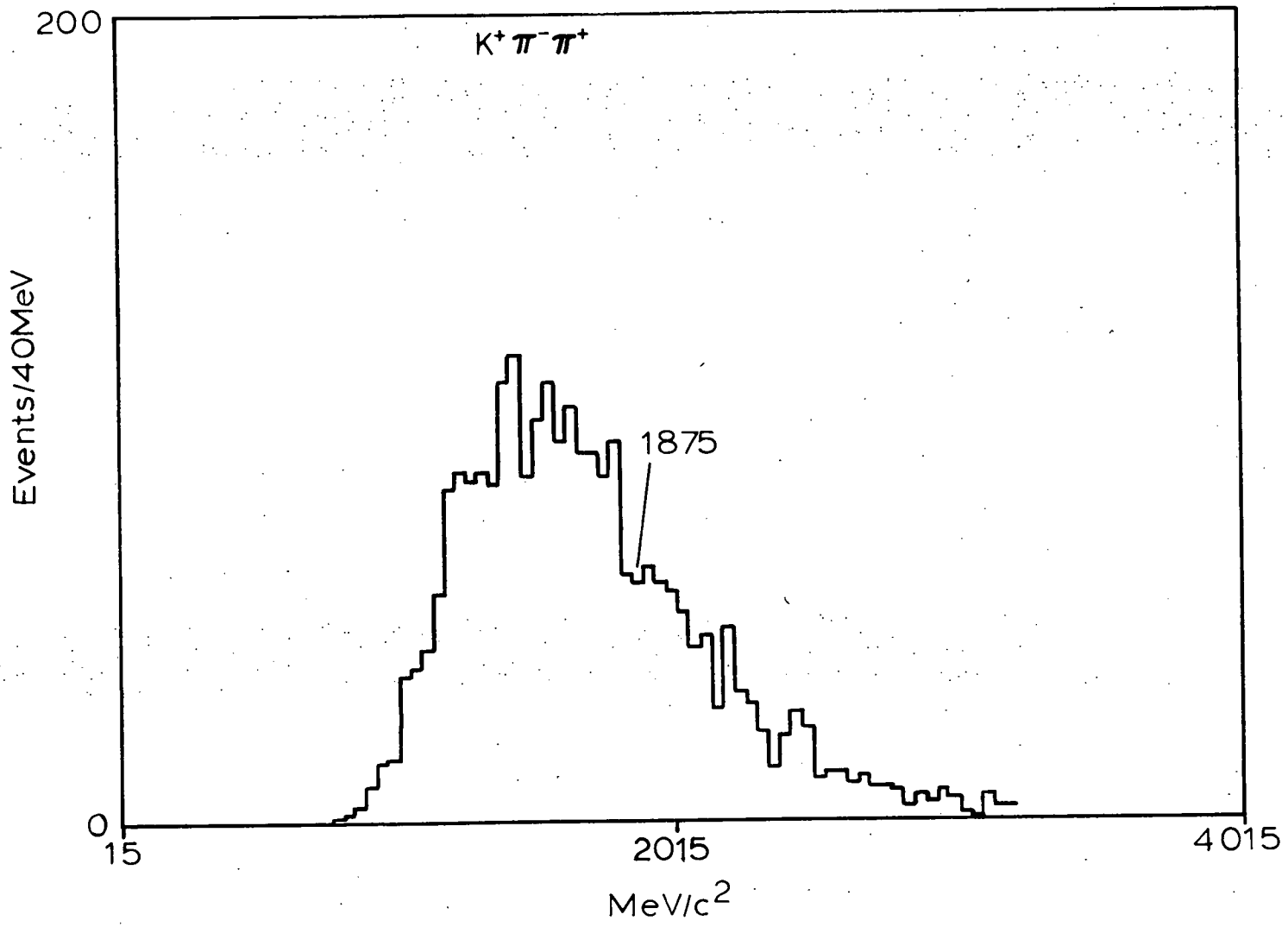
200
$K^+\pi^-\pi^+$
Events/40MeV
1875
0
15
2015
4015
MeV/c^2

Fig. 29. The non-exotic $K^-\pi^+\pi^-$ channel invariant mass plotted in 40MeV/c^2 bins.

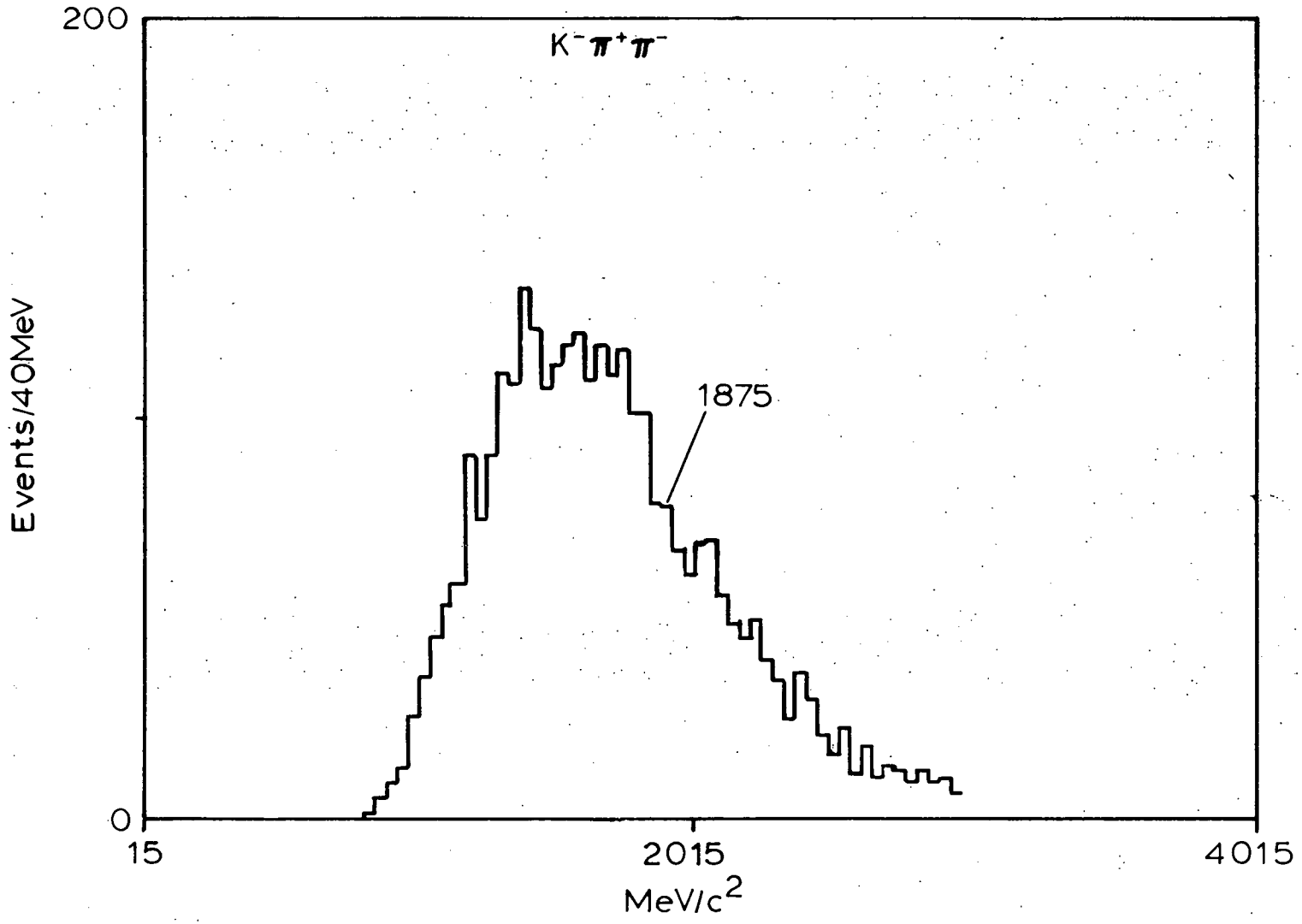
200
$K^-\pi^+\pi^-$
Events/40MeV
1875
0
15
2015
4015
MeV/c^2

Fig. 30. The invariant mass for both charged D channels ($K^{\pm}\pi^{\mp}\pi^{\mp}$) plotted in 20MeV/$c^2$ bins. The curve is the maximum likelihood fit. The fit gave the mass and width to be M=1877±4 MeV/c^2 and Γ=36.6±8.8 MeV/c^2, respectively. The amount of signal was determined to be 50±12 events.

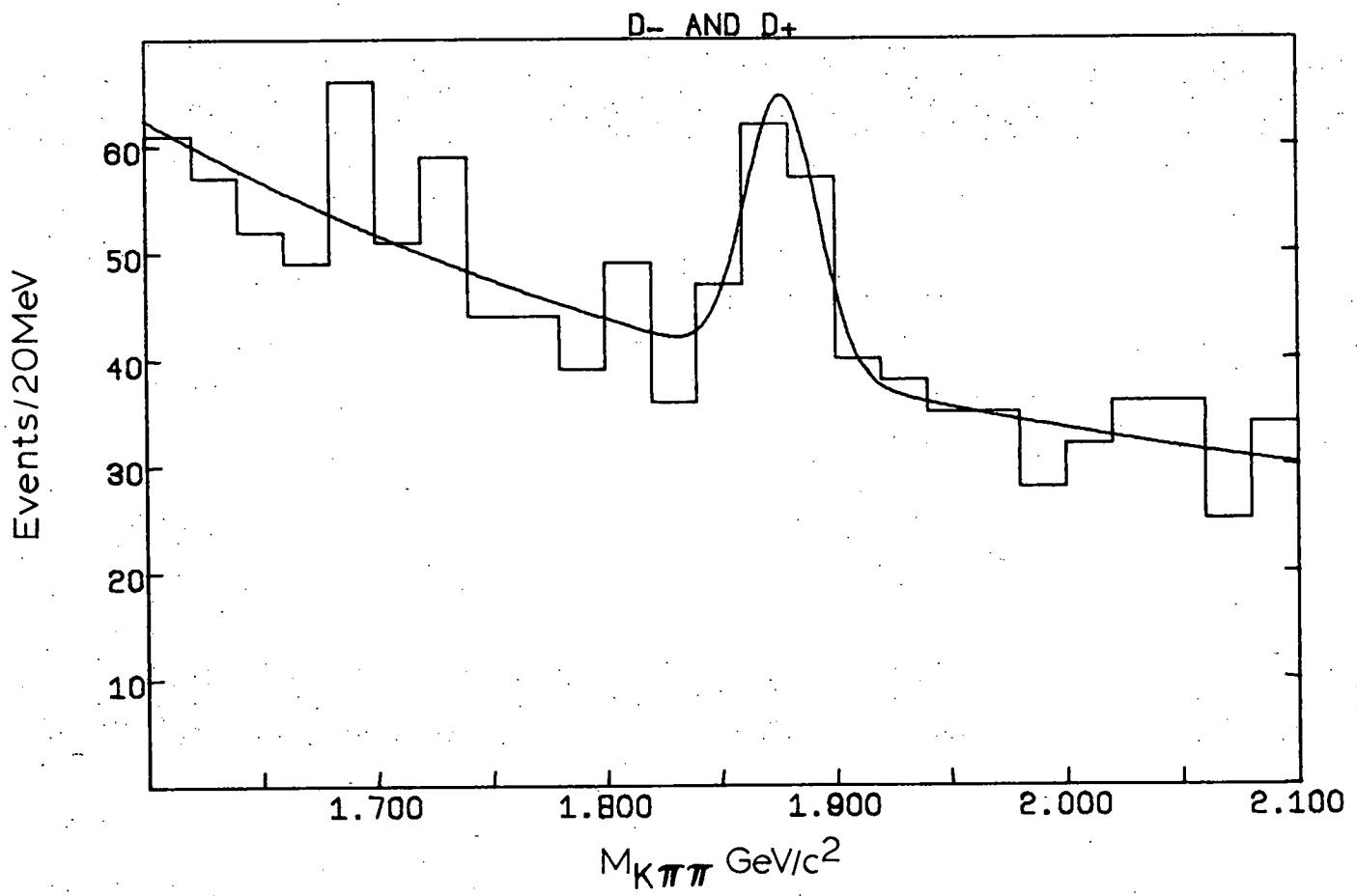
D- AND D+
Events/20MeV
60
50
40
30
20
10
1.700
1.800
1.900
2.000
2.100
$M_{K\pi\pi}$ GeV/c^2

Fig. 31. The $D^+(K^-\pi^+\pi^+)$ channel invariant mass in 20 MeV/c^2 bins with a maximum likelihood fit. For the fit, the mass and full width were constrained to be M=1877 MeV/c^2 and Γ=36.6 MeV/c^2, respectively. The area was determined to be 23±8 events.

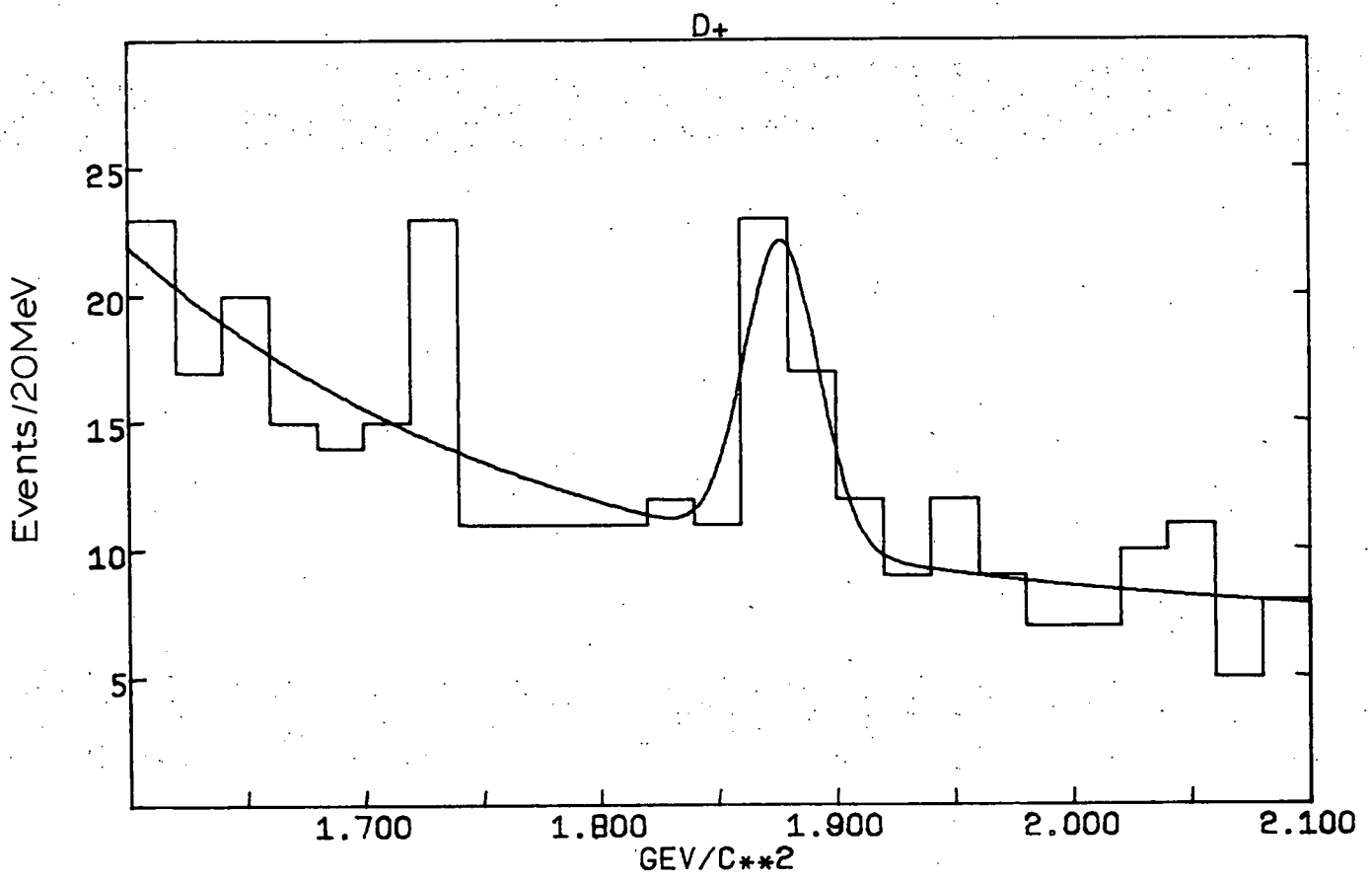
D+
Events/20MeV
25
20
15
10
5
1.700
1.800
1.900
2.000
2.100
GEV/C**2

Fig. 32. The $D^-(K^+\pi^-\pi^-)$ channel invariant mass in 20 MeV/c^2 bins with maximum likelihood fit. For the fit, the mass and full width were constrained to be M=1877 MeV/c^2 and Γ=36.6 MeV/c^2, respectively. The area was determined to be 26±10 events.

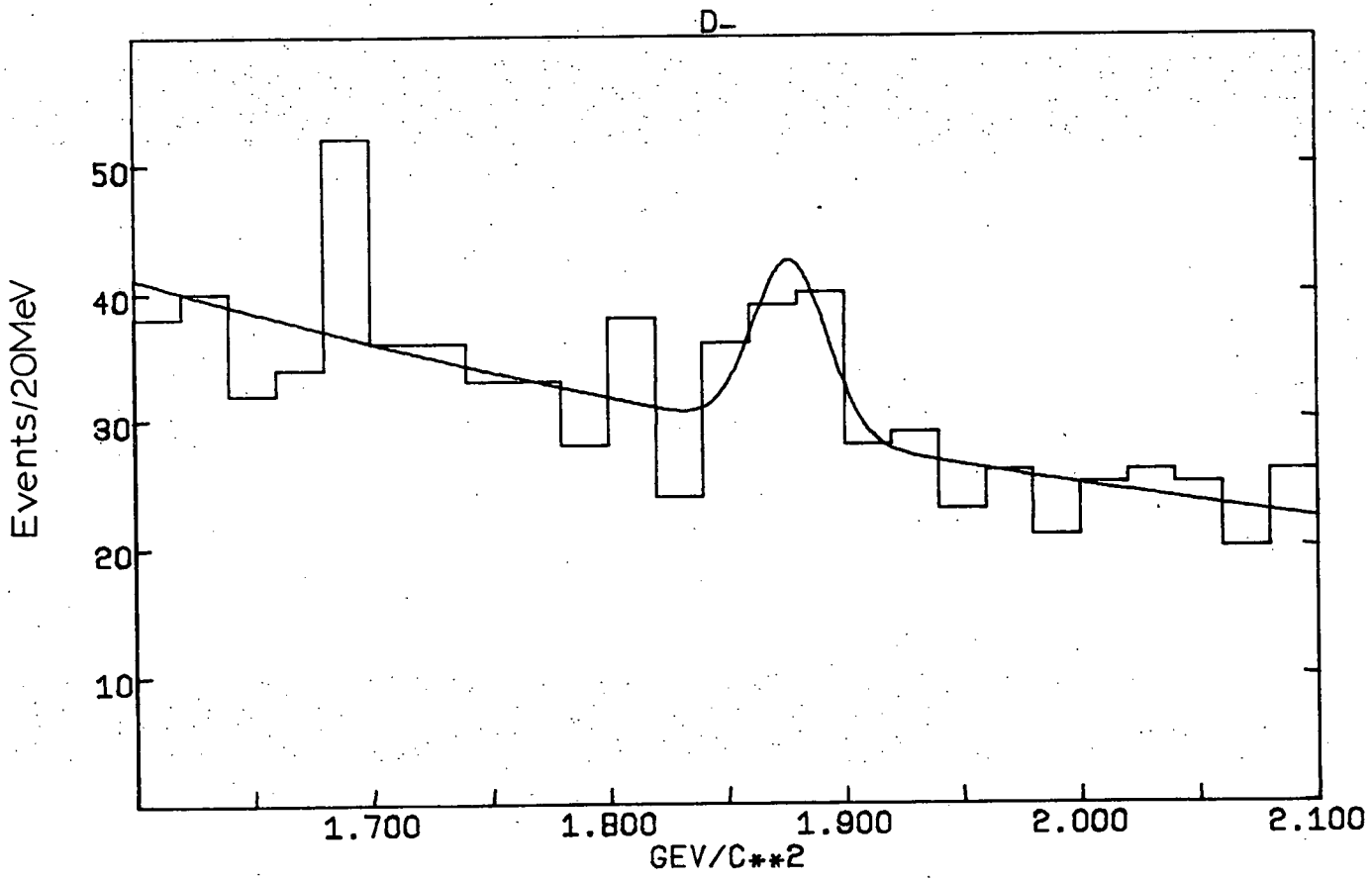
D-
Events/20MeV
50
40
30
20
10
1.700
1.800
1.900
2.000
2.100
GEV/C**2

Fig. 33. Both neutral D channels, D^0 ($K^-\pi^+$) and $\overline{D^0}$ ($K^+\pi^-$), plotted in 20MeV/c^2 bins with a fit of the background. This plot has an upper limit less than 3.7 events at a 90% CL.

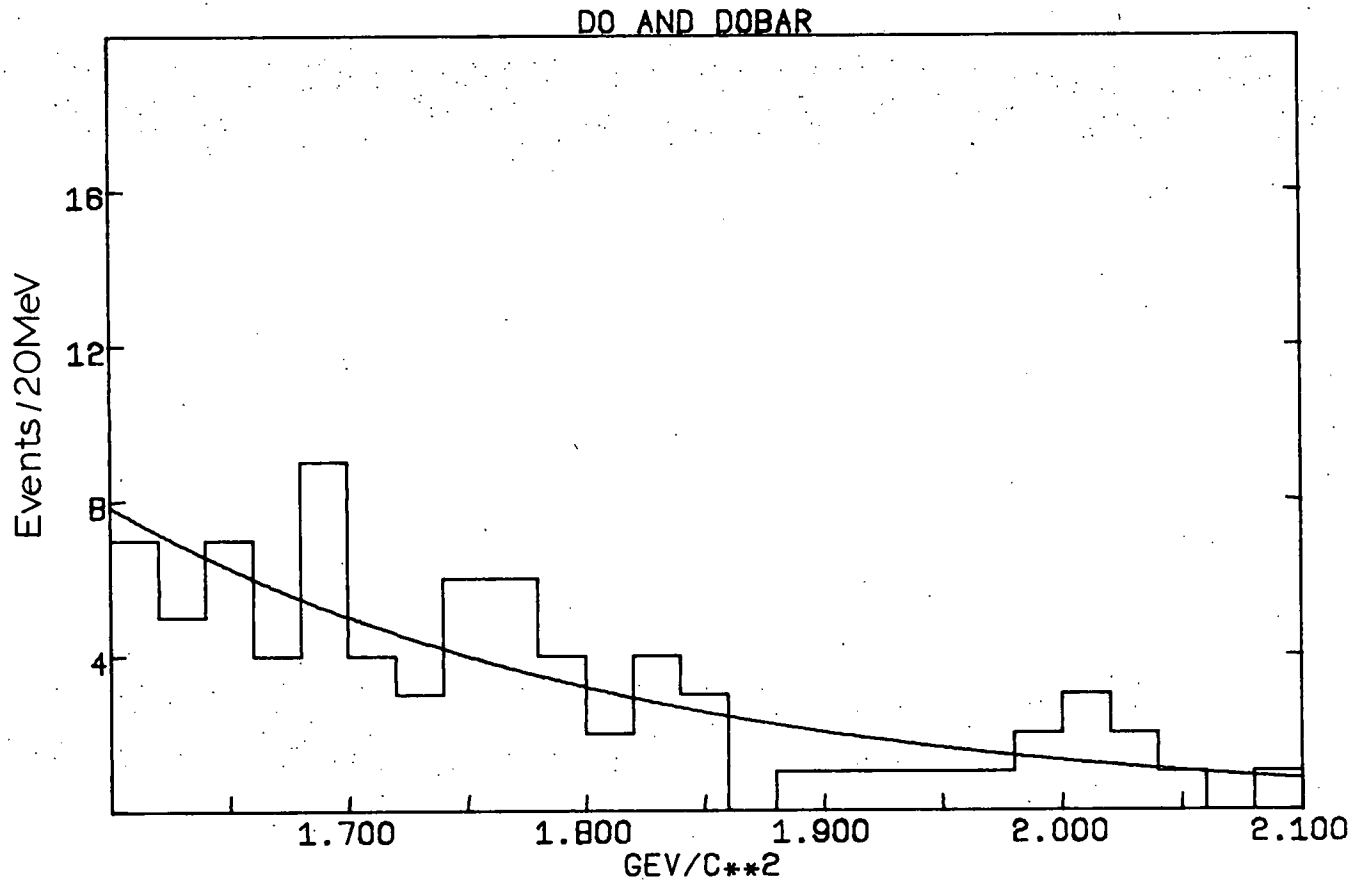
D0 AND D0BAR
Events/20MeV
16
12
8
4
1.700
1.800
1.900
2.000
2.100
GEV/C**2

these cuts are relaxed. The $K^{\pm}\pi^{\mp}\pi^{\mp}$ data are plotted in Figure 34 with cut 8 removed. Note that the number of background events is doubled while the signal remains the unchanged. In Figure 35 cut 8 is removed and cut 7 is relaxed to allow net charges of ±1 in the final state. Here the number of events is quadrupled without increasing the signal.

The results of these plots are summarized in Table 3. There are two things to note:

1. the almost equal amounts of the D^+ and D^-, and
2. the lack of neutral D signals.

This looks as though the D mesons are produced in a neutral pair, either (D^+D^-) or $(D^oD^{\overline{o}})$. Since the semileptonic branching ratio for D^+,

$$B(D^+ \longrightarrow \mu^- X) = 23\pm6\%,$$

is considerably larger than for D^o (Kirkby, 1979),

$$B(D^o \longrightarrow \mu^+ X) < 4\%,$$

our muon trigger requirement would suppress the detection of neutral D mesons. The ratio of the hadronic decay branching ratios,

$$B(D^o \longrightarrow K^-\pi^+)/B(D^+ \longrightarrow K^-\pi^+\pi^+) = 0.021/0.045 = 0.5,$$

(Kirkby, 1979) together with the semileptonic ratio, gives an over all suppression of more than a factor of 10 in trigger efficiency of $(D^oD^{\overline{o}})$ relative to (D^+D^-) pairs.

The production of a D^oD^- pair can not be ruled out in the type of diffractive model described in section 6.4. The acceptance for $D^o \longrightarrow K^-\pi^+$ with $D^- \longrightarrow \mu^- K^o \overline{\nu}_\mu$ is about half that for

Fig. 34. Both charged D channels ($K^{\pm}\pi^{\mp}\pi^{\mp}$) in 10 MeV/$c^2$ bins including events with track stubs. For the fit, the mass and full width were constrained to be M=1877 MeV/c^2 and Γ=36.6 MeV/c^2, respectively. The area was determined to be 55±22 events.

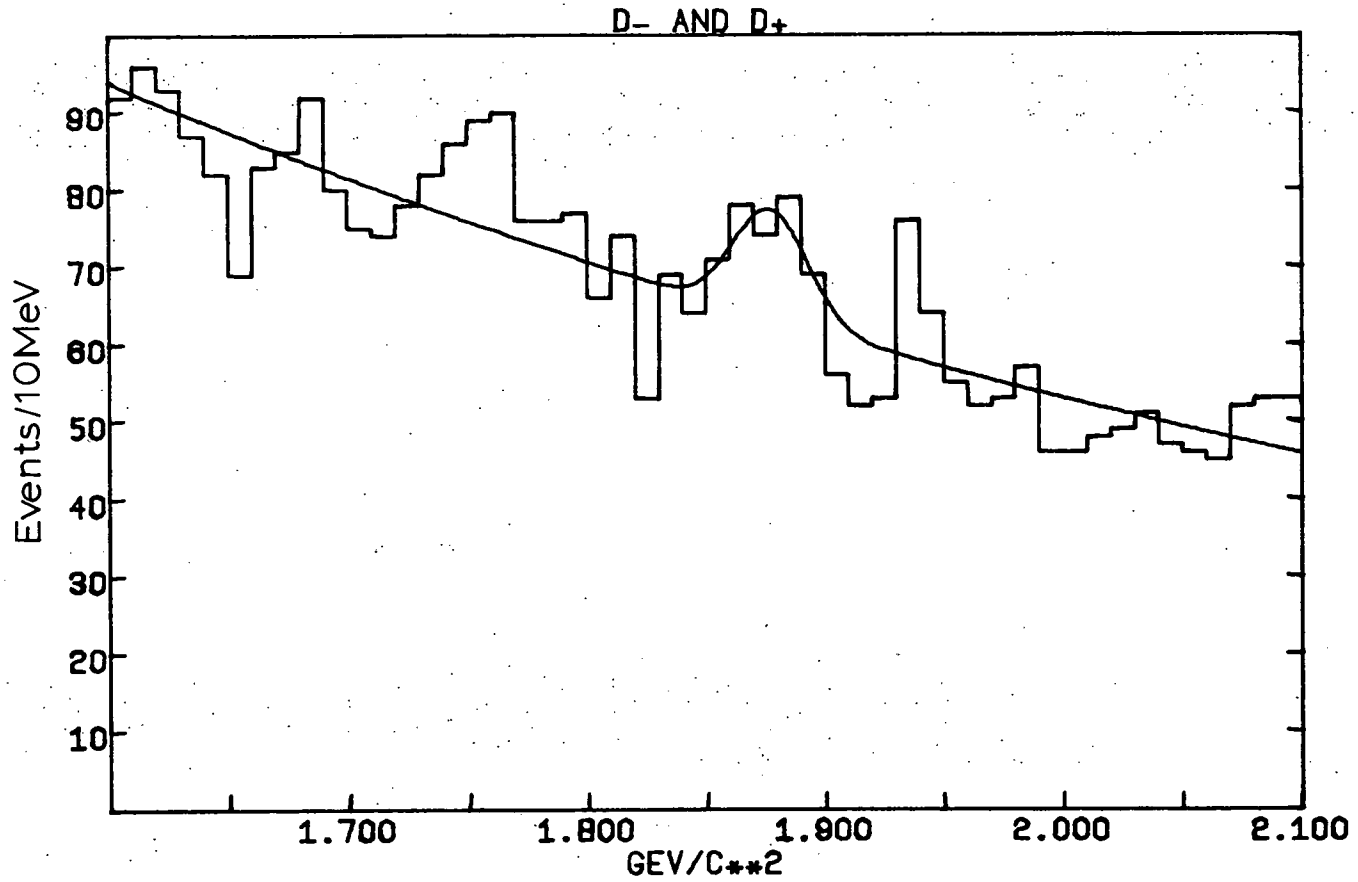
D- AND D+
Events/10MeV
90
80
70
60
50
40
30
20
10
1.700
1.800
1.900
2.000
2.100
GEV/C**2

Fig. 35. Both charged D channels ($K^{\pm}\pi^{\mp}\pi^{\mp}$) in 10 MeV/$c^2$ bins including events with track stubs and allowing a charge imbalance of ±1 in the final state. For the fit, the mass and full width were constrained to be M=1877 MeV/c^2 and Γ=36.6 MeV/c^2, respectively. The area was determined to be 49±27 events.

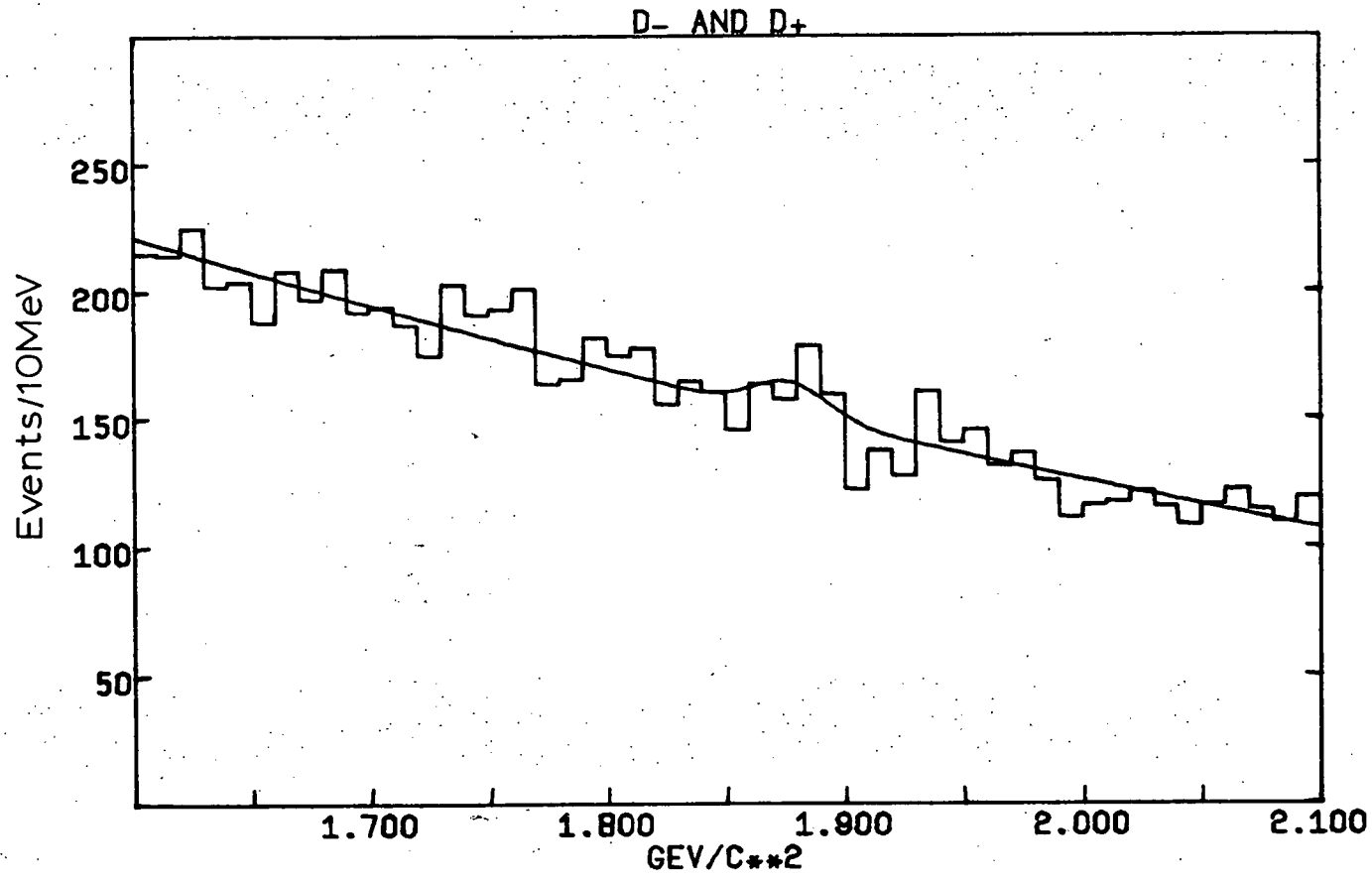
D- AND D+
Events/10MeV
250
200
150
100
50
1.700
1.800
1.900
2.000
2.100
GEV/C**2

TABLE 3

Summary of D Meson Data

Events with no stubs and net charge of 0:

Channel	# of events	Mass	Width
D^+ and D^-	50±12	1877±4MeV/c	37±9MeV/c
D^+	23±8	constrained	constrained
D^-	26±10	"	"
D^o and $\overline{D^o}$	< 4 at 90% CL		

Charged D Events with Stubs:

Net Charge	# of Events
0	55±22
+1, 0, -1	49±29

the D^+D^- mode. Using the relative acceptance and branching ratio, we should expect to see something like 6 D^0 events, if $D^0\bar{D}^0$ production occurs at a similar level to D^+D^- production.

6.3 Kinematic Distributions

Using the data from the signal bin in Figures 26 and 27 and the data in the bins to either side of the signal as background, I am able to make plots of relevant kinematic variables to test different production mechanisms. There is an excess of 40 events from both plots in the signal bin over a background of about 80 events.

The scaling variable, Feynman x, is defined by

$$x_F = P^*_{\parallel} / P^*_{max} ,$$

where $P^*_{\parallel}$ is the longitudinal component of momentum of the D in the center of mass system, and P^*_{max} is the maximum center of mass momentum that the D can have which is consistent with quantum numbers. This maximum occurs when the final state contains only a D meson and the lightest charmed baryon. I have used a mass of 2.285 GeV/c^2 for the charmed baryon. This scaling variable can be written in terms of lab variables as

$$x_F = 2\frac{(E_\pi + m_p)\, p_{\parallel D_1} - p_\pi E_{D_1}}{\sqrt{\Delta(s, M_D^2, 2.285^2)}} ,$$

where $\Delta(x,y,z)=x^2 + y^2 + z^2 - 2(xy + yz + zx)$. At our energies with s=408.1 GeV^2, the approximation

$$x_F \simeq E^{lab}_{D_1} / E^{lab}_{\pi}$$

is very good. Figure 36 shows the x_F distribution for the background subtracted D signal. Figure 37 shows the x_F acceptance of the apparatus as calculated with a flat x_F distribution in a

Fig. 36. Feynman x distribution for the background subtracted charged D data.

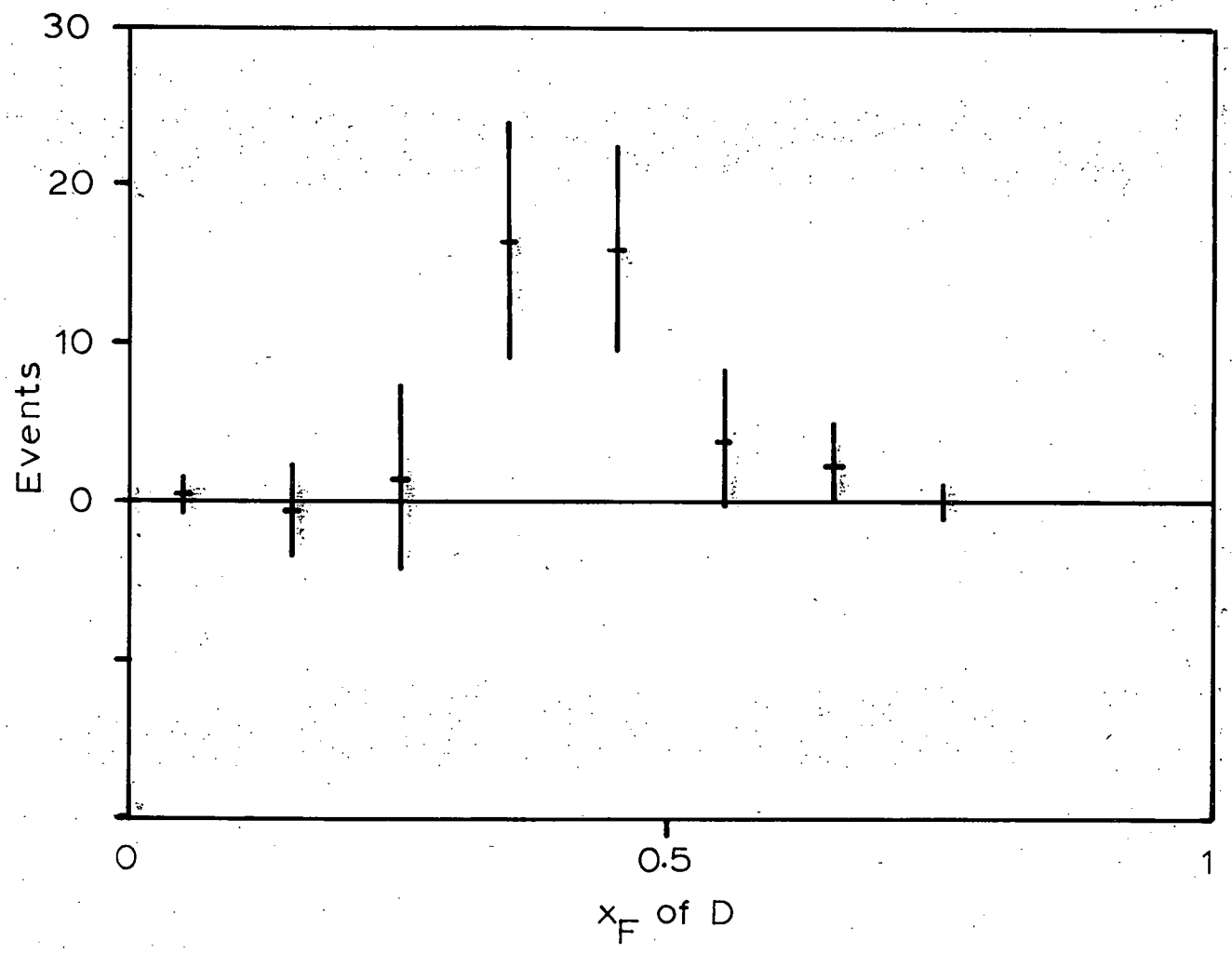
30
20
10
0
Events
0
0.5
1
x_F of D

Fig. 37. Feynman x distribution of Monte Carlo events showing the acceptance of D's generated with a flat Feynman x.

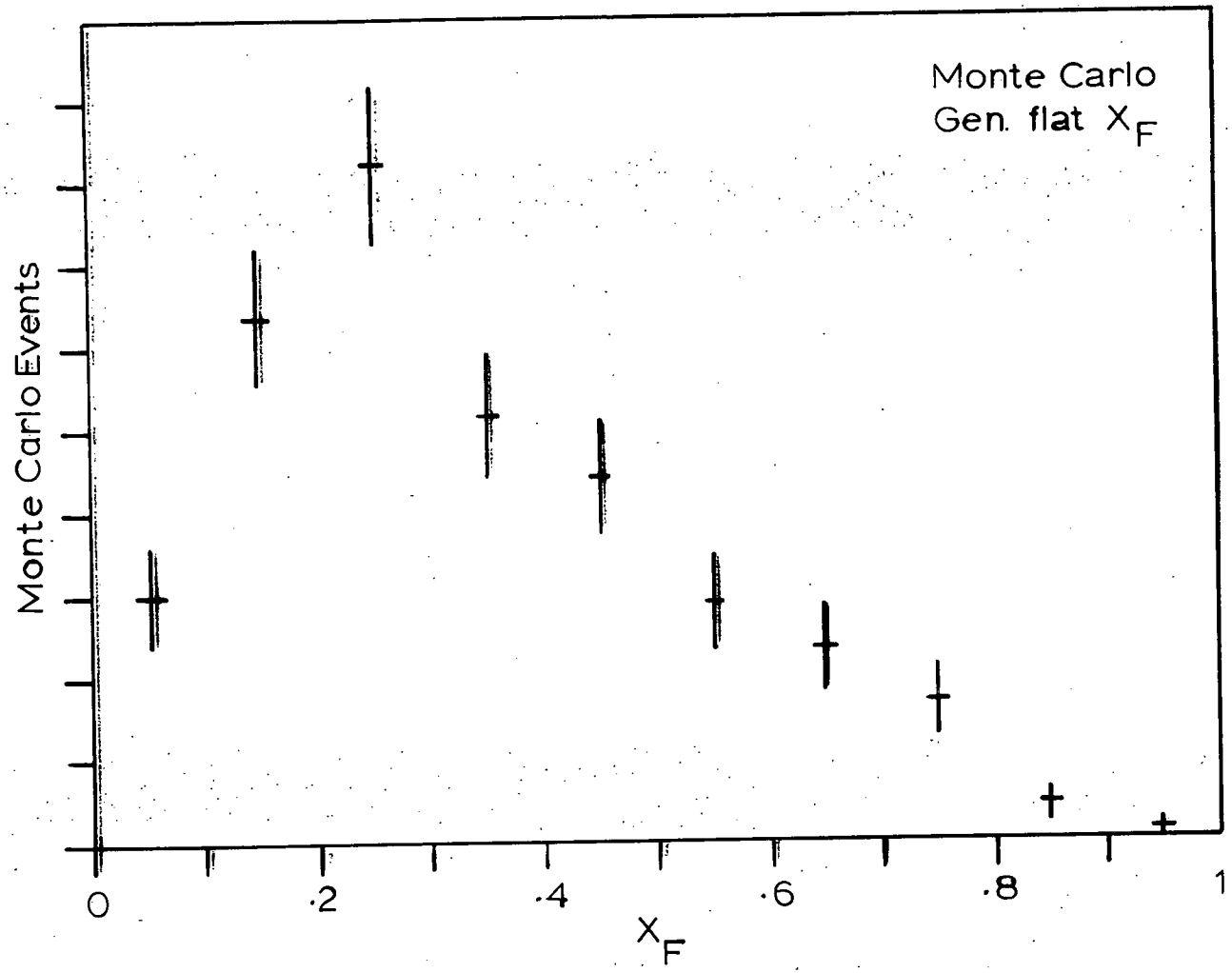
Monte Carlo
Gen. flat X_F
Monte Carlo Events
0
.2
.4
.6
.8
1
X_F

Monte Carlo. This Monte Carlo assumed no correlation between the two D's. Note that the data peaks around x_F=0.4 which is considerably higher than the acceptance peak around 0.25.

If a pair of D mesons is produced diffractively, we should expect the pair to carry off most of the beam's momentum. One of the D mesons should have about half the momentum of the pair, or an x_F just under 0.5.

The angular distribution in the lab is shown in Figure 38 for the D signal. The small angle peak also agrees with a diffractive interpretation. Figures 39 to 44 show the distributions for M_R, t_p, t_{D_1}, M_L, the charged track multiplicity, and the square of the perpendicular momentum component, $P_\perp^2$, of the D. The recoil mass, M_R, is quite sensitive to errors in the proton time of flight measurement and has an uncertainty of about 500 MeV/c^2. The M_R distribution is consistant with masses greater than or equal to the threshold for $D^+D^-\pi^-$ production. The t_p distribution fits to a form of $e^{-b|t_p|}$ with $b=16^{+11}_{-6}$ and is consistant with elastic π^--p data (b=9 (Perl, 1974)) as would be expected in a diffractive model with pomeron exchange. The t_{D_1} distribution shows a small momentum transfer to the D and indicates a diffractive process. Figure 42 shows the distribution of masses M_L recoiling against the proton and the reconstructed D. The minimum value of M_L should be 1860 MeV/c^2, but the proton time of flight measurement has systematic and statistical errors each of order 0.5 ns.

Fig. 38. Distribution of Lab angle for the background subtracted charged D data.

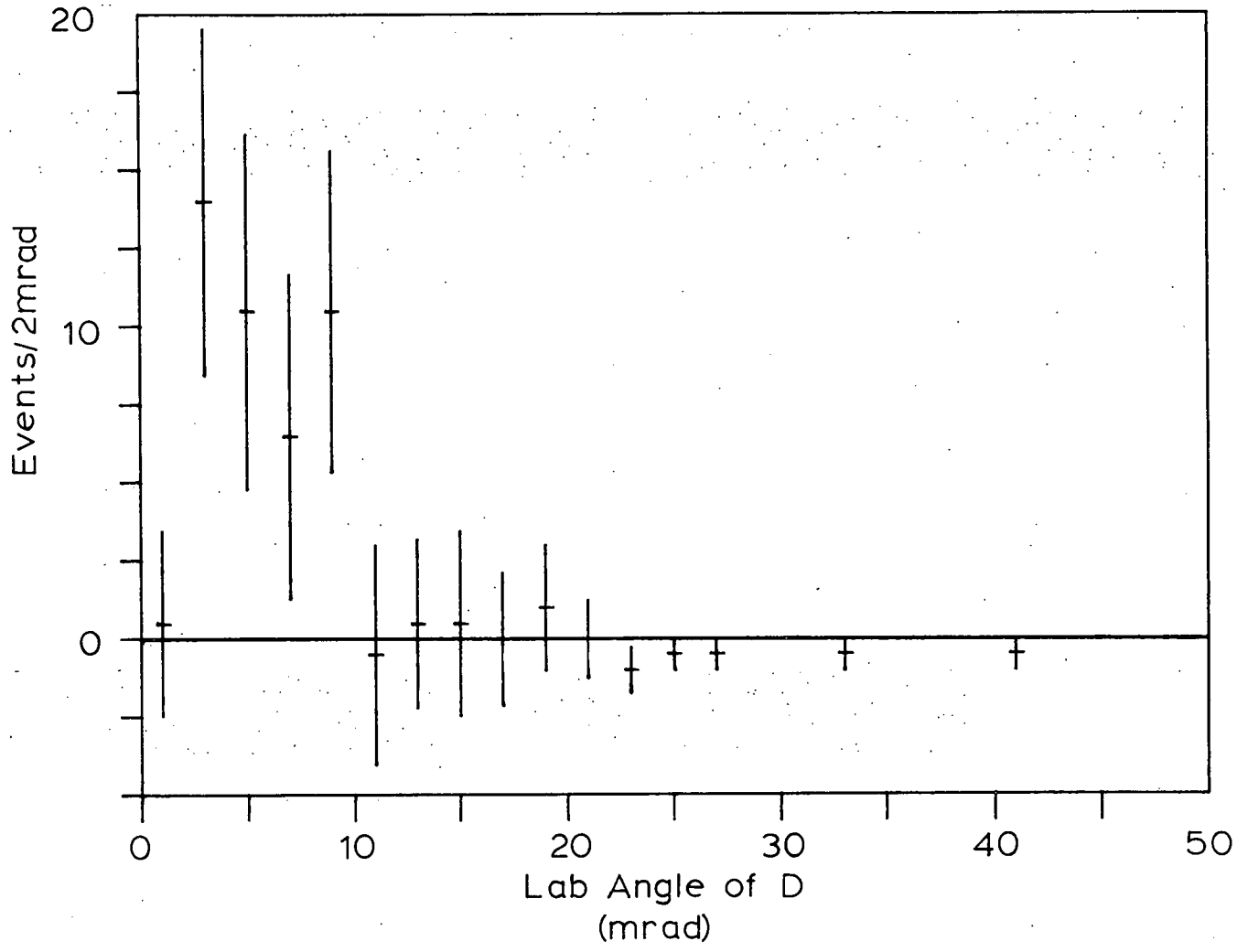
20
10
0
Events/2mrad
0
10
20
30
40
50
Lab Angle of D
(mrad)

Fig. 39. Mass M_R recoiling against the proton for the background subtracted charged D data.

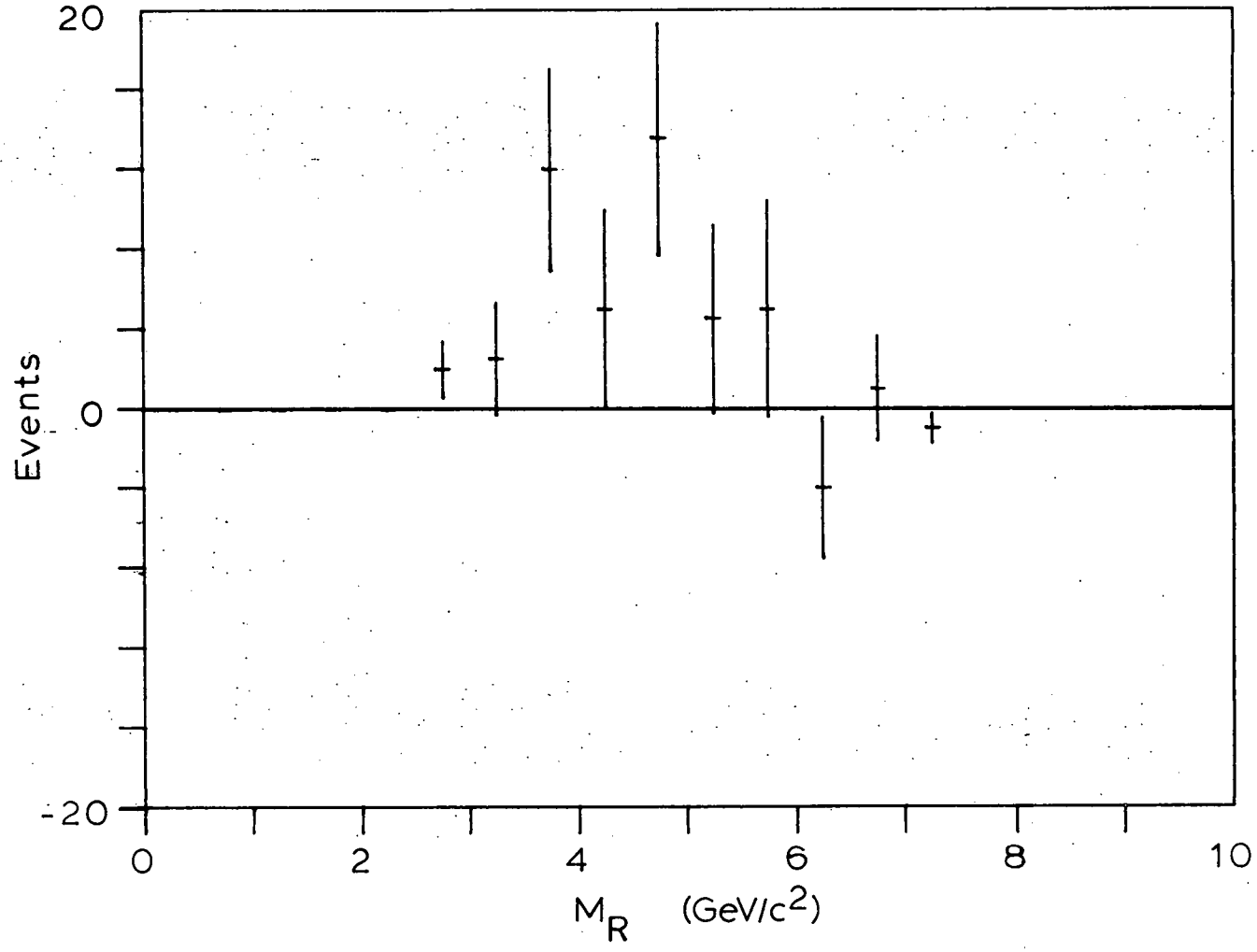
20
0
-20
Events
0
2
4
6
8
10
M_R (GeV/c^2)

Fig. 40. Distribution of the invariant momentum transfer to the proton, t_p, for the background subtracted charged D data. A fit to the form, $Ae^{-b|t_p|}$, is shown with $b=16^{+11}_{-6}$ $(GeV)^{-2}$.

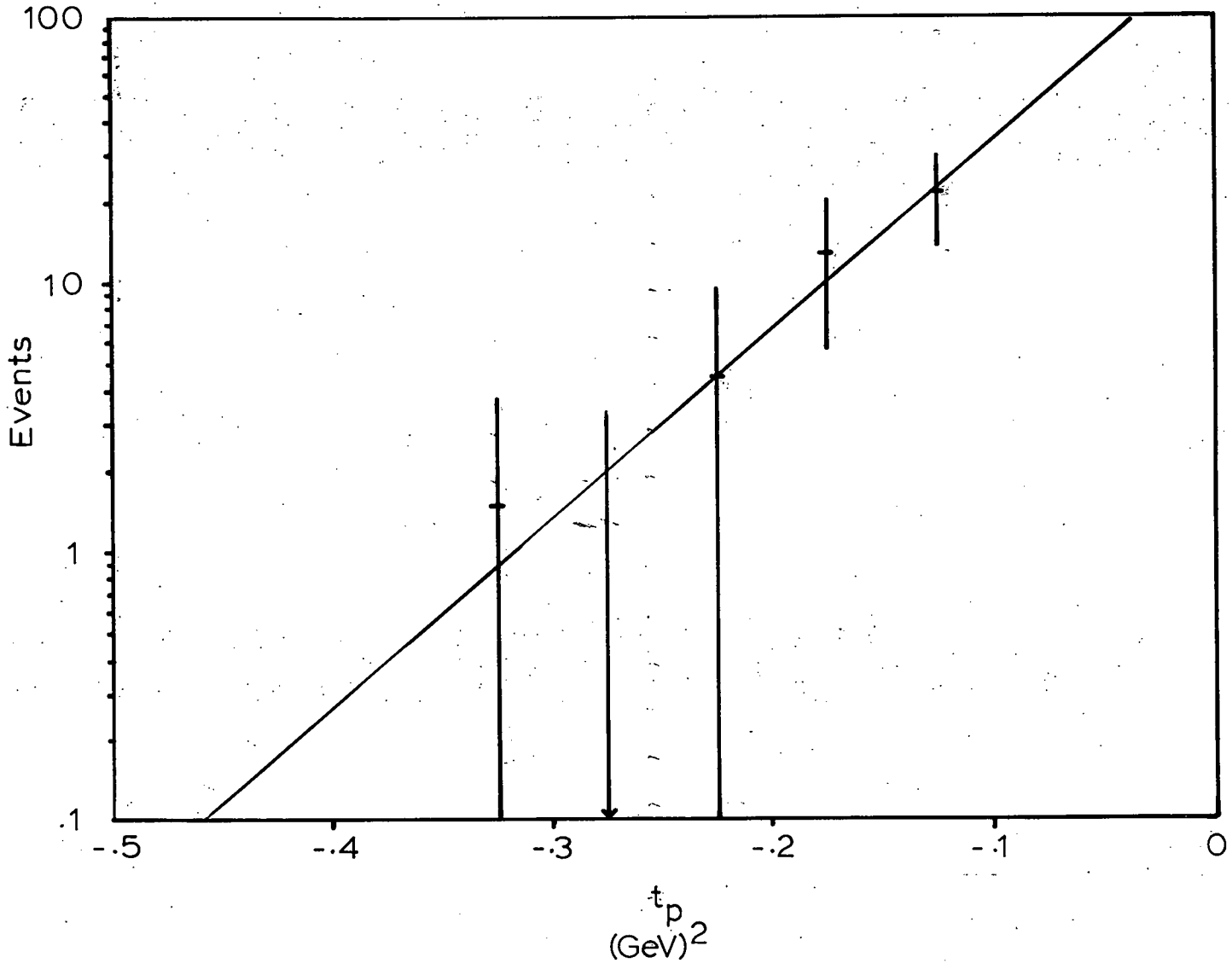
100
10
1
.1
Events
-.5
-.4
-.3
-.2
-.1
0
t_p
$(GeV)^2$

Fig. 41. Distribution of the momentum transfer squared to the D, $t_{0,}$ for the background subtracted charged D data.

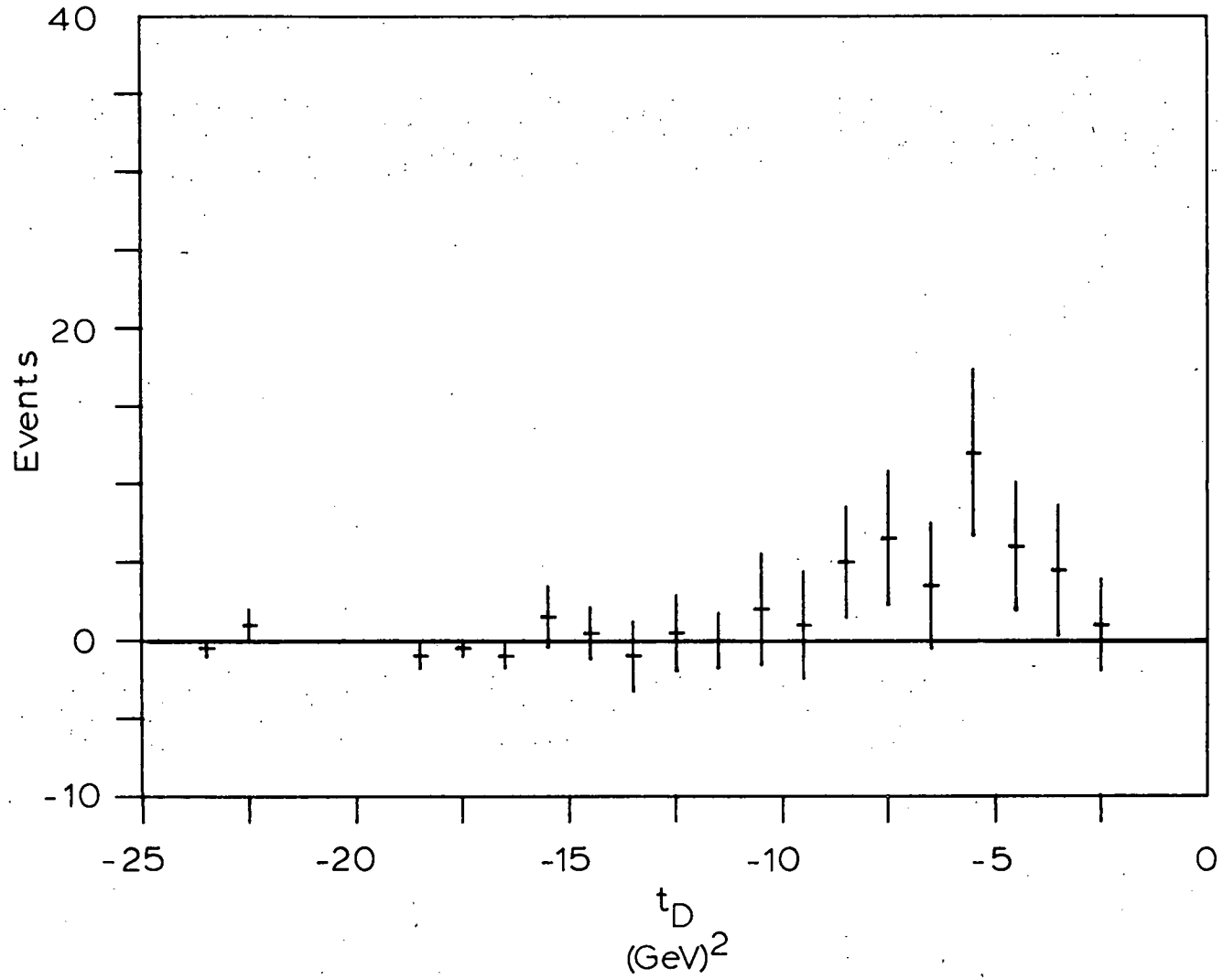
40
20
0
-10
Events
-25
-20
-15
-10
-5
0
t_D
$(GeV)^2$

Fig. 42. Mass M_L recoiling against the D and the proton for the background subtracted charged D data.

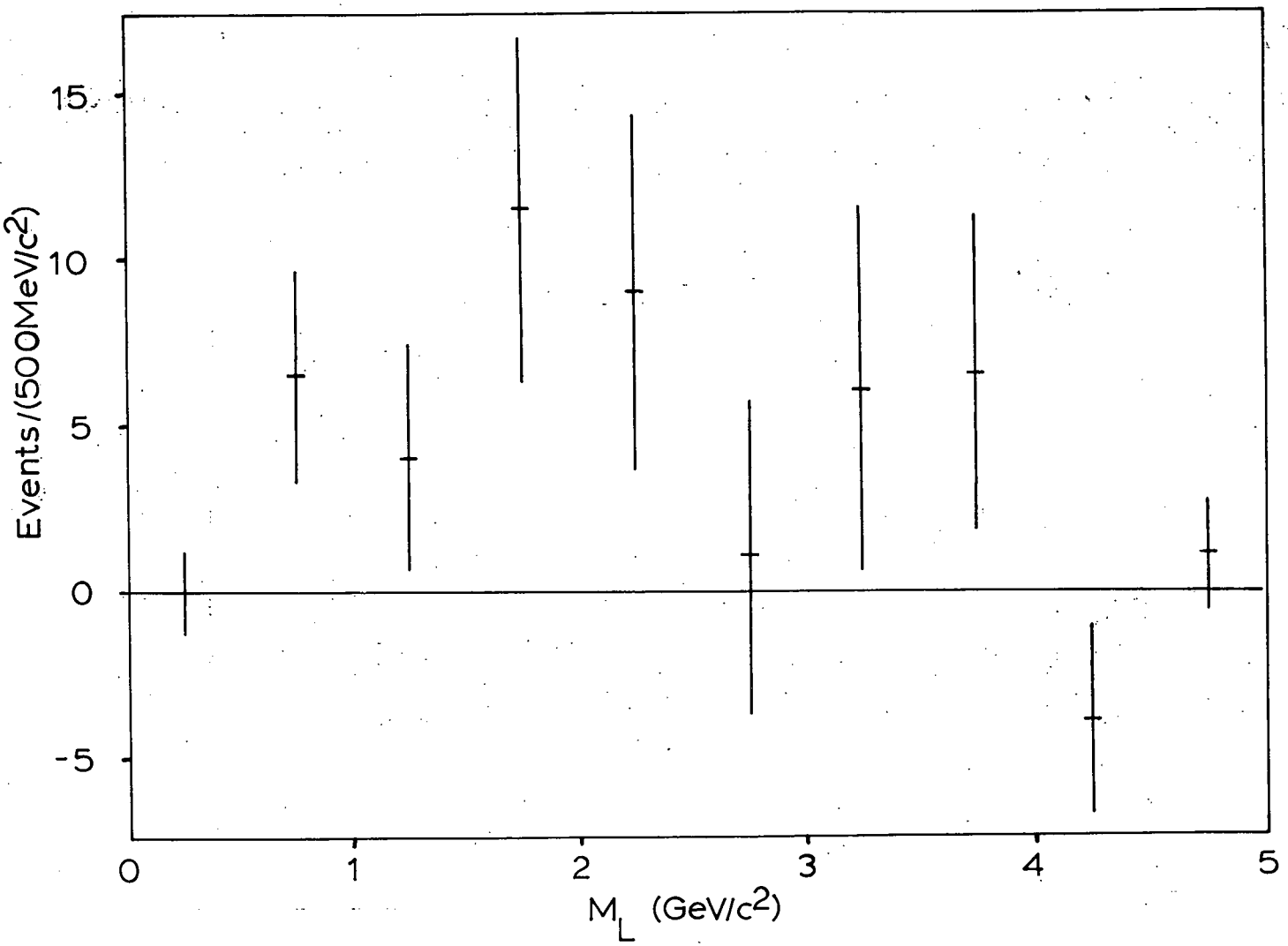
15
10
5
0
-5
Events/(500MeV/c2)
0
1
2
3
4
5
ML (GeV/c2)

Fig. 43. Charged multiplicity distribution for the background subtracted charged D data.

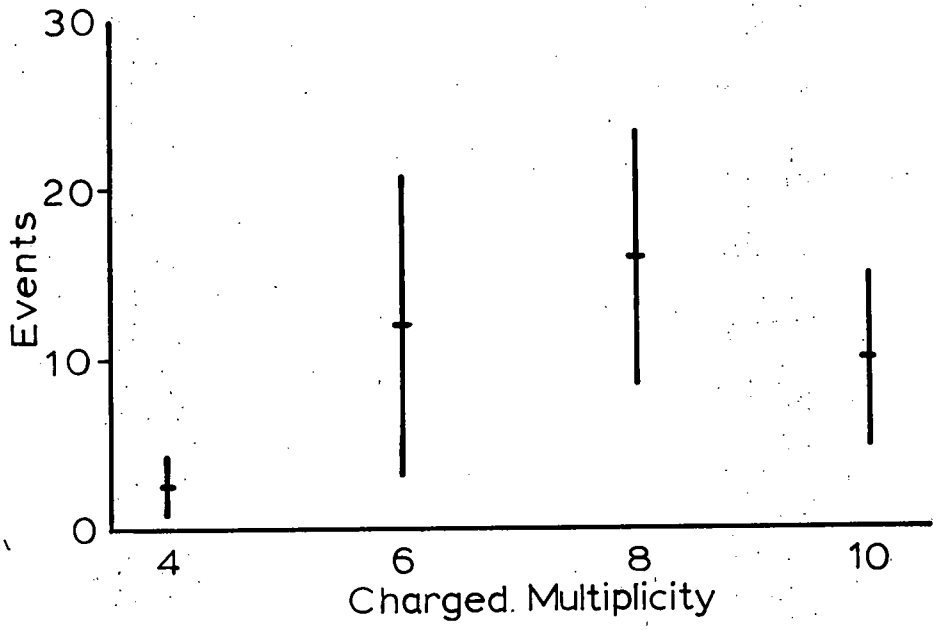
30
20
10
0
Events
4
6
8
10
Charged. Multiplicity

Fig. 44. $P_\perp^2$ distribution for the background subtracted charged D data. A fit to the form, $Ae^{bP_\perp^2}$, is shown with $b=-1.7^{+1.2}_{-1.4}$ $(GeV)^{-2}$.

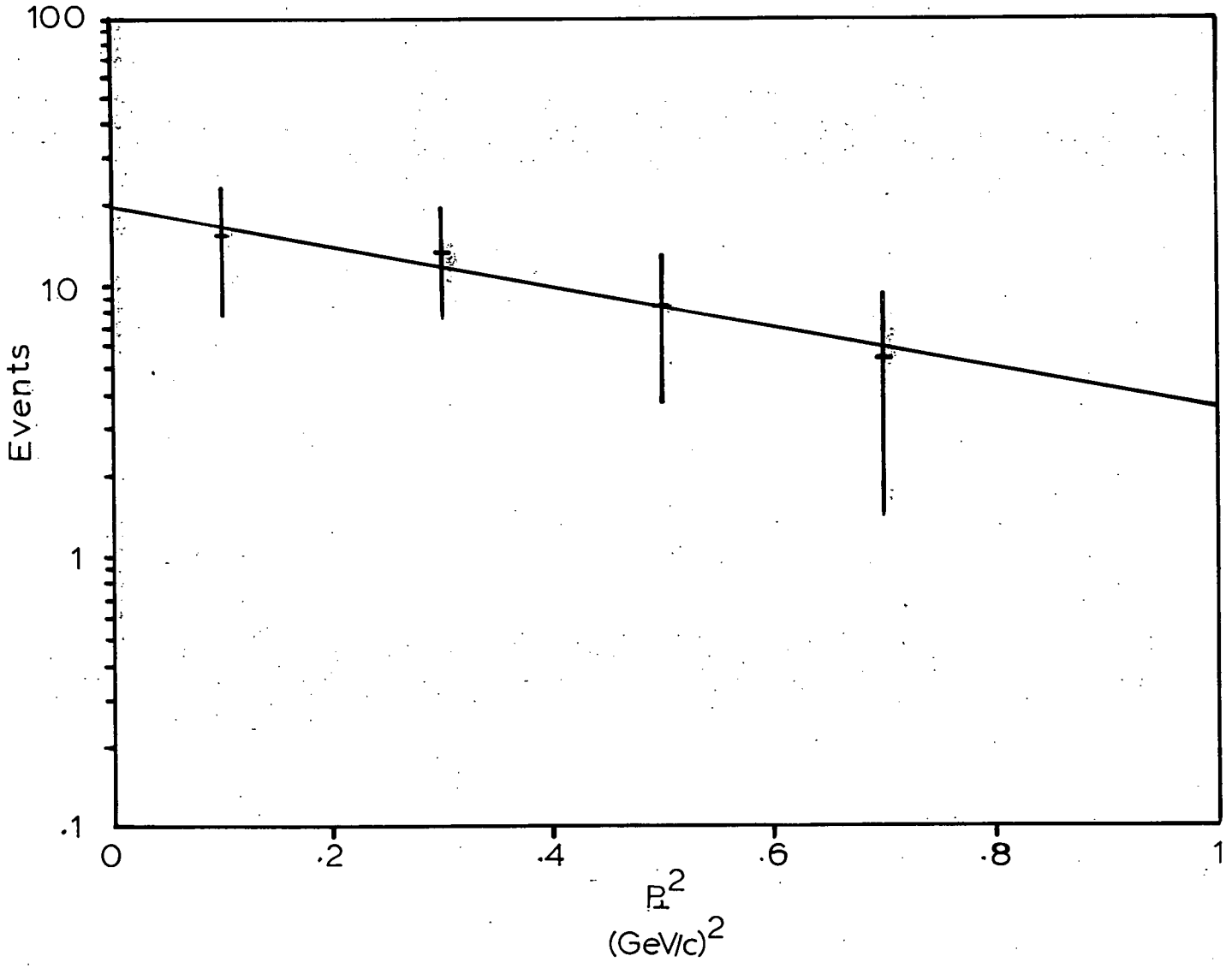
100
10
1
.1
Events
0
.2
.4
.6
.8
1
p_T^2
$(GeV/c)^2$

6.4 Diffractive Model

One of the models I have studied is a diffractive model for the reaction

$$\pi^- + p \longrightarrow p + D^+ + D^- + \pi^- \quad (D^- \longrightarrow K^+ + \pi^- + \pi^-;\ D^- \longrightarrow \mu^+ + K + \nu_\mu)$$

and also the reaction with the D meson decays reversed. Figure 45 shows a schematic of this reaction. The D mesons were assumed to decay isotropically with phase space.

The recoil proton was generated by using the formula for the proton differential cross section as given in the E369 proposal (Ascoli et al., 1975):

$$\frac{d^2\sigma}{dt_p\, dM_R^2} \propto e^{-b(M_R^2)|t_p|},$$

where $b(M_R^2)$ is given by

$$b = (4.6 + 7.0\ e^{-34.7 M_R^2/s})\ \text{GeV}^{-2}.$$

Using the generated proton, I calculated the four momentum of the $D^+D^-\pi^-$ system recoiling against the proton. Next, the $D^+D^-\pi^-$ system was allowed to decay according to 3-body phase space. Finally, I let the D mesons decay and propagated the tracks through the apparatus. Figures 46 and 47 show the x_F and angular distributions calculated for M_R of 4.0 and 4.4 GeV/c^2 in this model. The agreement with the data in both cases is very good.

Of the generated events, 15-20% satisfied the recoil proton trigger requirement. About 50% of these events passed the muon trigger requirement to give a combined trigger rate of 7-10%. More than 94% of the charged tracks recoiling against the proton were detected by the downstream spark chambers. The Cerenkov

Fig. 45. Schematic for the diffractive model described in section 6.4.

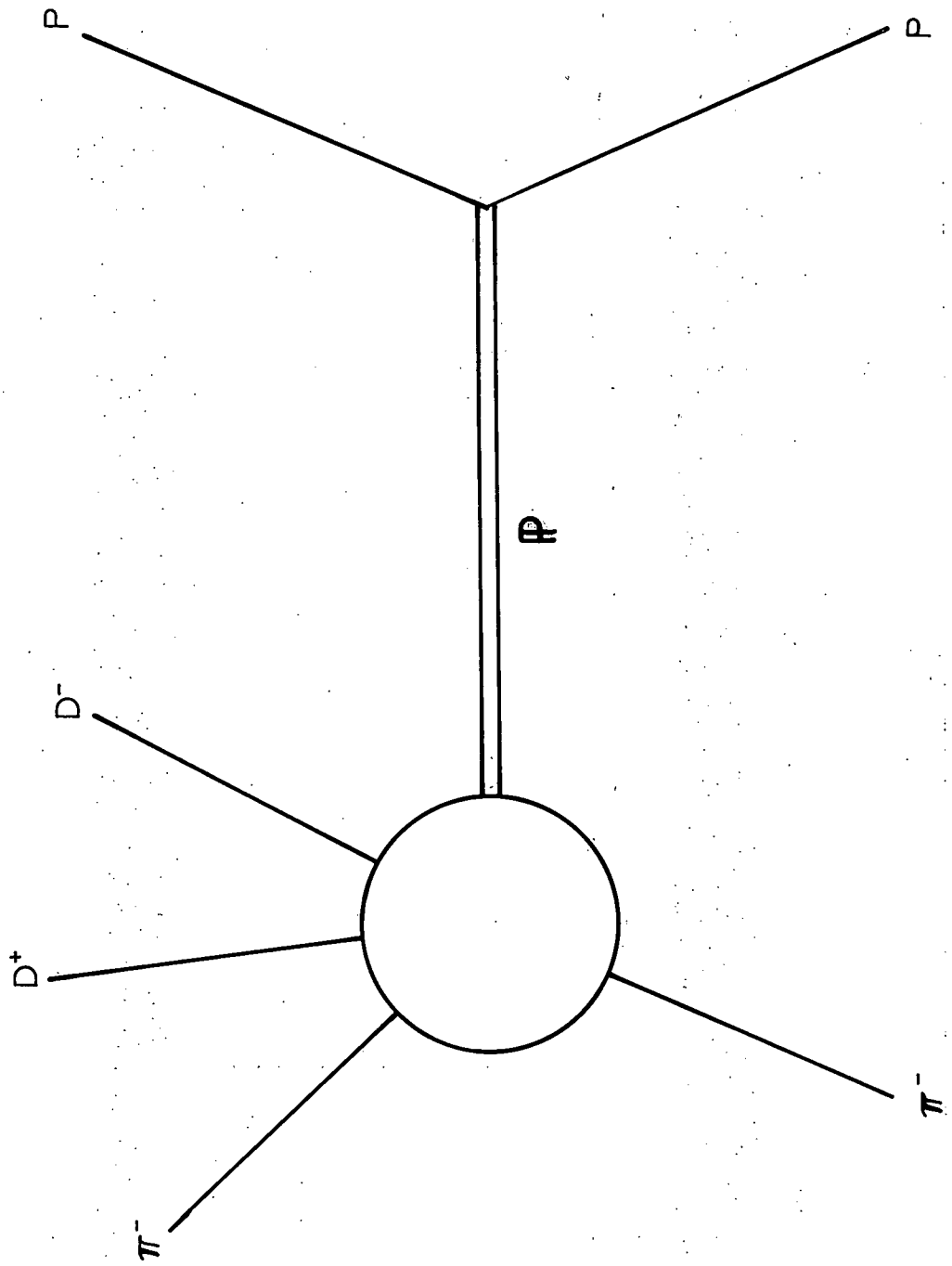
p
p
IP
D⁻
D⁺
π⁻
π⁻

Fig. 46. Monte Carlo x_F distribution for the hadronically decaying D's of the diffractive model of section 6.4.

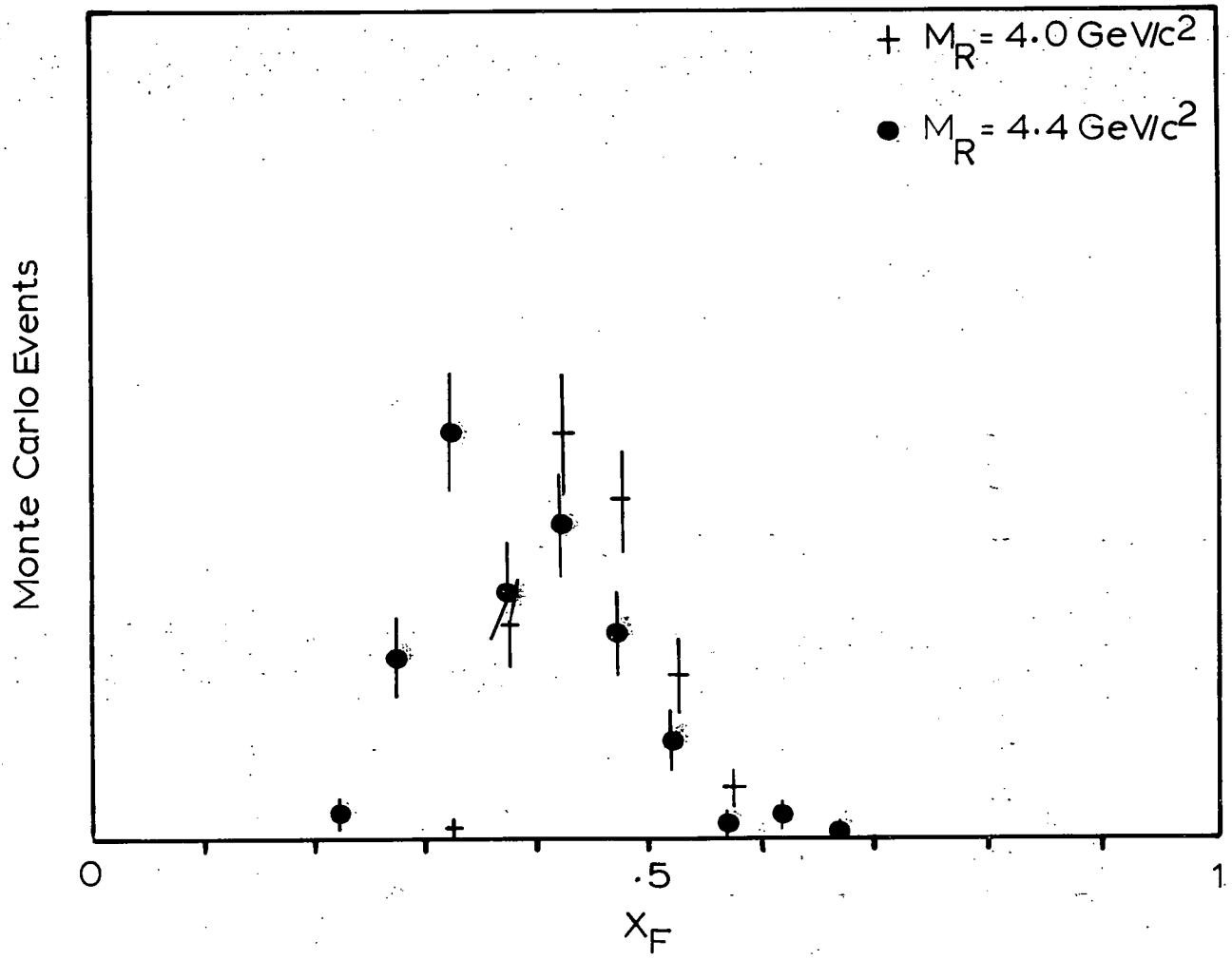
+ M_R = 4.0 GeV/c^2
● M_R = 4.4 GeV/c^2
Monte Carlo Events
0
.5
1
X_F

Fig. 47. The lab angle distribution for hadronically decaying D's from the diffractive model Monte Carlo of section 6.4.

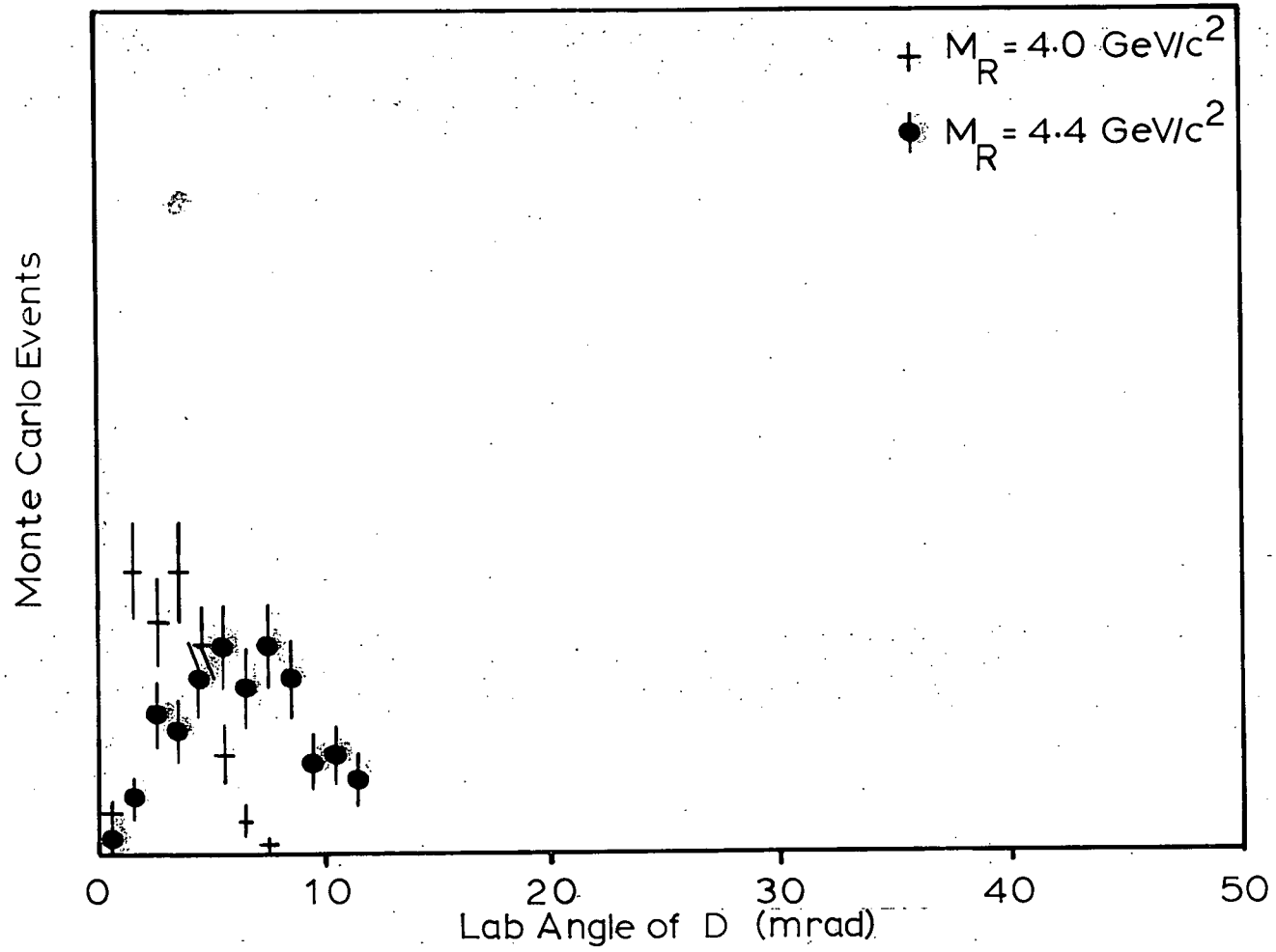
+ M_R = 4.0 GeV/c^2
● M_R = 4.4 GeV/c^2
Monte Carlo Events
0
10
20
30
40
50
Lab Angle of D (mrad)

identification of charged kaons also limited the acceptance. The momentum band for K identification was about 8-24 GeV/c. The final acceptance for reconstructed D's was about 1.2-1.8% depending on M_R. This acceptance is shown in Figure 48 as a function of M_R.

The same Monte Carlo, with a constant b=9 instead of the values 5-6.4 used above, gave identical x_F and angular distributions. The acceptance had the same M_R dependence but was decreased everywhere by about 0.2%.

6.5 Gluon Fusion Model

The gluon fusion model is a typical central production model. Jones and Wyld have calculated charm production for $s=450$ GeV^2 and a geometry similar to ours but without the same trigger requirement of a recoil proton and a prompt muon. Their model gives a total cross section for $c\bar{c}$ production of about 0.2-0.9 μb, and an x_F distribution much lower than my data. They also predict a much wider angular distribution.

Does the requirement of a recoil proton trigger change this model so that the distributions are more forward? To answer this question, I have modified their model to include a slow proton in the final state. Figure 49 shows a schematic of this modified gluon fusion model. The basic idea is that the gluon from the proton just carries off the momentum transfer from the proton as the pomeron does in the above diffractive model. The gluon from the pion has a distribution just as in the Jones-Wyld model:

$$g(x_g) = \frac{n+1}{16 x_g}(1-x_g)^n,$$

where I have used n=3 to give a somewhat flatter distribution than

Fig. 48. Acceptance for the reconstruction of charged D's as calculated by the diffractive model Monte Carlo of section 6.4.

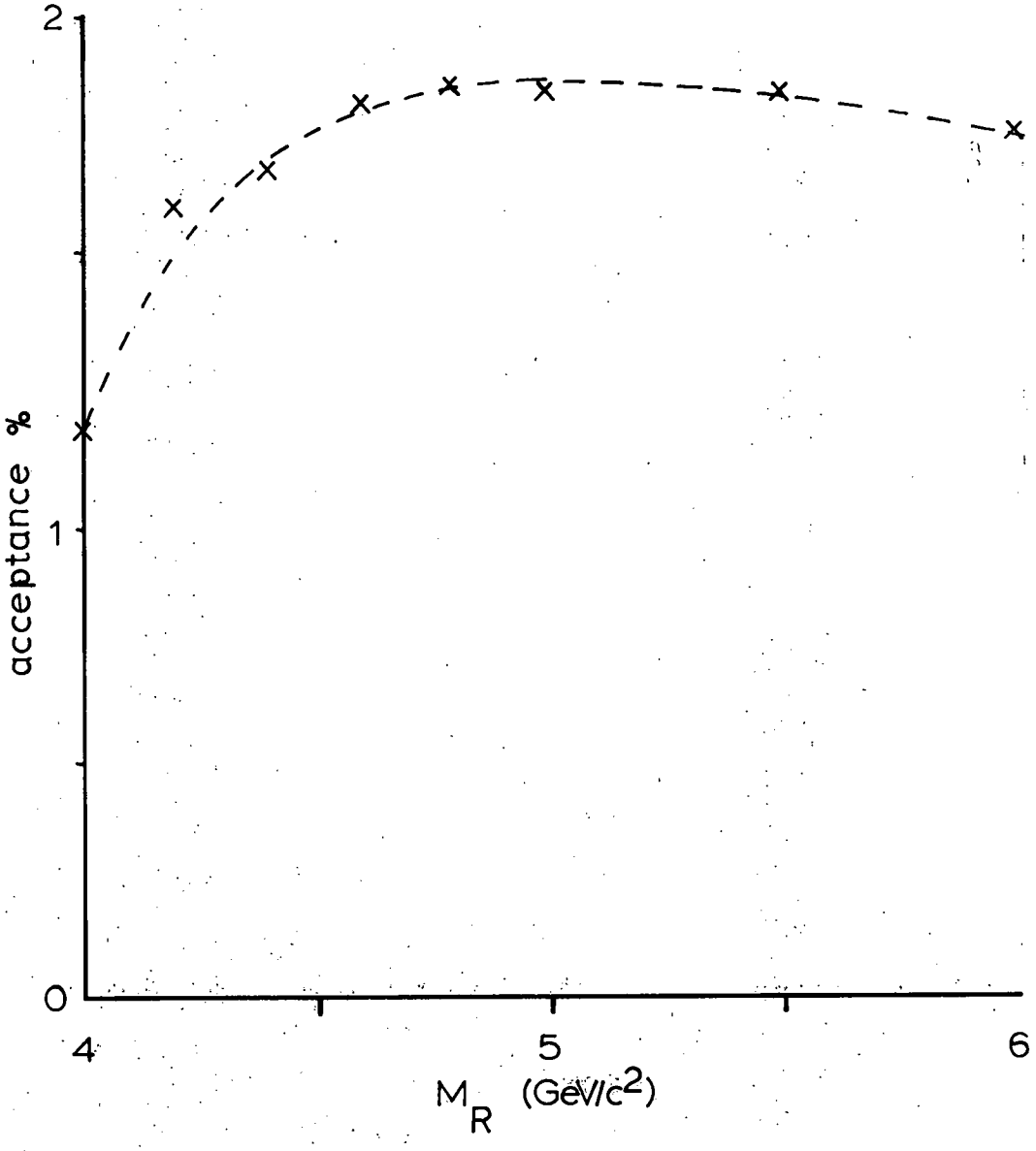
2
1
0
acceptance %
4
5
6
M_R (GeV/c^2)

Fig. 49. Schematic for the modified gluon fusion model described in section 6.5.

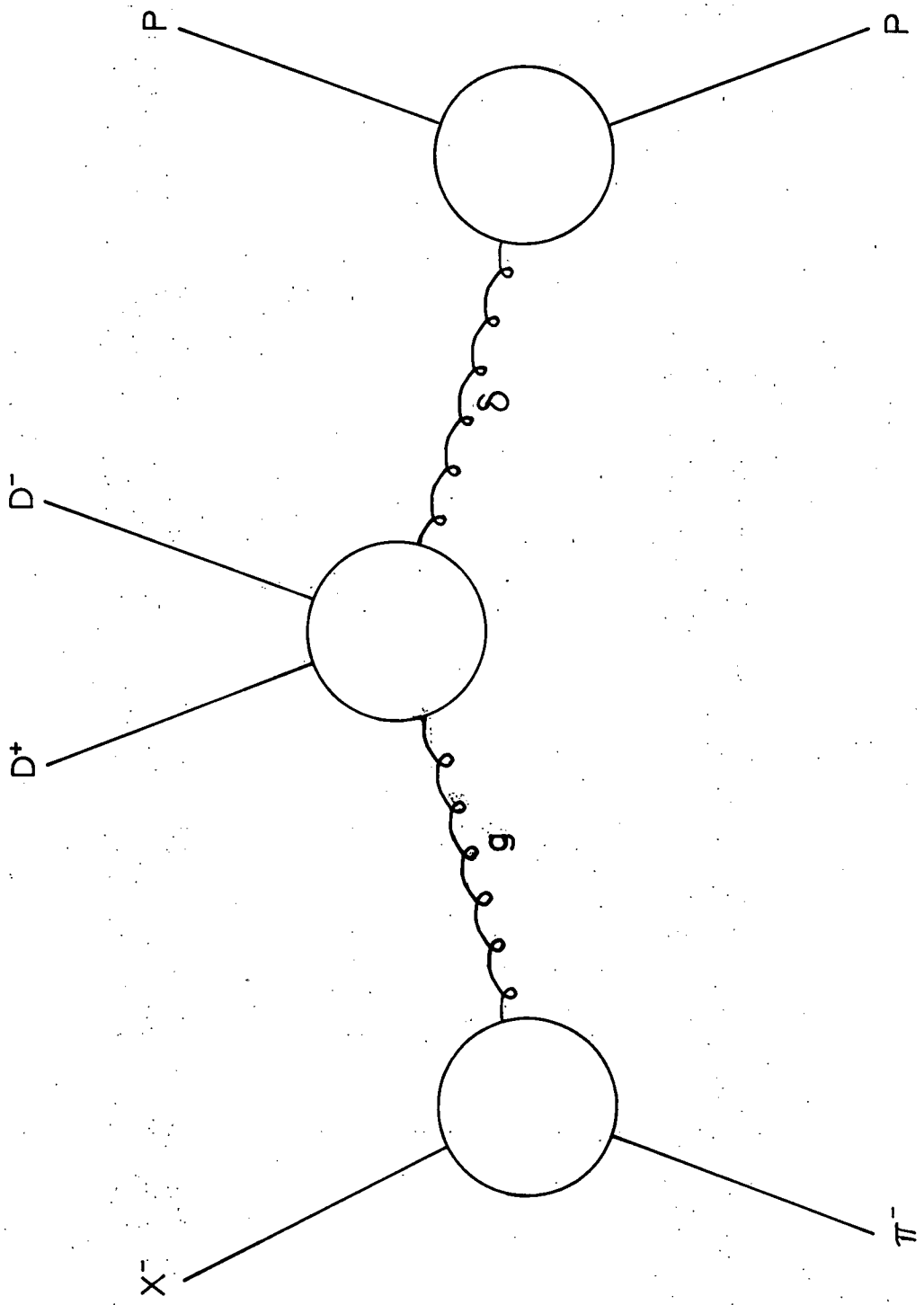
p
p
g
D⁻
D⁺
g
X⁻
π⁻

Jones and Wyld. The longitudinal momentum fraction of the beam momentum carried by the gluon g is x_g, and the fraction of the target momentum carried by gluon δ is x_δ. Momentum conservation in the high energy limit gives us

$$M_B^2 = x_g x_\delta s$$

for the mass of the central D^+D^- system. The integral for the total cross section is

$$\sigma = \int g(x_g)\ h(x_\delta)\ \sigma(M_B^2)\ \delta(x_g x_\delta s - M_B^2)\ dx_g\ dx_\delta\ dM_B^2,$$

where $h(x_\delta)$ is the proton gluon distribution function, and $\sigma(M_B^2)$ is the strength of the gluon-gluon interaction as given in section 2.2.1. For high energy and small t_p, the δ-gluon fraction becomes

$$x_\delta \simeq M_R^2/s,$$

and the g-gluon fraction becomes

$$x_g \simeq M_B^2/M_R^2.$$

The delta function in the above integral allows us to integrate over x_g before proceeding to the Monte Carlo:

$$\sigma \propto \int_{M_t^2}^{M_c^2} \int_{M_B^2/s}^{1} \frac{\sigma(M_B^2)}{M_B^2} \left(1-\frac{M_B^2}{M_R^2}\right)^3\ h(M_R^2/s)\ dM_R^2\ dM_B^2.$$

The limit M_t is just twice the D mass, and M_c is a cut off for which I used a value of 7 GeV/c^2.

Figures 50 and 51 show the x_F and lab angle distributions for the hadronically decaying D meson in this Monte Carlo with the acceptance folded in. The distributions do not agree with the data. They are essentially the same as for the unmodified Jones-Wyld model. This is because the gluon distribution function g(x) peaks at x=0 and falls off rapidly. The small momentum transfer requirement also forces the momentum fraction x_δ to be near zero. The x_F for the blob is just $x_g - x_\delta$ which is still near

Fig. 50. Monte Carlo x_F distribution for the hadronically decaying D's of the modified gluon fusion model. Our acceptance is folded into this plot. This figure should be compared with Figure 34.

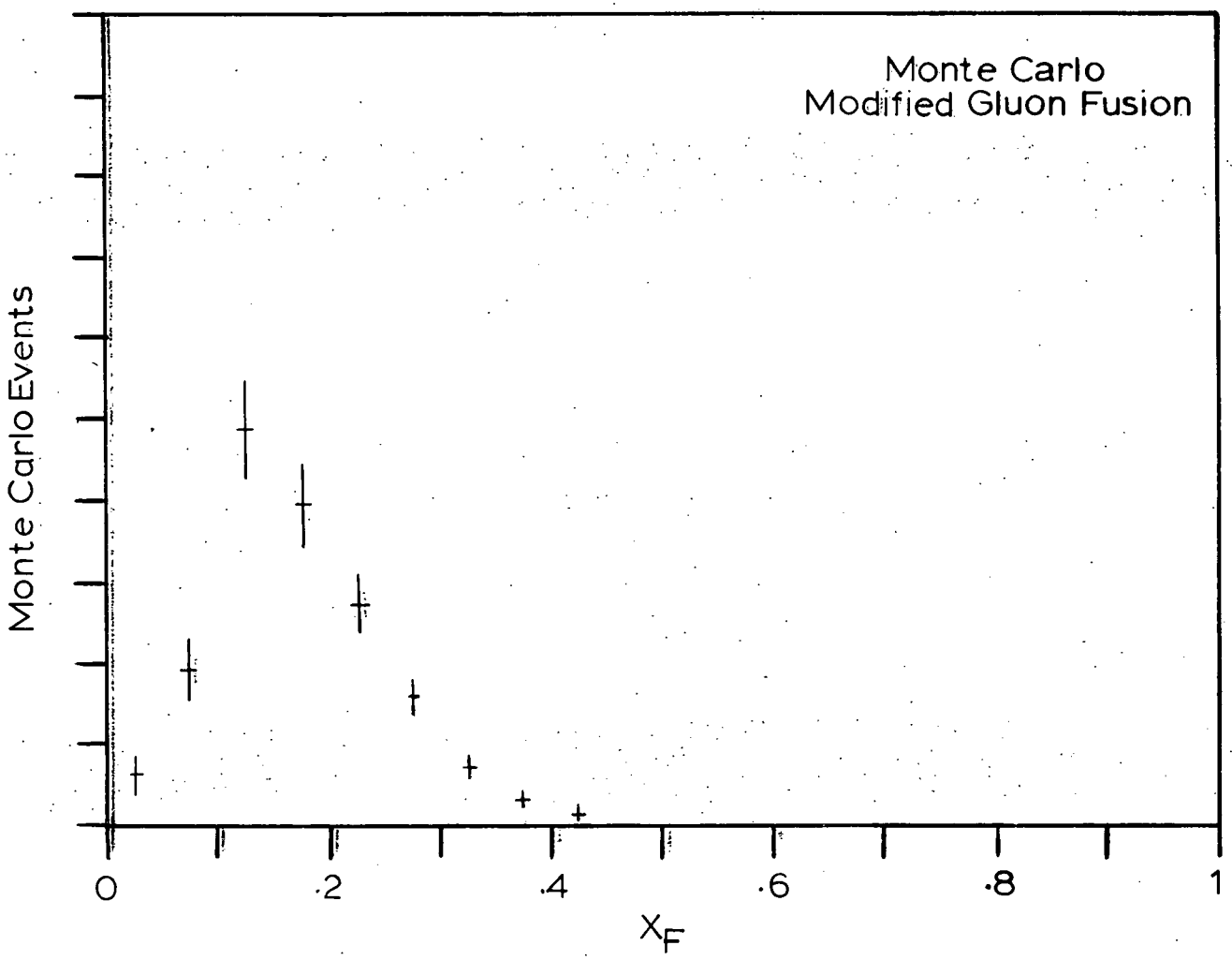
Monte Carlo
Modified Gluon Fusion
Monte Carlo Events
0
.2
.4
.6
.8
1
X_F

Fig. 51. The lab angle distribution for hadronically decaying D's from the Monte Carlo of the modified gluon fusion model of section 6.5.

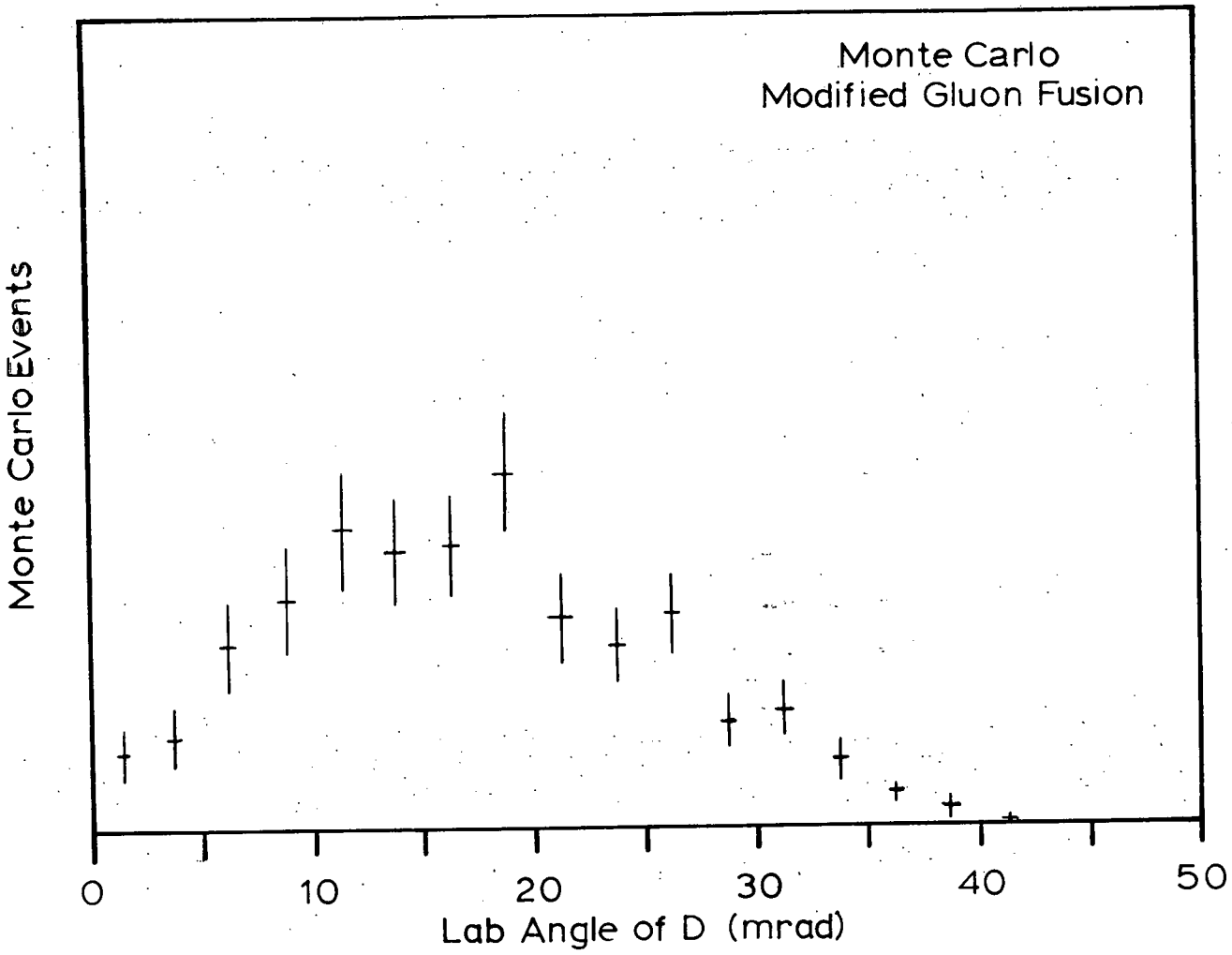
Monte Carlo
Modified Gluon Fusion
Monte Carlo Events
0
10
20
30
40
50
Lab Angle of D (mrad)

zero. This model gives an acceptance at least a factor of 10 smaller than the diffractive model.

6.6 Cross Section

To calculate a cross section I use the formula,

$$AB\sigma TF = n,$$

where $n=50\pm12$ is the number of D events, $F=1.1\times10^{10}$ is the flux of beam particles, and $T=1.7/\text{barn}$ is the length of the target times density times Avogadro's number. For , I have used the acceptance calculated for the diffractive model in section 6.4, and B is the over all branching ratio,

$$B = B(D^+ \rightarrow K^-\pi^+\pi^+)B(D^- \rightarrow \mu^- X) + B(D^+ \rightarrow \mu^+ X)B(D^- \rightarrow K^+\pi^-\pi^-)$$

$$= (2)(4.5\pm0.8\%)(23\pm6\%) \quad \text{(Kirkby, 1979)}$$

$$= 2.1\pm0.7\%.$$

This gives $A\sigma=130\pm50$ nb. For the diffractive model the acceptance is between 1.2% and 1.8% depending on the value of M_R (see Figure 48). This yields a total diffractive cross section for pD^+D^- production of $(7\text{-}10)\pm4$ μb.

Contamination in the muon trigger by nonprompt muons would lower this cross section estimate. There are two sources for this contamination: 1) in-flight decay of pions and kaons before reaching the muon detector, and 2) hadrons punching through the steel absorber and firing the muon hodoscopes. I looked at data from the LMP trigger which had no muon trigger requirement to get an estimate of this contamination. Of a sample of 2105 downstream tracks, only 14 were identified as muons by the M' and P hodoscopes. This gives a bogus muon rate of about 0.007 muon per track. We should expect about 10^{-4} prompt muons per track from

charm production (Ritchie, 1980). If we assume an average charged track multiplicity of 7 downstream tracks per D event, we may expect to observe a non-prompt muon in 4.9% of the events. This is consistent with the nonprompt muon partial acceptance (5%) estimated at the end of chapter 4. This 4.9% should be added to the 23% branching ratio $B(D^+ \longrightarrow \mu^+ X)$ to yield an overall branching ratio B=2.5%. Our previous cross section estimate is lowered to 6 to 9 μb.

6.7 Comparison with Other Data

Recent experiments (Brown et al., 1979; Diamant-Berger et al., 1979; Ritchie et al., 1980) look at prompt muons from p-Fe interactions at 350 GeV and 400 GeV. Their apparatus was a large calorimeter target and muon identifier. They used central production models and assumed that all of the muon excess over background came from semileptonic decays of D mesons. They arrived at a total cross section for DD production around 10-40 μb/nucleon which is highly model dependent. My cross section of 6-10 μb is smaller, but this should be expected since it is only for the diffractive region including a recoil proton.

Three other experiments were performed at the CERN ISR with colliding proton beams and $\sqrt{s}$ of about 52 and 62 GeV. One shows evidence for D^+ production in the $\overline{K^{*0}}\pi^+$ channel (Drijard et al.,1979a) and Λ_c^+ production (Drijard et al.,1979b) in the $\overline{K^{*0}}$p and $K^-\Delta^{++}$ channels. The other two (Lockman et al., 1979; Giboni et al., 1979) see Λ_c^+ production in the $K^-\pi^+$p and $\Lambda^0\pi^+\pi^+\pi^-$ channels. All three experiments indicate substantial forward production.

The Giboni group required a proton in the final state and used a diffractive model to calculate their acceptance. They obtained a branching ratio times cross section of

$$\sigma B(\Lambda_c^+ \longrightarrow K^- p \pi^+) = 0.7\text{-}1.8\ \mu b.$$

If one uses the Mark II estimate for this branching ratio of 1.5% (Hitlin, 1979), the above result implies a total cross section of 50-120 μb for Λ_c^+ production. Since diffractive cross sections have essentially no s dependence (Albrow et al.,1976) and the Λ_c^+ mass is not very different from the D mass, my cross section should remain the same when scaled to their energy. The large difference may arise form the use of a pion beam rather than proton beams. A mechanism such as Gustafson and Peterson propose (Gustafson et al., 1977; Peterson, 1980), which assumes that a proton has a nonnegligible $uudc\bar{c}$ contribution to its wave function, might give a larger cross section for a proton than for a π^- beam (with a $d\bar{u}c\bar{c}$ contribution). I say this since the pion has a much smaller mass than the proton and therefore the contribution from heavy quarks is probably smaller.

CHAPTER 7

Conclusion

I see production of charged D mesons in π^--p interactions with a recoil proton and prompt muon trigger. The x_F and angular distributions indicate that the production is diffractive. A total of 50±12 charged D events are seen in the $K^{\pm}\pi^{\mp}\pi^{\mp}$ channels and are split between the two channels in about equal amounts. An upper limit of 4 is placed on the number of neutral D events in the $K^{\pm}\pi^{\mp}$ channels with a 90% confidence level. If we assume that the D^+D^- cross section is about the same as for D^oD^-, we should only expect to see about 6 D^o events.

The measured total diffractive cross section for pD^+D^- production is about 6-10 μb. This assumes that all my signal was from $D\bar{D}$ production and ignored any D^* production. This result does not exclude central production of charmed mesons, since we had a diffractive trigger, but it does indicate that diffractive processes are large enough to be competitive.

References

Albrow, M. G. et al., Nucl. Phys. B108, 1, (1976).

Alverson, G. O., thesis, University of Illinois, 1979.

Ascoli, G. et al., "Search for Charmed Particles Revised Proposal 369", (October ,1975).

Bander, M. et al., Phys. Rev. Lett. 44B, 7, (1980).

Brown, K. W. et al., Phys. Rev. Lett. 43, 410, (1979).

Carlson, S. E. and R. Suaya, Phys. Rev. D17, 760, (1978).

Denegri, D. et al., Preprint-Saclay, (1975).

Diamant-Berger, A. et al., Phys. Rev. Lett. 43, 1774, (1979).

Drijard, D. et al., Phys. Lett. 81B, 250, (1979a).

Drijard, D. et al., Phys. Lett. 85B, 452, (1979b).

Einhorn, M. B., lecture notes: Fermilab-Lecture-75/1-Thy/Exp, (1975).

Gaillard, M. K. and B. W. Lee, Rev. Mod. Phys. 47, 277, (1975).

Giboni, K. L. et al., Phys. Lett. 85B, 437, (1979).

Gustafson, G. and C. Peterson, Phys. Lett., 67B, 81, (1977).

Hicks, R. G., thesis, University of Illinois, 1978.

Hitlin, D., talk given at the 8th Hawaii Topical Conference in Particle Physics, 1979.

Jackson, J. D., Classical Electrodynamics, J. Wiley and Sons, New York, 1962.

Jones, L. M. and H. W. Wyld, Phys. Rev. D17, 1782, (1978).

Kerns, C. R., IEEE Trans. on Nucl. Sci. NS-24, 353, (1977).

Kirkby, J., Talk at the Fermilab Photon-Lepton Conference, 1979.

Lockman, W. et al., Phys. Lett. 85B, 443, (1979).

Measday, D. F. and C. R. Serre, "Loss of Protons by Nuclear Interactions in Various Materials", CERN 69-17

Perkins, D., Introduction to High Energy Physics, Addison-Wesley, 1972.

Perl, M. L., High Energy Hadron Physics, J. Wiley and Sons, New York, 1974.

Peterson, C., NORDITA preprint, NORDITA-80/2.

Pordes, S., thesis, Harvard University, 1976.

Ritchie, J. L. et al., Phys. Rev. Lett. 44, 230, (1980).

Rosen, S. P., Phys. Rev. Lett., 44B, 4, (1980).

Rossi, B. B., High Energy Particles, McGraw Hill, New York, 1952.

Roy, P., Theory of Lepton-Hadron Processes at High Energies, Oxford, 1975.

VITA

William Wallace MacKay was born in [redacted] He graduated from Williamson High School in West Virginia in 1970. He received a Bachelor of Science in physics from the University of Virginia in 1974. At the University of Illinois, the author held teaching and research assistantships and received a Master of Science in physics in 1976. He is also coauthor of "Production of Photons Associated with the ψ by 217-GeV/c π^- Mesons," T. B. W. Kirk et al., Phys. Rev. Lett. 42, 619(1979).